OPTICAL CHARACTERIZATION OF PROCESSED GALLIUM ARSENIDE

by

Ramon Alfredo Carvalho Siochi

Dissertation submitted to the Faculty of
the Virginia Polytechnic Institute and State University
in partial fulfillment of the requirements for the degree
of

DOCTOR OF PHILOSOPHY

in

PHYSICS

APPROVED:

Richard Zallen

Richard Zallen, Chairman

G. J. M. Indebetouw

J. G. Dillard

A. L. Ritter

C. D. Williams

December, 1990

Blacksburg, Virginia

Optical Characterization of Processed Gallium Arsenide

by Ramon Alfredo Carvalho Siochi

Committee Chairman: Richard Zallen
Department of Physics

(ABSTRACT)

Raman scattering and ultraviolet-visible reflectivity have been used to characterize the structural and electronic changes that occur in GaAs during ion implantation and subsequent annealing. In this work, the damaged structure is modelled as an amorphous GaAs matrix embedded with GaAs microcrystals. The longitudinal-optic (LO) Raman-line characteristics were monitored to determine the amorphous volume fraction, the average microcrystal diameter and, for the annealed samples, the carrier concentration. An oscillator analysis of the reflectivity spectra, along with the effective medium approximation, was carried out to determine the linewidths of the interband peaks and the amorphous volume fraction in the damage layer.

To determine damage depth profiles, spectra were taken as a function of the amount of material removed via chemical etch. A new method of interpreting reflectivity spectra was developed to deal with the etchant-induced roughness. This roughness reduced the reflectivity by a constant factor in the region between 4.5 and 5 eV. The ratio between reflectivities at 4.55 and 4.75 eV was monitored to determine qualitatively the amount of damage.

The annealing studies show that structural recovery occurs

at a lower temperature than that for which electrical activation occurs. The depth profile of a sample annealed at 400°C reveals that nucleation takes place not only at the boundary between the damaged and undamaged layers (i.e., "epitaxial regrowth") but also at the microcrystal/amorphous interfaces within the damage layer.

The oscillator analysis of the dielectric properties was further developed, and a connection was established between the strengths, positions, and linewidths of the interband oscillators and the shift in position of the LO Raman line. The results indicate that the static dielectric constant is independent of microcrystal size.

A comparison between (211) and (100) oriented Si-implanted GaAs was done as well, showing greater near surface damage and a shallower total damage layer for the (211) samples.

Finally, a method for characterizing damage, based on the observed shifts of the two-phonon ("2LO") Raman peak as the incident photon energy is varied around the E_1 interband energy (2.9 eV), has been developed. The results suggest that the total mass of the electron-hole pair involved in the scattering process increases even for large (>400 Å) microcrystals. The 525°C annealed sample had little damage, and was studied with this technique.

Acknowledgments

I am very grateful for the encouragement and support of my advisor, Prof. Richard Zallen. The wisdom and kindness he showed me in guiding my dissertation work is a blessing to me. I enjoyed working with him very much, and I greatly appreciate all the time he spent helping me.

I am also thankful for all the suggestions and helpful comments of all those who served on my dissertation committee, Prof. Guy Indebetouw, Prof. Jimmy Ritter, Prof. Larry Burton, Prof. Clayton Williams and Prof. John Dillard. Our conversations were very fruitful, and I am grateful for their thoughtfulness. I am particularly grateful to Prof. Diane Hoffman who always encouraged me in my work every time I talked with her.

I appreciate the kindness shown to me by Prof. Norman Eiss who taught me how to use his optical profilometer and made it available to me. I also thank Prof. Alan Schick and Marilyn O'Grady for letting me use their Raman equipment and for their invaluable assistance with the experimental set-ups.

I am also indebted to Dr. Guofu Feng and Dr. Mark Holtz. Their research served as a foundation for much of my own work. I am also thankful that they took the time to familiarize me with the different laboratory apparati, and that we had many useful conversations.

I thank Texas Instruments, ITT Corporation, and the Virginia Center for Innovative Technology for supporting my research.

I am grateful for all the support of the staff members of the Physics department. Dale Schutt, Grayson Wright and Roger Link from the electronics shop, and Dave Miller, Bob Ross, Melvin Shaver and John Miller from the machine shop were especially helpful in providing the accessories needed for my experiments. I am also grateful to Chris Thomas, Lou Terhune, Judy Faw and Sheri Turner for taking care of all the paperwork needed in the course of my studies.

I have enjoyed the collaborative efforts with Dr. June Epp, Dr. Ashok Vaseashta and in particular, Dr. Sidharta Sen, whose electrical measurements were of great value to my research. I am also thankful for all the conversations and help of Calvin Doss, especially in getting some of the pieces of equipment in the Raman set-up repaired.

I am very grateful for the support and advice of my parents, my brothers Antonio, Fernando and Octavio, my sister Lucia, my sister-in law Mia and to all my friends, especially my fiancée, Ann Webb, who have been praying for me and my work.

Finally, I thank my Lord Jesus Christ for blessing my work and giving me the strength and motivation to complete it. It is to Him I dedicate this work.

TABLE OF CONTENTS

CHAPTER ONE
INTRODUCTION

1.1 Processing and Optical Probes

Gallium arsenide (GaAs) is a semiconductor which can be used to make devices that are potentially superior to the silicon-based ones. However, since GaAs technology is quite young, the performance of GaAs-based devices is not yet on par with that of silicon. Hence, much research is focused on the effects of processing steps (e.g. doping, annealing, and etching) on device performance.

The most controlled and reproducible method of introducing dopants into semiconductors is through ion implantation [Pearton; Ryssel and Ruge]. This process involves focusing a beam of dopant ions (such as Be and Si) onto a wafer of GaAs. The depth distribution of the dopants depends on their mass and initial energy. As these ions move through the target, their energies change as a result of the numerous nuclear collisions with the target. Since damage results from the breaking of bonds between target atoms, damage occurs where the energy is sufficient; since the energy varies with depth, the structure of the target will also vary with depth. An understanding of the damage distribution should help improve doping methods.

To make the implanted sample useful for device applications, the structure of the implanted layer must be restored to approximately that of the virgin crystal. To accomplish this, the implanted

sample is annealed at high enough temperatures (>550 °C) to cause regrowth of the damaged material. However, at a temperature above 657°C, the stoichiometry of the crystal can change appreciably enough (due to As evaporation) to degrade device performance [Duncan and Westphal]. Compensation can occur, decreasing the number of carriers in the device. The kinetics of crystal regrowth and annealing methods then become important considerations when seeking improved device performance.

Besides lattice structural change, changes in the electronic structure occur as well during the annealing process. Monitoring these changes as a function of temperature should provide insight into possibilities for improving the annealing process to yield better devices.

To study the changes in the implanted layer that result from implantation and annealing, a host of optical tools are available. However, some of these optical methods probe only a small portion of the implanted layer. Chemical etches are then used to remove layers that have already been studied, and by successive etches, a profile of the total damage layer is determined. Unfortunately, the chemical etch itself can cause changes in the surface structure of the sample (e.g. increased roughness). The effects of these changes on optical properties must be understood in order to isolate the effects of doping and annealing on the optical properties of the implanted layer. Otherwise, structural profiles of this layer will not even be qualitatively correct.

The optical probes used in this dissertation are Raman scattering and ultraviolet-visible (ultraviolet for short) reflectivity. The absorption coefficient of GaAs for the incident photon energies used in these methods is quite high, and layers ranging in thickness from 100 to 3000 Å can be probed. Other optical tools such as infrared absorption involve probing the entire sample, and since the implanted layer thickness is only a very small fraction of the total sample thickness, the experimentally observed optical properties will be that of the bulk crystal rather than that of the implanted layer.

The important spectral features observed by Raman scattering and ultraviolet reflectivity are the following. The Raman LO (longitudinal optical) phonon peak characteristics change as damage is introduced. The full width at half-maximum increases, the peak position shifts towards lower frequencies, and the intensity diminishes. In resonance, the 2LO (LO phonon overtone) peak shifts as the incident photon energy is varied across the gap. The behavior of these shifts and the 2LO peak intensity are different even in slightly damaged material. In the implanted and annealed material, the LO peak intensity is reduced due to the damping out of the LO peak caused by phonon-plasmon interactions in a layer with a high enough carrier concentration ($N>10^{16}/cm^3$).

In ultraviolet reflectivity spectra, damage causes the linewidths of the E_1, $E_1+\Delta_1$, and E_2 peaks to broaden; the E_1 doublet feature washes out (see Figure 1.1 for the origin of these peaks). The

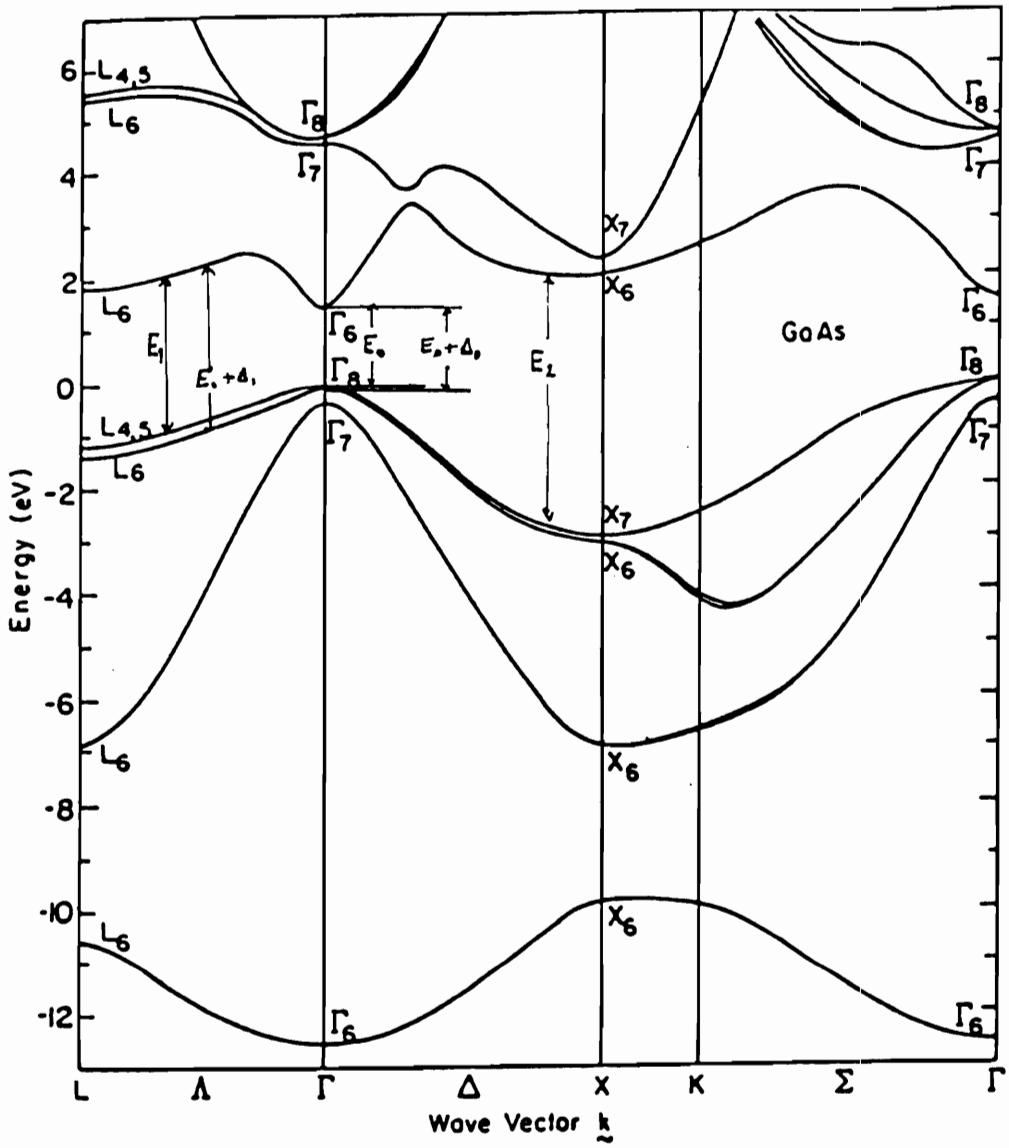

Fig. 1.1: Band structure of GaAs, adapted from Cohen and Chelikowsky. The critical points in the joint density of states are labelled with the energies corresponding to the direct interband transitions.

peaks in the spectra tend to appear flatter, and the slopes of linear regions decrease, approaching the slopes of the corresponding linear regions in the spectrum of amorphous (a-)GaAs.

The mechanisms which cause these spectral changes will be examined in detail in this dissertation, and a picture of the structural and electronic changes that occur during ion implantation, annealing and chemical etching will emerge.

1.2 Gallium Arsenide

1.2.1 Crystal Structure

GaAs crystallizes in the zincblende structure. This structure is composed of two interpenetrating face-centered cubic (fcc) sublattices [Wight], with the origin of the second sublattice displaced from that of the first by the vector (1,1,1)a/4 (in the coordinate system of the first sublattice, which is formed by three cube edges), where a is the length of a side of the cubes, and a = 5.65 Å for GaAs [Blakemore]. Each sublattice contains only one type of atom; atoms are located at the cube corners and the centers of the faces of each cube. The nearest neighbors of any atom will always be atoms of the other sublattice; the coordination number is 4, and nearest neighbor atoms form the corners of a tetrahedron. Figure 1.2 [Mayer and Lau] displays a cube of the GaAs lattice containing four tetrahedrons.

Such lattices belong to the space group T_d^2 (Schoenflies notation). [Burns] Since this space group is symmorphic, the factor group, formed by considering the cosets of the subgroup

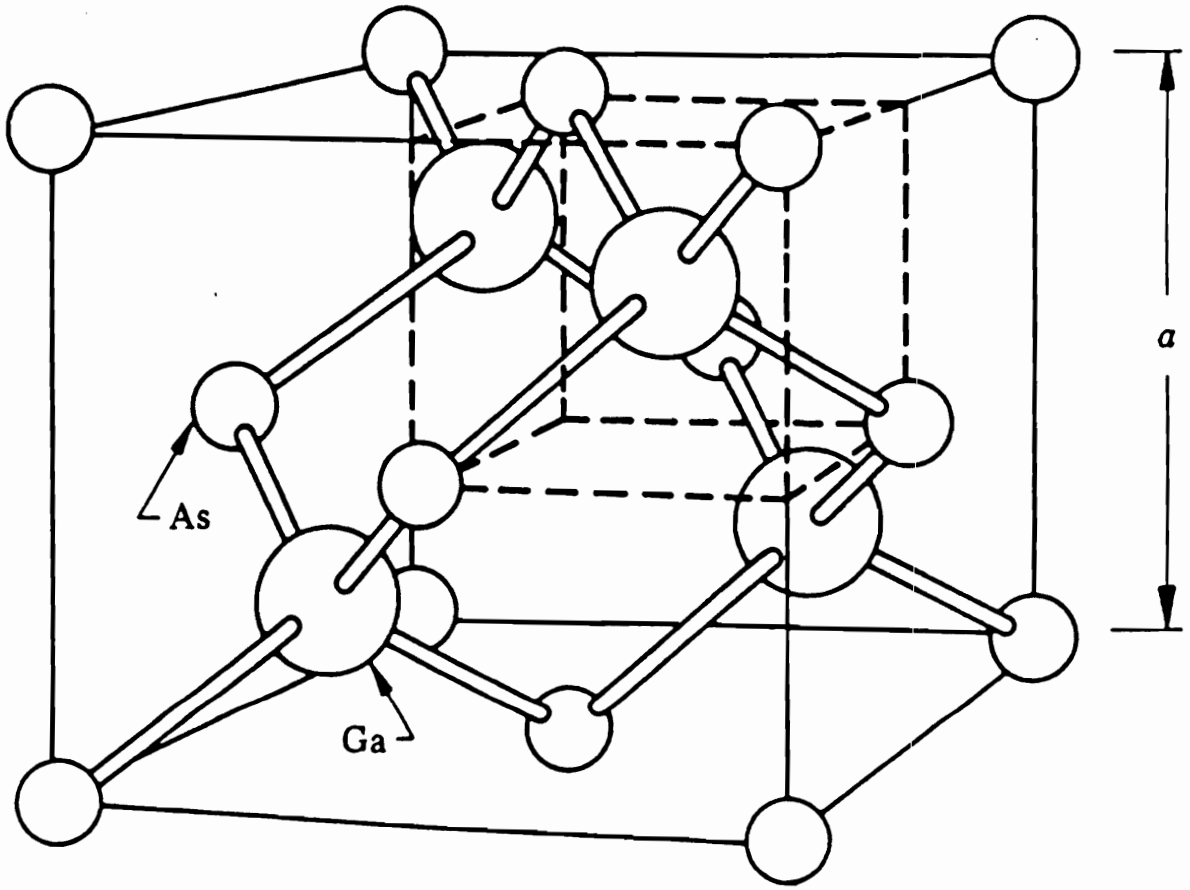

Fig. 1.2: The unit cube for GaAs and other zincblende lattices [Mayer and Lau].

consisting of translation operations which leave the lattice invariant, is isomorphic to the point group T_d. Hence the point group of the crystal is the group of symmetry operations of a tetrahedron.

The reciprocal lattice of an fcc lattice is a body centered cubic (bcc) lattice. The first Brillouin zone for GaAs is therefore the Wigner-Seitz cell of a bcc lattice and is shown in Figure 1.3 [Wooster]. The special points and lines marked in the figure are points and lines of high symmetry; that is, they transform back into themselves under several operations in the group. Characteristics of the crystal which are mapped in k-space (e.g. phonon dispersion, energy bands) are usually mapped along these points and lines.

1.2.2 Phonons

The phonon dispersion curve is shown in Figure 1.4 [Dorner and Strauch] and was measured using inelastic neutron scattering. Since GaAs is an ionic crystal which lacks a center of inversion, zero wavevector LO phonon vibrations polarize the material and set up an electric field, which does not cancel out in the crystal, parallel to the polarization vector. This electric field adds an extra restoring force for the LO vibrations. For TO phonons the electric field vanishes [Huang]. This explains the higher frequency for the LO peaks at the zone center (Γ point).

Optical phonons can be visualized as the motion of the sublattices in opposite directions, with the longitudinal displacements parallel to the wavevector and the transverse ones perpendicular

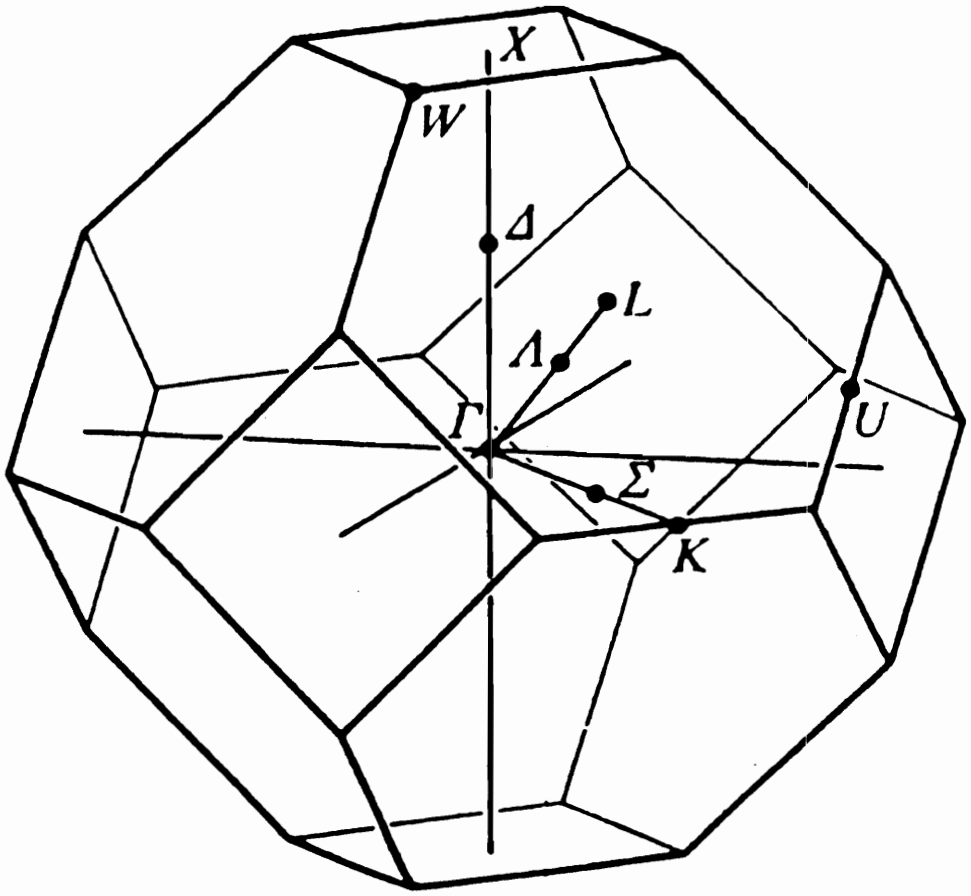

Fig. 1.3: The (first) Brillouin zone for all fcc lattices, marked with points and lines of high symmetry [Wooster].

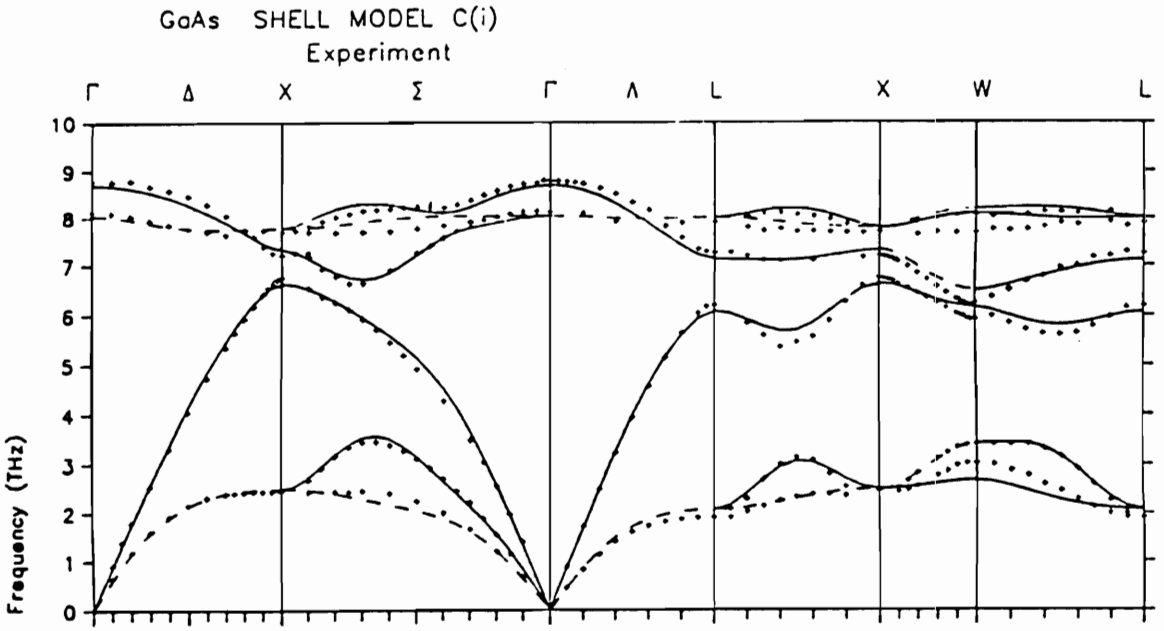

Fig. 1.4: Phonon dispersion curves for GaAs obtained through inelastic neutron scattering [Dorner and Strauch].

to it. For every crystal, the number of phonon branches is 3N, where N is the number of atoms in a unit cell. Three of these are acoustic, while the rest are optical. Hence, since GaAs is diatomic, it has three optical phonons. The phonon dispersion curve shows at most six phonon branches; where there are less it is due to the double degeneracy of the transverse phonons.

1.2.3 Electronic Structure

The relationship between the energy and the wavevector of electrons and holes in GaAs is shown in the band structure diagram of Figure 1.1 [Cohen and Chelikowsky]. Critical points in the electronic joint density of states are indicated on the diagram, and they represent a large probability for electronic transitions to occur between the valence and conduction bands. Of particular interest is the E_0 gap; it is the smallest energy difference between conduction and valence bands, allowing transitions to occur between the top of the valence band and the bottom of the conduction band without a change in wavevector. Hence, GaAs is a direct bandgap semiconductor.

Other critical points of interest in this work are the $E_0+\Delta_0$, E_1, $E_1+\Delta_1$, and E_2 gaps. Like E_0, $E_0+\Delta_0$ involves direct transitions, but this time it is between the bottom of the conduction band and the top of the spin-orbit split-off valence band. E_1 and $E_1+\Delta_1$ also involve direct transitions, but this time the value of the joint density of states is high for transitions between states separated by these energies because the conduction and valence

bands along the 4 equivalent (111) directions are parallel (equal slopes).

The effective masses of the electrons and holes are related to the inverse of the curvature of the bands. The electrons in the conduction band at the Γ point (large curvature) have a very small effective mass: $0.063m_0$ compared to a mass of $0.3m_0$ at the bottom of the conduction band in silicon [Wight]. Electrons should be able to respond faster in GaAs, making it more attractive to the semiconductor industry.

1.3 Raman Scattering

1.3.1 Non-resonant Raman Scattering

The theory behind Raman scattering will be explained in this section following the treatment of M. Cardona (1982) in outline form. He starts with the familiar expression for the differential scattering cross section, $d\sigma/d\Omega$, of a dipole vibrating at frequency ω such as the one given in chapter 9 of Jackson, and arrives at the following result:

$$\frac{d\sigma}{d\Omega} = \frac{\omega^4}{(4\pi\varepsilon_0)^2 c^4} \left| \hat{e}_s \cdot \tilde{\alpha} \cdot \hat{e}_L \right|^2 \qquad (1.1)$$

where $\tilde{\alpha}$ is the polarizability tensor of the dipole, $\hat{e}_s$ and $\hat{e}_L$ are the scattered and incident light polarization unit vectors, ε_0 is the static dielectric constant of the medium and c is the speed of light. Assuming the system is far from resonance, a phonon can be treated as a quasistatic deformation of the dipole. The

polarizability of the dipole will depend on the amplitude of the vibration at any given time. An expansion of the polarizability in a Taylor series in powers of the normal mode coordinate $\xi=\xi_0 \exp[-i\omega_v t]$ for a vibrational mode with frequency ω_v gives:

$$\tilde{\alpha}(\omega_L,\xi) = \tilde{\alpha}(\omega_L) \qquad (1.2a)$$

$$+ \frac{\partial\tilde{\alpha}}{\partial\xi}\xi_0 e^{-i\omega_v t} + \frac{\partial\tilde{\alpha}}{\partial\xi^*}\xi_0^* e^{i\omega_v t} \qquad (1.2b)$$

$$+ \frac{1}{2}\frac{\partial^2\tilde{\alpha}}{\partial\xi^2}\xi_0^2 e^{-2i\omega_v t} + \frac{1}{2}\frac{\partial^2\tilde{\alpha}}{\partial\xi^{*2}}\xi_0^{*2} e^{2i\omega_v t} \qquad (1.2c)$$

$$+ \frac{1}{2}\frac{\partial^2\tilde{\alpha}}{\partial\xi\,\partial\xi^*}(\xi\xi^* + \xi^*\xi) + \ldots.$$

The various terms in the expansion, when substituted in equation 1.1, give various Raman scattering terms for dipoles. The term in 1.2a describes Rayleigh scattering. Remembering that the incident field in 1.1 has the phase factor $\exp(i\omega_L t)$, the scattered radiation will have the frequencies $\omega_L \pm \omega_v$ in first order (1.2b), and $\omega_L \pm 2\omega_v$ for overtones (1.2c). The + and - signs give antistokes and Stokes scattering respectively. Higher order terms in the expansion yield multiphonon scattering.

An extension to crystals is obtained by considering the scattering of a collection of dipoles. However, the normal mode eigenvectors of the dipoles in the jth unit cell are related to those at the origin by Bloch's theorem. The vibrational amplitudes now also depend on the crystal momentum, **q**, and

a phase factor of $\exp[\pm i(\mathbf{q}\cdot\mathbf{R}_j - \omega_v(\mathbf{q})t)]$ is introduced for an atom in the jth unit cell with the position vector $\mathbf{R}_j$. Since the susceptibility, $\chi(\mathbf{r})$, is defined as the dipole moment per unit volume induced by a unit electric field, the scattered field can be expressed in terms of the Fourier component of the susceptibility which corresponds in k-space to $\chi(\mathbf{k}_L \pm \mathbf{q} - \mathbf{k}_s)$, where the subscripts L and s on **k** refer to the incident and scattered wavevectors respectively.

An expansion of the susceptibility similar to the one for the polarizability provides expressions for various orders of Raman scattering when the polarizability is replaced by the susceptibility in equation 1.1. With the phase factor $\exp(i\omega_L t)$ from the incident field, the scattered field will have the phase factor $\exp[-i(\omega_L \pm \omega_v(\mathbf{q}))t]\exp[i(\mathbf{k}_L \pm \mathbf{q})\cdot\mathbf{r}]$ for first order Raman scattering. This is consistent with the fact that in a crystal, $\chi(\mathbf{k}_L, \mathbf{k}_s, \mathbf{q})$ vanishes unless $\mathbf{k}_L \pm \mathbf{q} - \mathbf{k}_s$ is zero or a reciprocal lattice vector, **G**. From these factors, the laws of conservation of energy and wave vector are obtained:

$$\omega_s = \omega_L \pm \omega_v \tag{1.3}$$

$$\mathbf{k}_s = \mathbf{k}_L \pm \mathbf{q} + \mathbf{G} \tag{1.4}$$

The equations for two phonon scattering are obtained from these by replacing ω_v with $\omega_v + \omega_{v'}$ and **q** with **q** + **q**'; the expansion for the susceptibility would contain terms bilinear in the two vibrational modes v and v'. Note that since $|\mathbf{k}_L - \mathbf{k}_s| = q << 2\pi/a$ for first order scattering, $q \approx 0$ so only zone center phonons

can participate. In second-order, this restriction is removed, since wavevector conservation gives $\mathbf{q} + \mathbf{q}' \approx 0$ and therefore $\mathbf{q}' = -\mathbf{q}$ will allow even zone edge phonons to participate; as a result, the second-order Raman spectrum mimics $\rho(\omega_v/2)$ where $\rho(\omega)$ is the one-phonon density of states.

When the first order term in the susceptibility expansion is considered as a Raman tensor, $\tilde{R}$, and the normal mode coordinate is replaced by a phonon annihilation operator in a semi-classical approach, the following expression for first order Stokes Raman scattering is obtained:

$$\frac{d\sigma_s}{d\Omega} = \frac{\omega_s^4 V}{(4\pi)^2 c^4} \left| \hat{e}_s \cdot \tilde{R} \cdot \hat{e}_L \right|^2 (n + 1) \frac{\hbar}{2\omega_v} \tag{1.5}$$

where $n = 1/[\exp(\hbar\omega_v/kT) - 1]$, the Bose-Einstein statistical factor. It is clear from this treatment that Raman scattering arises from the modulation of the electric susceptibility of the crystal by the normal mode coordinates.

1.3.2 Resonant Raman Scattering

The various Raman scattering processes are depicted in Figure 1.5. The Feynman diagrams included in the figure show the electron (or hole)-phonon vertices; this kind of diagram will be useful in an alternative description of Raman scattering using quantum mechanics with the quasi-particle to quasi-particle (e.g. phonon-electron) interactions treated as third or fourth order perturbations [Martin and Falicov]. With the quantum

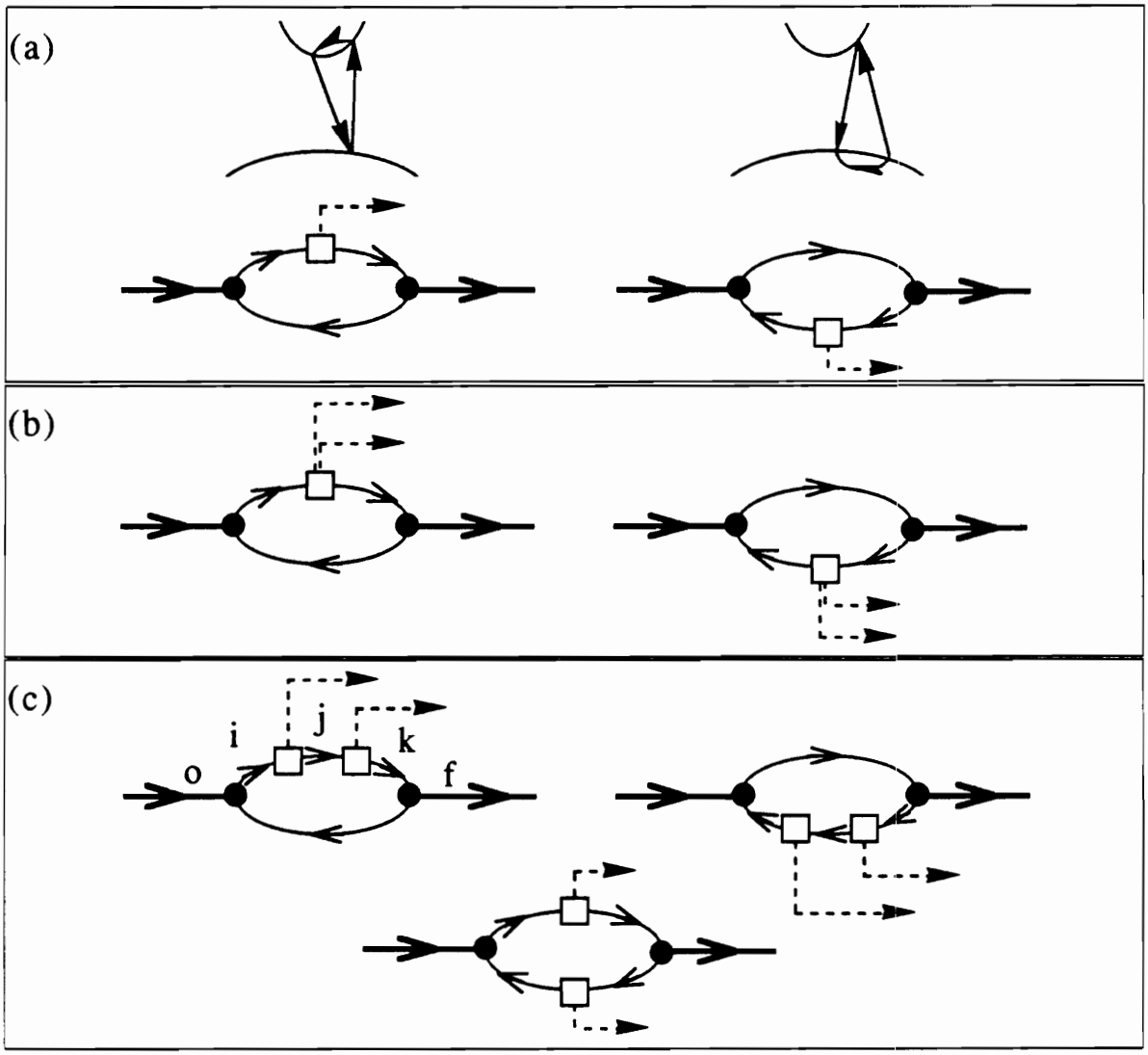

Fig. 1.5: Raman scattering processes. (a) interband transitions involved in first-order scattering and the corresponding Feynman Diagrams, (b) Feynman diagrams for electron-(left) or hole-(right) two-phonon interactions, and (c) diagrams for iterated scattering (clockwise from left): iterated electron-one-phonon interactions with states labelled f, i, j, k, and o, iterated hole-one-phonon interactions, and electron-one-phonon-hole-one-phonon interactions.Solid lines show photons, dashed lines represent phonons, solid circles stand for radiation-electron (hole) interaction vertices, and squares represent electron-(hole-) phonon interaction vertices.

mechanical states of the system labelled as in Figure 1.5c, and the transition matrix element between states a and b denoted by M_{ab} for electron-photon interactions and M_{ab} (italicized) for electron-phonon interactions, the radiation-material interaction Hamiltonian matrix element between initial and final states o and f of the system that experiences an iterated electron-one-phonon interaction is given by:

$$K = \sum_{ijk} \left[\frac{M_{fk} M_{kj} M_{ji} M_{io}}{\hbar^3 (\omega_1 - \omega_i - i\gamma_i)(\omega_1 - \omega_j - i\gamma_j)(\omega_1 - \omega_k - i\gamma_k)} \right] \tag{1.6}$$

where the energies of states i, j, and k are written in terms of the frequencies (ω_q) of the phonons involved. For resonance at the E_1 critical point in GaAs, these energies are:

$$\hbar\omega_i = E_1 + \frac{\hbar^2 k^2}{2M} \tag{1.7}$$

$$\hbar\omega_j = E_1 + \frac{\hbar^2 (\mathbf{k} + \mathbf{q})^2}{2M} + \hbar\omega_q \tag{1.8}$$

$$\hbar\omega_k = E_1 + \frac{\hbar^2 k^2}{2M} + 2\hbar\omega_q \tag{1.9}$$

where M is the mass of the free electron-hole pair. With the definitions

$$\frac{\hbar^2 \kappa_1^2}{2M} \equiv \hbar\omega_1 - E_1 - i\hbar\gamma \tag{1.10}$$

$$\frac{\hbar^2 \kappa_2^2}{2M} \equiv \hbar\omega_1 - E_1 - \omega_q - i\hbar\gamma \tag{1.11}$$

$$\frac{\hbar^2 \kappa_3^2}{2M} \equiv \hbar\omega_1 - E_1 - 2\omega_q - i\hbar\gamma \tag{1.12}$$

the matrix element K is proportional to

$$\frac{1}{(\kappa_1^2 - \kappa_3^2)} \int \left[\frac{\left(\frac{L}{2\pi}\right)^3 d^3k}{(k^2-\kappa_1^2)\left[(\mathbf{k}+\mathbf{q})^2 - \kappa_2^2\right]} - \frac{\left(\frac{L}{2\pi}\right)^3 d^3k}{(k^2-\kappa_3^2)\left[(\mathbf{k}+\mathbf{q})^2 - \kappa_2^2\right]} \right] \tag{1.13}$$

From this expression, it can be shown that resonance occurs for fixed $\mathbf{q}$ at E_1, $E_1 + \omega_q$ and $E_1 + 2\omega_q$ and also at the double resonances for phonons with wavevectors

$$q = \left(\frac{2M}{\hbar^2}\right)^{\frac{1}{2}} \left[(\hbar\omega_1 - E_1)^{\frac{1}{2}} + (\hbar\omega_1 - E_1 - \hbar\Omega_{LO})^{\frac{1}{2}} \right] \tag{1.14}$$

and

$$q = \left(\frac{2M}{\hbar^2}\right)^{\frac{1}{2}} \left[(\hbar\omega_1 - E_1 - \hbar\Omega_{LO})^{\frac{1}{2}} + (\hbar\omega_1 - E_1 - 2\hbar\Omega_{LO})^{\frac{1}{2}} \right] \tag{1.15}$$

For systems which involve only electron-one-phonon interactions, or two electron-one-phonon interactions which can be renormalized into one interaction (dressed vertex, [Renucci et al.]) similar results hold; the denominator will have only two resonating terms and the matrix elements $M_{kj}M_{ji}$ are replaced by M_{ki}.

A physical picture of the events that take place during

Raman scattering involves virtual intermediate states (Figure 1.5a). As light hits the sample, an electron makes a direct transition ($k \approx o$) from the valence to the conduction band. It then interacts with the material (phonons, magnons, etc.) bringing the system from one virtual state to another. Several interactions can take place (multiphonon scattering, Figures1.5b and c) before the electron goes back to the valence band and the scattered light leaves the sample. These interactions change the energy of the system; phonons can be created (destroyed) and hence the scattered light will be red (blue) shifted in a Stokes (anti-Stokes) process. If the direct transition involved is near a critical point in the electronic joint density of states, the transition matrix will be large. As the energy of the incident light approaches the critical point resonance occurs and the scattering is greatly enhanced.

1.3.3 Selection Rules

Because of the translational invariance of the crystal, only $k=0$ phonons are allowed to participate in first order scattering. Other considerations which determine what modes are Raman active and under which scattering configurations they appear provide a complete picture of the selection rules.

Following the analysis of Burns to determine the normal modes of a tetrahedral molecule (such as CH_4) would provide the irreducible representations of the local vibrational modes of a dopant in GaAs. For each atom, a set of three orthogonal

displacement vectors is assigned. The symmetry operations of the point group (T_d) are then performed on each displacement, and a reducible 15 by 15 matrix for each class of operations is obtained. Table 1.1 summarizes the characters for each class in the representation Γ_{LVM}. A reduction of this representation can be obtained by considering the great orthogonality theorem, and one obtains $\Gamma_{LVM} = A_1 + E + T_1 + 3T_2$. Of these 15 modes, those representations that have the infinitesimal rotations (Rx,Ry,Rz) as basis functions give pure rotational modes (T_1). Those which have (x,y,z) as basis functions are pure translational modes (T_2). Hence the 9 vibrational modes are $A_1 + E + 2T_2$.

Of these modes, the only ones allowed for k=0 (zone center) phonons in the crystal are those whose displacements preserve the translational invariance. The opposite faces of primitive cells must have their atoms moving in the same direction. The A_1 breathing mode and the two E modes do not meet this criterion; hence the only phonon modes of interest in the crystal are the $2T_2$ modes. This is to be expected since GaAs has six modes possible, and the T_2 representations are three dimensional.

The factor group analysis suggested by M. Cardona, 1982 for k=0 modes is a much simpler method but it does not provide the local vibrational modes. He splits the representation into a part that transforms as a vector and a part that determines the transformation among the atoms in a unit cell. Under all the operations of the point group, the positions of the Ga and As atoms remain unchanged. Hence they both transform as the

Table 1.1: Character table for the T_d point group [Wooster].

T_d	E	$8C_3$	$3C_2$	$6S_4$	$6\sigma_d$	Basis Functions	
A_1	1	1	1	1	1		$x^2+y^2+z^2$
A_2	1	1	1	-1	-1		
E	2	-1	2	0	0		$(2z^2-x^2-y^2,$ $x^2-y^2)$
T_1	3	0	-1	1	-1	(R_x,R_y,R_z)	
T_2	3	0	-1	-1	1	(x,y,z)	(xy,xz,yz)
Γ_{LVM}	15	0	-1	-1	3		

identity representation. In T_d, vectors transform as the T_2 representation. Therefore the k=0 phonons are represented by $A_1 \times T_2$ (Ga) and $A_1 \times T_2$ (As); this is consistent with the other analysis providing $2T_2$ as the normal modes.

A determination of which of these modes are Raman active is also accomplished through group theory. From equation 1.5, it is clear that for the scattering cross section to be invariant under the operations of the point group, the direct product of the representations of the incident and scattered polarization vectors and the Raman tensor, $\Gamma_{Vs} \times \Gamma_R \times \Gamma_{VL}$, must contain A_1, the identity representation. This is equivalent to the statement that the irreducible representation for the Raman tensor Γ_R, must be contained in $\Gamma_{Vs}^* \times \Gamma_{VL}$. Since the polarization vectors transform as T_2 [Lax], Γ_R must be contained in $T_2 \times T_2 = A_1 + E + T_1 + T_2$. This means that all the k=0 phonon modes are Raman active since they have T_2 symmetry.

In computing the selection rules, the Raman tensors with T_2 symmetry for the zincblende family must be used. The tensors in Table 1.2 are for three orthogonal modes and are immediately applicable to the (100) face backscattering selection rules. The tensor labelled u_x is appropriate for LO phonons, while the other two are for the TO phonons. Since any linear combination of these modes will produce modes with the same symmetry, the rules for the (211) face are obtained by considering the appropriate linear combinations. The tensor for the LO phonon in that case will be $2u_x + u_y + u_z$. Table 1.3 summarizes

Table 1.2: Raman Tensors for the optical phonon modes of zincblende crystals [Cardona, 1982].

Tensor	direction	phonon	face
$\Gamma(u_x) = \begin{bmatrix} & & \\ & & d \\ & d & \end{bmatrix}$	$\parallel$ to $\langle 100 \rangle$	LO	(100)
$\Gamma(u_y) = \begin{bmatrix} & & d \\ & & \\ d & & \end{bmatrix}$	$\parallel$ to $\langle 010 \rangle$	TO(y)	(100)
$\Gamma(u_z) = \begin{bmatrix} & d & \\ d & & \\ & & \end{bmatrix}$	$\parallel$ to $\langle 001 \rangle$	TO(z)	(100)
$\Gamma_{(211)} = \begin{bmatrix} & 1 & 1 \\ 1 & & 2 \\ 1 & 2 & \end{bmatrix} d$	$\parallel$ to $\langle 211 \rangle$	LO	(211)

Table 1.3: Selection rules for first order Raman scattering in zincblende crystals in a backscattering configuration for the (100) and (211) faces.

Configuration (100)	LO	TO
$z(x,x)\bar{z}$	0	0
$z(x,y)\bar{z}$	d^2	0
$z(y,y)\bar{z}$	0	0
$z(x',x')\bar{z}$	d^2	0
$z(x',y')\bar{z}$	0	0
$z(y',y')\bar{z}$	d^2	0

where x, y, x', y', z are unit vectors for (100):

x = (0,1,0) y = (0,0,1) ;

x' = $(0,1,1)/\sqrt{2}$ y' = $(0,-1,1)/\sqrt{2}$ z= (1,0,0)

Configuration (211)	LO	TO
$z(xx)\bar{z}$	$(2/3)\,(d_{LO})^2$	$(1/3)(d_{TO})^2$
$z(xy)\bar{z}$	0	$(1/3)(d_{TO})^2$
$z(yy)\bar{z}$	0	$(4/3)(d_{TO})^2$

where x, y and z are unit vectors for (211):

x = $(0,-1,1)/\sqrt{2}$

y = $(1,-1,-1)/\sqrt{3}$

z = $(2,1,1)/\sqrt{6}$

the selection rules for both the (100) and (211) faces of GaAs in a backscattering configuration. The Porto notation for the configurations is used; e.g. $x(yz)\bar{x}$ means that the incident (scattered) light wavevector is in the positive (negative) x direction and is polarized along the y (z) axis.

For two phonon processes the selection rules calculated by Birman (1974, 1963) show that all overtones and combinations are Raman active in zincblende at the Γ, X, L and W points in the Brillouin zone. The excitation symmetry for such processes is contained in the direct product of the irreducible representations (of the space group) of the participating phonons [Hayes and Loudon]. For the zone center phonons in GaAs, overtones and combinations will all have $T_2 \times T_2$ symmetry. Since this product is exactly that for which Raman scattering is allowed (product of the irreducible representations of two polar vectors), all zone center overtones and combinations are allowed. For non-zero wavevector phonons it can be shown that all second-order scattering is allowed [Loudon, 1965] since the space group excitation symmetries will contain all the Raman active point group (zone center) symmetries; restrictions may occur, however, at high symmetry points in the Brillouin zone.

1.4 Ultraviolet-Visible Reflectivity

This section outlines the explanation given by Cohen and Chelikowsky for the significance of reflectivity spectra. (See also Greenaway and Harbeke, 1968.) The optical functions which

aid in an analysis of reflectivity spectra are the complex index of refraction $N(\omega) = n(\omega) + ik(\omega)$ and the complex dielectric function $\varepsilon(\omega) = \varepsilon_1(\omega) + i\varepsilon_2(\omega)$. Here they are written as wavevector independent since the wavevectors for the range of incident photon energies involved are much smaller than the Brillouin zone size (2π/lattice constant); only direct transitions (except for indirect minimum gaps as in silicon) are involved. The relationships between these functions are expressed in the equations:

$$N^2 = \varepsilon_1 + i\varepsilon_2 \tag{1.16}$$

$$\varepsilon_1 = n^2 - k^2 \tag{1.17}$$

$$\varepsilon_2 = 2nk \tag{1.18}$$

$$R = \frac{(n-1)^2 + k^2}{(n+1)^2 + k^2} \tag{1.19}$$

It is clear that the (near normal incidence) reflectivity, R, contains information about $\varepsilon(\omega)$, and with the aid of the Kramers-Kronig relation

$$\varepsilon_1(\omega) = 1 + \frac{2}{\pi} P \int_0^\infty \frac{\omega' \varepsilon_2(\omega')}{\omega'^2 - \omega^2} d\omega' \tag{1.20}$$

$\varepsilon(\omega)$ can be completely determined with a complete knowledge of $\varepsilon_2(\omega)$.

The imaginary part of the dielectric function, $\varepsilon_2(\omega)$, deals with the absorption processes that cause transitions between

initial valence band (i) states and final conduction band (j) states. An expression for $\varepsilon_2(\omega)$ is given [Ehrenreich and Cohen] in terms of an integral over all states in the Brillouin zone as:

$$\varepsilon_2(\omega) = \frac{4\pi^2 e^2 \hbar}{3m^2\omega^2} \sum_{ij} \frac{2}{(2\pi)^3} \int_{BZ} \delta[\omega_{ij}(\mathbf{k}) - \omega] \left| P_{ij}(\mathbf{k}) \right|^2 d^3k \qquad (1.21)$$

where $\omega_{ij}(\mathbf{k})$ is the difference between the energies of states i and j divided by Planck's constant, and $P_{ij}(\mathbf{k})$ is the dipole matrix element, a function that varies slowly and smoothly except near points of high symmetry. By isolating that part of $\varepsilon_2(\omega)$ which gives the major structure, the electronic joint density of states is obtained and can be written as:

$$J_{ij}(\omega) = \frac{2}{(2\pi)^3} \int_{\omega_{ij} = \omega} \frac{ds}{\left| \nabla_k \omega_{ij}(\mathbf{k}) \right|} \qquad (1.22)$$

where the integral is over the surface in wavevector space defined by $\omega_{ij}(\mathbf{k})=\omega$. The zeros in the denominator give rise to the sharp structure in the joint density of states; these critical points can be described by the condition $\nabla_k E_i = \nabla_k E_j$. This means that where the slopes of the ith and jth bands are equal, distinctive features should appear in $\varepsilon_2(\omega)$ as well as in the reflectivity. Hence, reflectivity spectra contain information about the band structure of the solid.

Unfortunately, for a Kramers-Kronig analysis, experimental data must span a wide range of frequencies. The 4 eV range

in this dissertation does not allow for meaningful Kramers-Kronig analysis. An alternative method based on expressing the dielectric function as a sum of Lorentzian harmonic oscillators [Spitzer and Kleinman, Verleur, Feng and Zallen] has proved to be quite fruitful since the oscillators can represent direct transitions at critical points in the joint density of states and give information about the energy of the transition and the lifetime of the electron involved in the process. A detailed description of such an analysis is given in chapter three.

1.5 Spectra of Processed Gallium Arsenide

1.5.1 Ion-Implanted GaAs

Ion implantation introduces damage into a crystal by leaving pockets of microcrystalline material while making the rest of the target amorphous. Spectra from these mixed materials can be interpreted using an effective medium approximation.

Raman spectra for ion-implanted GaAs contain a contribution from amorphous GaAs (a-GaAs). When the three broad bands characteristic of a-GaAs (Figure 1.6, Holtz) are subtracted from the spectra of mixed material, an intensity-reduced, asymmetrically broadened and downshifted LO peak is left. This peak comes from the microcrystalline portion of the sample, and the characteristics are changed by size effects and the uncertainty principle.

Richter, et al. analyzed these changes in ion-implanted Si while Tiong, et al. extended the results to GaAs. Size effects were dealt with by introducing a spatial confinement function

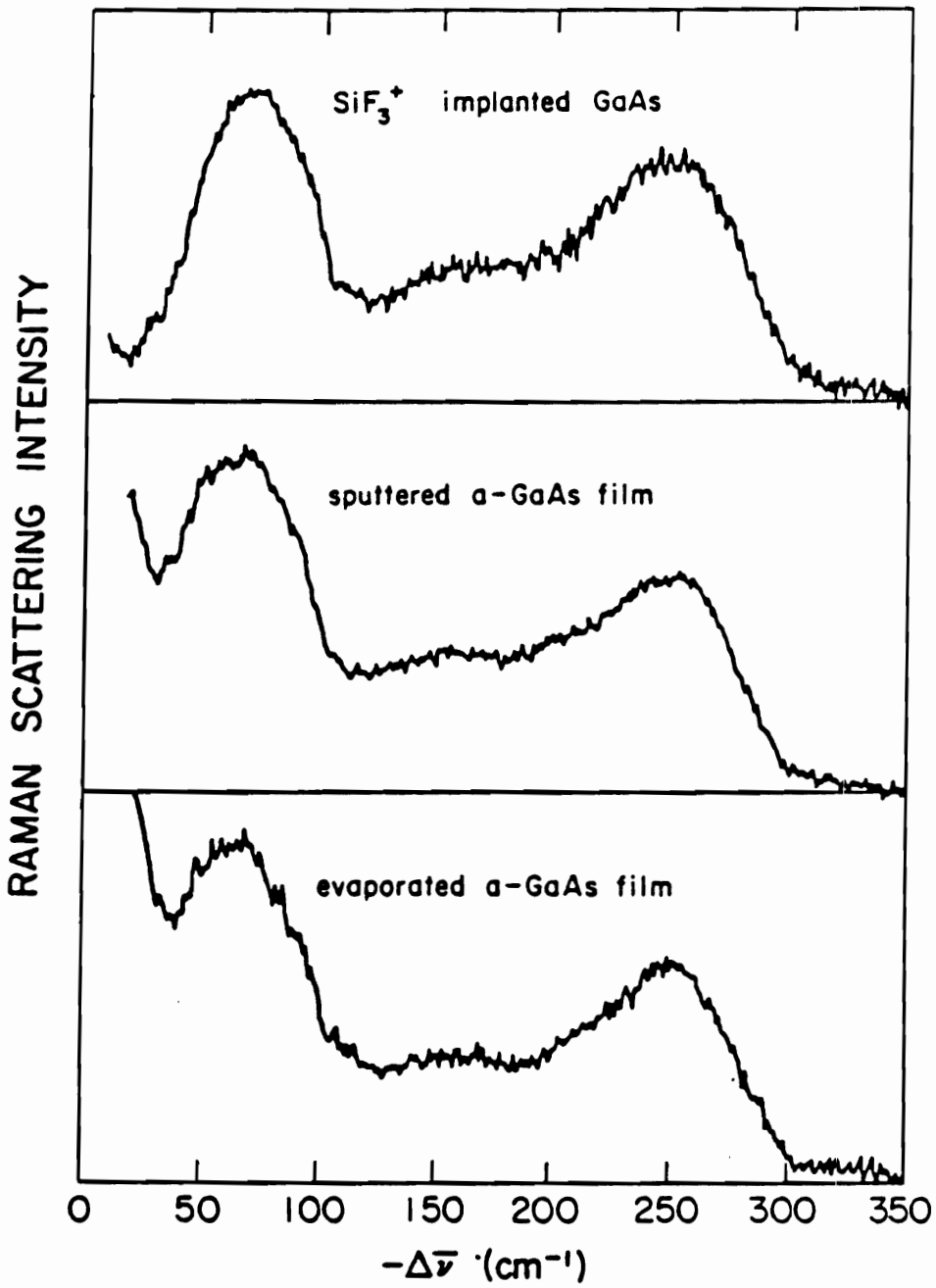

Fig. 1.6: Raman spectra for a-GaAs prepared in three different ways [Holtz].

which would cause the Bloch wave functions of the infinite crystal to damp out beyond a mean microcrystal diameter, L. The LO line intensity of such a microcrystal is proportional to:

$$\int_0^1 \exp\left(\frac{-q^2L^2}{4}\right) \frac{d^3q}{[\,\omega - \omega(q)\,]^2 + [\,\Gamma_0/2\,]^2} \tag{1.23}$$

where Γ_0 is the LO linewidth in the crystal. The integral is done over the whole Brillouin zone, with q in units of $2\pi/a$ where a is the lattice constant. The Fourier transform of the confinement function is proportional to the Gaussian term in the integral and the LO phonon dispersion $\omega(q)$ is given in cm^{-1} by

$$\omega(q) = 269.5 + 22.5 \cos(\pi q) \tag{1.24}$$

for the LO phonon along $\langle 100 \rangle$. A plot of the full width at half maximum and the shifts in the LO peak versus the microcrystal diameter can be obtained from this relation by varying L. Figure 1.7 shows the result, along with experimental points from Tiong, et al.

The confinement function destroys the zero-wavevector selection rule in the microcrystal; phonons with non-zero wavevectors can now participate in scattering events. Because the phonon dispersion for LO phonons decreases with increasing crystal momentum the presence of the confinement function causes an asymmetric broadening and a downshifting of the LO peak. Physically, this is the

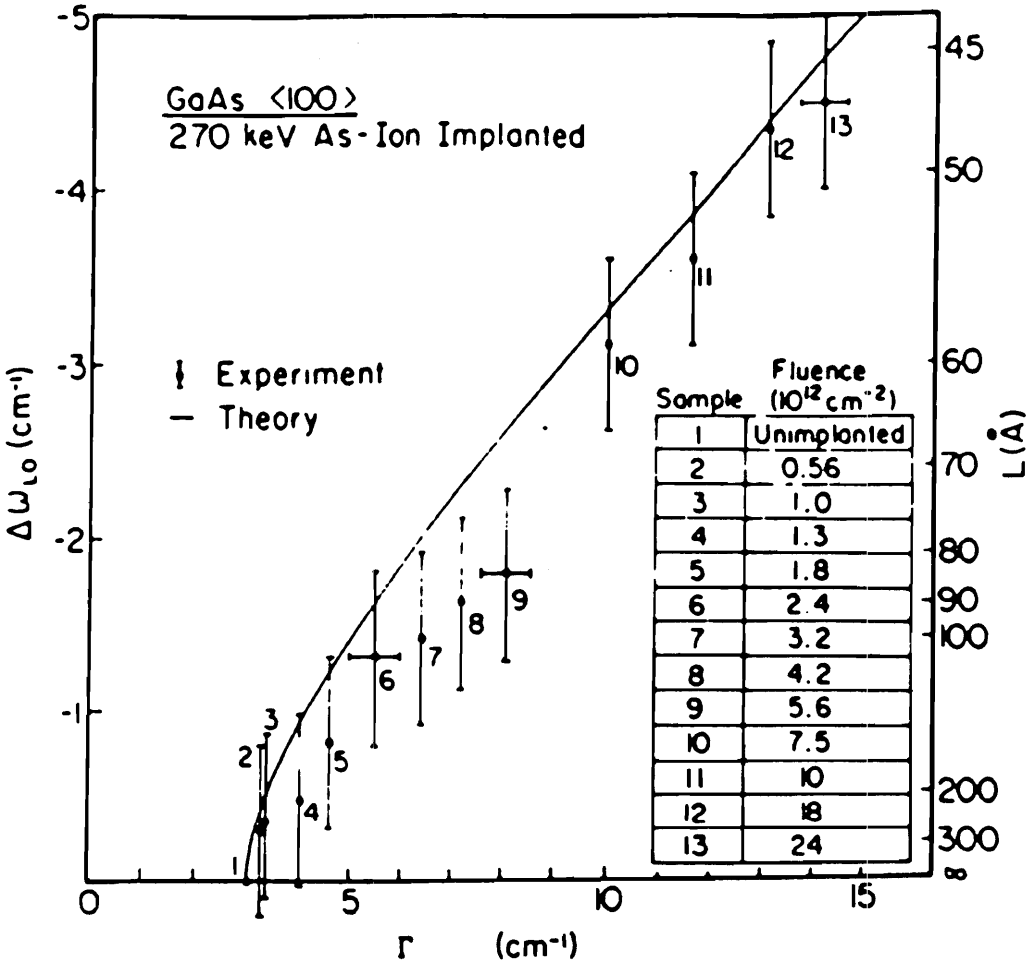

Fig. 1.7: Dependence of Raman LO peak linewidth and position on microcrystal size [Tiong et al.].

uncertainty principle in action. A confinement of the phonons leads to a smaller uncertainty in their position and therefore a greater uncertainty in their momentum. Hence, the selection rule that allows only zone center phonons to participate in Raman scattering is now destroyed. LO phonons with lower frequencies can participate, and the Raman LO peak scattering cross section is an integral including all these allowed phonons. As phonons with greater momentum are allowed (i.e. as the phonons are confined to smaller microcrystals), the LO peak broadens and downshifts. Hence the amount of broadening and downshifting increases as the microcrystals decrease in size. As for the reduction in Raman intensity from the value in unimplanted samples, this is mainly a volume effect; a smaller volume fraction of microcrystalline material will produce less scattering.

Ultraviolet reflectivity spectra are changed in a similar manner. Again, the uncertainty principle plays a part. After the Bruggeman effective medium approximation is applied to the dielectric functions derived from the spectra, knowing the a-GaAs contribution and the total dielectric function for the mixed material yields the dielectric function of the microcrystals. The linewidths of the oscillators which correspond to the interband transitions increase with decreasing microcrystal size. As the microcrystal size decreases, a collision of an electron (hole) with the boundary of the microcrystal is more likely to occur in a shorter amount of time. A shorter lifetime means a greater

uncertainty in the energy of the electron, hence the linewidth of the oscillator broadens. The features in the real and imaginary parts of the microcrystalline dielectric function will flatten out compared to c-GaAs, and when mixed with the featureless dielectric function of a-GaAs (through the Bruggeman effective medium approximation) cause the resulting interband reflectivity peaks to broaden.

1.5.2 Ion-implanted and Annealed Gallium Arsenide

The presence of carriers in a sample does not affect spectra obtained when the probing depth of the incident photon does not go beyond the depletion layer. In this layer, spectra will be identical to those obtained in a virgin crystal. Typical depletion layers are not thin enough (>150 Å) to cause changes in the reflectivity spectra, since the probe depth of the incident photons with energies near the interband reflectivity peaks is less than 100 Å. For that part of the reflectivity spectra above the fundamental band gap which probes beyond the depletion width, an oscillator analysis reveals that no oscillators with energies that correspond to a probe depth greater than the depletion width are needed to model the spectra. The lowest energy oscillator needed corresponds to the E_1 peak and a probe depth of about 100 Å; hence ultraviolet reflectivity spectra are unaffected by the presence of dopants.

Raman spectra, on the other hand, can be affected when the carrier regions ($N > 10^{16}$ cm^{-3}) are examined. The phonon-

plasmon interactions cause the LO phonon to damp out exponentially in this region, thus reducing the intensity of the LO signal in the doped material compared to that in virgin GaAs. A theoretical treatment of the behavior of the LO phonon in regions of high carrier concentration is given by Mills, while a calculation of the depletion width from the observed LO intensity reduction is treated by Pinczuk, et al. Carrier concentrations can then be estimated from the depletion width, and for Si-implanted GaAs, such a calculation is made by Shen, et al. Figure 1.8 shows their results. A concise description of the calculations involved in getting the carrier concentration from the observed LO intensity reduction can be found in chapter four.

1.6 Dissertation Outline

The objective in this study was two-fold: to determine the structural and electrical changes that occur in GaAs after it undergoes device processing steps such as ion-implantation and annealing, and to understand the effect of these changes on the optical properties of the material. An understanding of these effects enables one to describe the structural and electrical properties of processed GaAs and to identify and develop optical characterization methods suitable for studying such systems.

The details of all the experiments performed in this work are found in chapter two. The equipment and the methods of measurement are described there, while a brief review of experimental methods specific to each of the remaining chapters are described

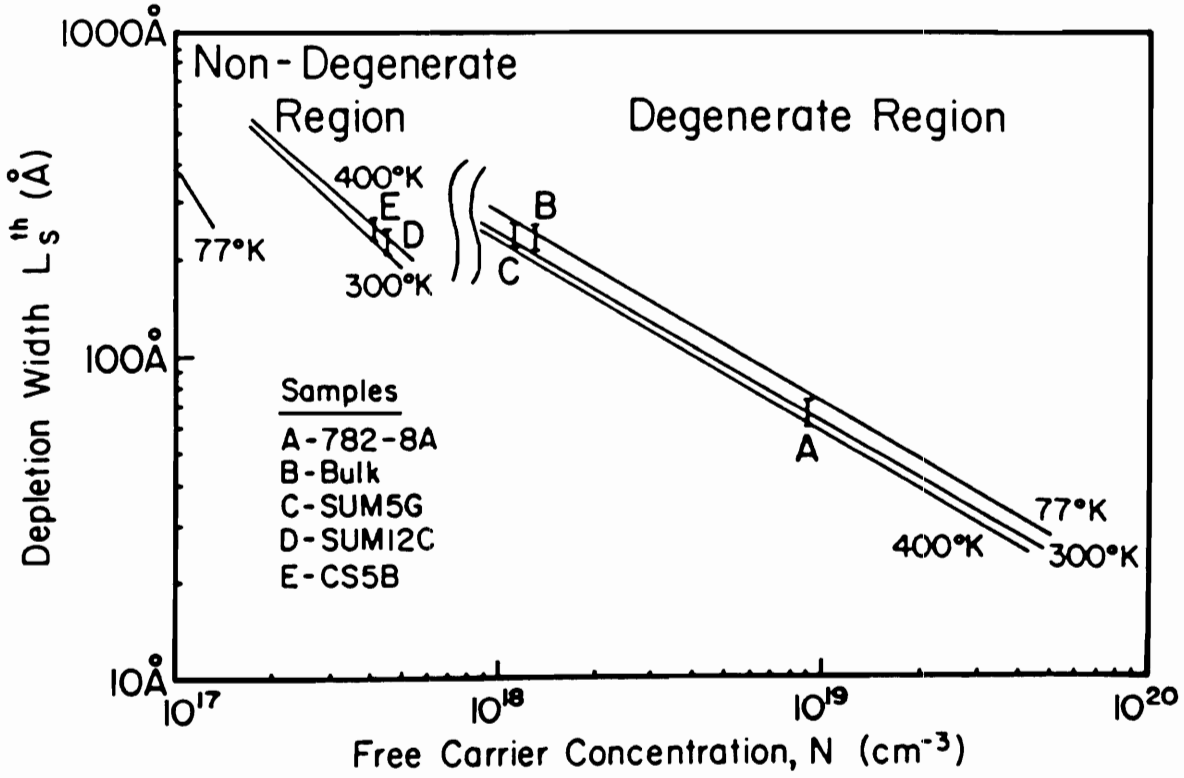

Fig. 1.8: Carrier concentration versus depletion layer width for Si-implanted GaAs [Shen et al.].

in the experimental section of each chapter.

The oscillator analysis of reflectivity spectra is used in chapter three to develop a method of damage depth profiling in Be-implanted GaAs. The depth profiles using various oscillator parameters are compared with the Raman LO peak damage profile determined by Holtz for the same samples, and the relationship between Raman LO shifts and the oscillator parameters is discussed.

The method developed in that chapter is then used in chapter four along with other well established methods of interpreting Raman spectra in order to characterize the structural recovery and electrical activation of Si-implanted GaAs as a function of annealing temperature. The recrystallization kinetics are also examined.

In chapter five, a comparison of the structural and electrical characteristics of (211) and (100) oriented Si-implanted GaAs is performed. A new method of qualitatively determining damage depth profiles for reflectivity spectra of samples with rough surfaces is developed to facilitate the comparison.

With the methods of the previous chapters, Si-implanted GaAs annealed at 525°C for 20 minutes would appear to be completely recrystallized. In chapter six, the shifts in the frequency of the two-LO-phonon Raman peak as the incident photon energy is varied near the E_1 gap (2.89 eV) are examined. This method is developed to study the residual damage in the 525°C annealed sample.

Finally, chapter seven summarizes the methods used, their applicability in studying the different effects caused by processing GaAs, and the major conclusions of the different experiments.

CHAPTER TWO
EXPERIMENTS : METHODS AND INSTRUMENTS

2.1 Sample Preparation

Several samples were used in the experiments, and a brief description of each is provided in Table 2.1. All samples were liquid encapsulated Czochralski (LEC) grown, chromium-doped, semi-insulating (SI) gallium arsenide single crystals (c-GaAs) which were implanted at room temperature with either 45 keV $^{9}Be^{+}$ ions or 50 keV $^{29}Si^{+}$ ions at Texas Instruments (TI). The implant energies and fluences used for each chapter are detailed in Table 2.1. Other than half of the samples used in chapter five, all of them were (100)-oriented. The other half in chapter five were (211)-oriented. Prior to implantation, the samples were cut from ingots (perpendicular to the ingot for (100) samples, and at about 35° away from the (100) plane for (211) samples). They were then polished to remove gross defects, and were finally etched in 8:1:1 H_2SO_4:30%H_2O_2:H_2O to remove leftover pits and scratches. All samples obtained in this way had smooth and shiny surfaces and were well-suited for optical experiments.

During implantation, the ion beam was tilted away from the normal to the sample surface at an angle between seven and nine degrees. This is done in order to avoid any channeling effects; if the ions were implanted at an angle below a threshold angle (which depends on the distance between the atoms that

TABLE 2.1: Summary of GaAs samples used in the experiments.

Dopant	Face	Energy, keV	Fluence, cm^{-2}	Anneals	Used in Chapters:
Si	(100)	50	1.7 E 13	none; RTA, 850 °C	five
Si	(211)	50	1.7 E 13	none; RTA, 850 °C	five
Si	(100)	50	4.0 E 13	none	four, five
Si	(100)	50	4.0 E 13	SFA, 525 °C	four, six
Si	(100)	50	4.0 E 13	SFA, 200, 400, 775, 1000 °C, (electrical studies: 350, 850°C)	four
Si	(211)	50	4.0 E 13	none	five
Be	(100)	45	5.0 E 14	none	three

form the sides of the channel), they could enter a channel in the crystal without colliding with the target atoms. Below the threshold angle, the steering action of the atoms due to coulombic repulsion allows the ions to travel deeper into the crystal. Above this angle, the target appears to have a random arrangement of atoms, much like an amorphous solid would. The prediction of the distribution of the ions with depth is made simpler since no channeling has to be accounted for, and one can use the Lindhard-Scharff-Schiott (LSS) theory [Lindhard et al., Gibbons et al., Gibbons].

After implantation, some of the samples were annealed. For a comparison of device characteristics between the (211)- and (100)-oriented Si-implanted GaAs (chapter five), TI annealed the samples in a rapid thermal annealing (RTA) system at temperatures of 750, 850, and 950 °C for 30 seconds. These anneals were performed with silicon nitride caps to prevent the outdiffusion of arsenic at the surface which can cause degradation of the optical and electrical characteristics of the surface layer [Duncan and Westphal]. The caps were removed using hydrofluoric acid after the annealing process and before optical measurements.

For the annealing studies in chapter four, the anneals were done in the Electronic Materials Lab of the Electrical Engineering Department of Virginia Tech. These were standard furnace anneals (SFA) carried out for 20 minutes at various temperatures. This time, arsenic loss was prevented by the proximity method

in which the sample to be annealed was sandwiched between samples of LEC SI c-GaAs. The samples were in an atmosphere of forming gas (five percent H_2, 95% N_2) during the anneal. Anneal temperatures were monitored with an Omegatherm thermocouple placed near the samples at the center of the Thermodyne furnace for the 200 and 400 °C anneals. The anneals done with temperature readings of 450, 650, and 850 °C were done with the thermocouple displaced away from the samples in the Lindberg furnace during the anneal, and actual temperatures at the sample area were estimated to be 525, 775, and 1000 °C respectively by recalibrating the temperatures at different zones in the furnace. (Anneals at 350 and 850°C were also done for electrical measurements.)

To carry out depth profiling experiments, a calibration of the etch rate (amount of material removed as a function of time) for the Si-implanted GaAs samples and an etchant solution of 1:1:100 H_2SO_4:30%H_2O_2:H_2O [McLevige] was carried out. (The etch rate for the Be-implanted samples is 660 Å/min [Holtz].) The calibration involves coating the samples with Microposit polymethyl methacrylate photoresist, covering half of each sample surface with rubylith, exposing them to ultraviolet radiation and dissolving the exposed photoresist in Microposit developer. This means only half of the surface along the length of the sample will be exposed to the etchant. The sample is then placed in the etchant (with the surface of the water perpendicular to the length of the sample) and five mm. of the sample is dipped into the etchant every 20 seconds, with the aid of a rack

and pinion mount, for a total of 80 seconds. Then the sample is rinsed in deionized water and immediately dried using lens-cleaning paper. The remaining photoresist is dissolved in acetone. This procedure yields a series of steps along the length of the sample as in Figure 2.1. The step heights were measured using a WYKO Topo-3D optical profilometer; it has an error margin (average point by point difference between two successive profiles of the same area) of three to six Å using a 10 x magnification lens which gives a probe area of one mm^2. Step heights as a function of time are plotted in Figure 2.2 for both (100) and (211) implants. The slopes of these graphs have a difference (.01 Å/s) that is well within experimental error in the rates between the two implants. The etch rate is 10 Å/s (600 Å/min, similar to, but slower than the rate for the Be-implanted samples).

Using LSS theory, Gibbons et al. tabulated the projected range statistics for several different combinations of ions and implantation targets. The projected range (the peak position in the Gaussian distribution of dopants along an axis normal to the surface) and standard deviation for 50 keV $^{28}Si^{+}$ implanted into GaAs is 424 and 254 Å respectively. The slight difference in atomic masses for the TI implant conditions ($^{29}Si^{+}$ in order to distinguish these ions from $^{28}N_2$ in a mass spectrometer) will negligibly alter the range statistics. Also, since the implants were done with the ion beams angled away from the surface normal, LSS theory applies. Hence the total damage depth in the TI samples is about 1200 Å (424 Å + 3 * 254 Å). The

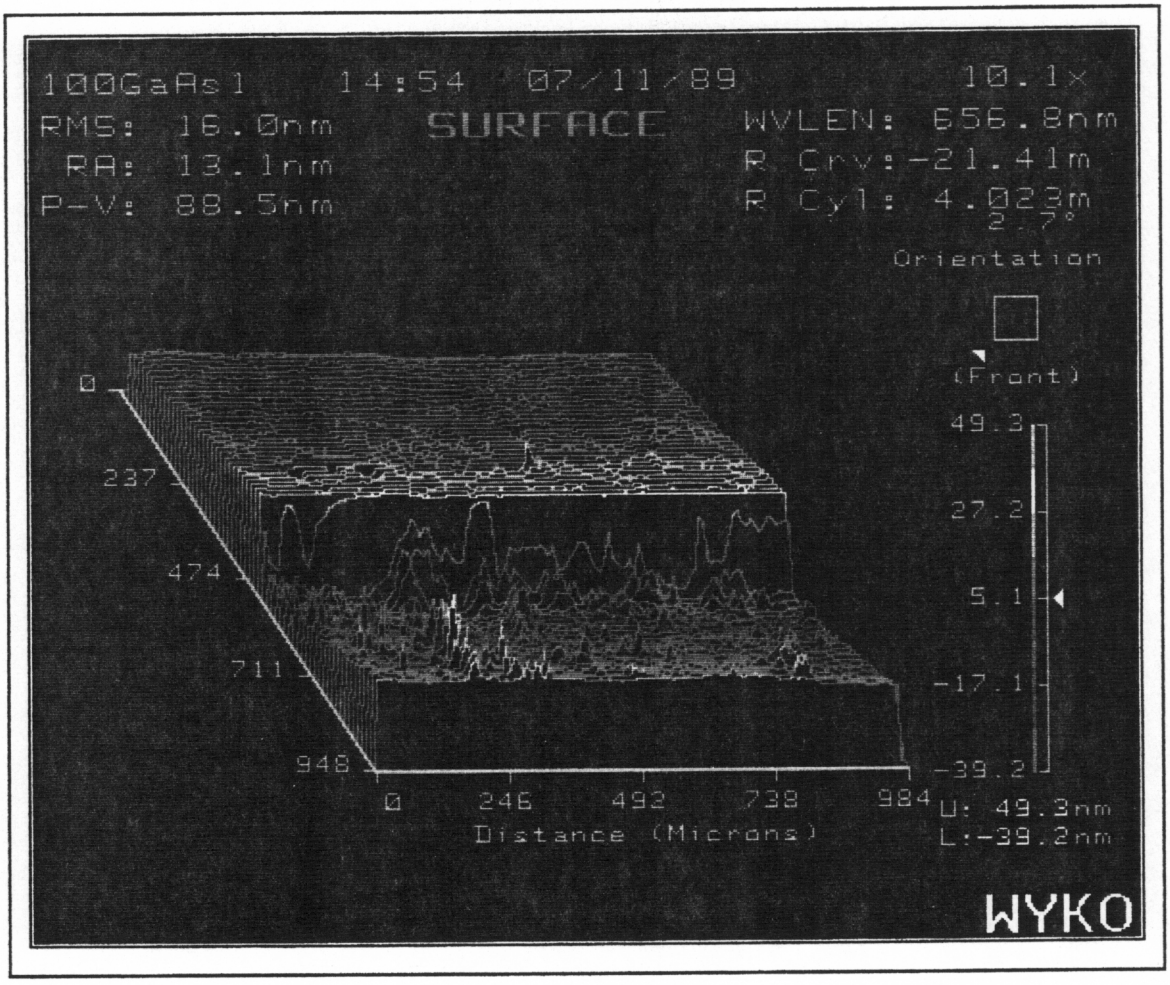

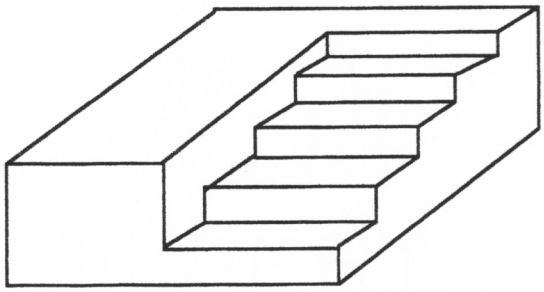

Fig. 2.1: Top: Topographical profile of a section of the (100) Si-implanted GaAs sample after the etch calibration for the etchant solution 1:1:100 H_2SO_4:30%H_2O_2:H_2O. Bottom: artist's sketch of the step-like surface of the etched sample.

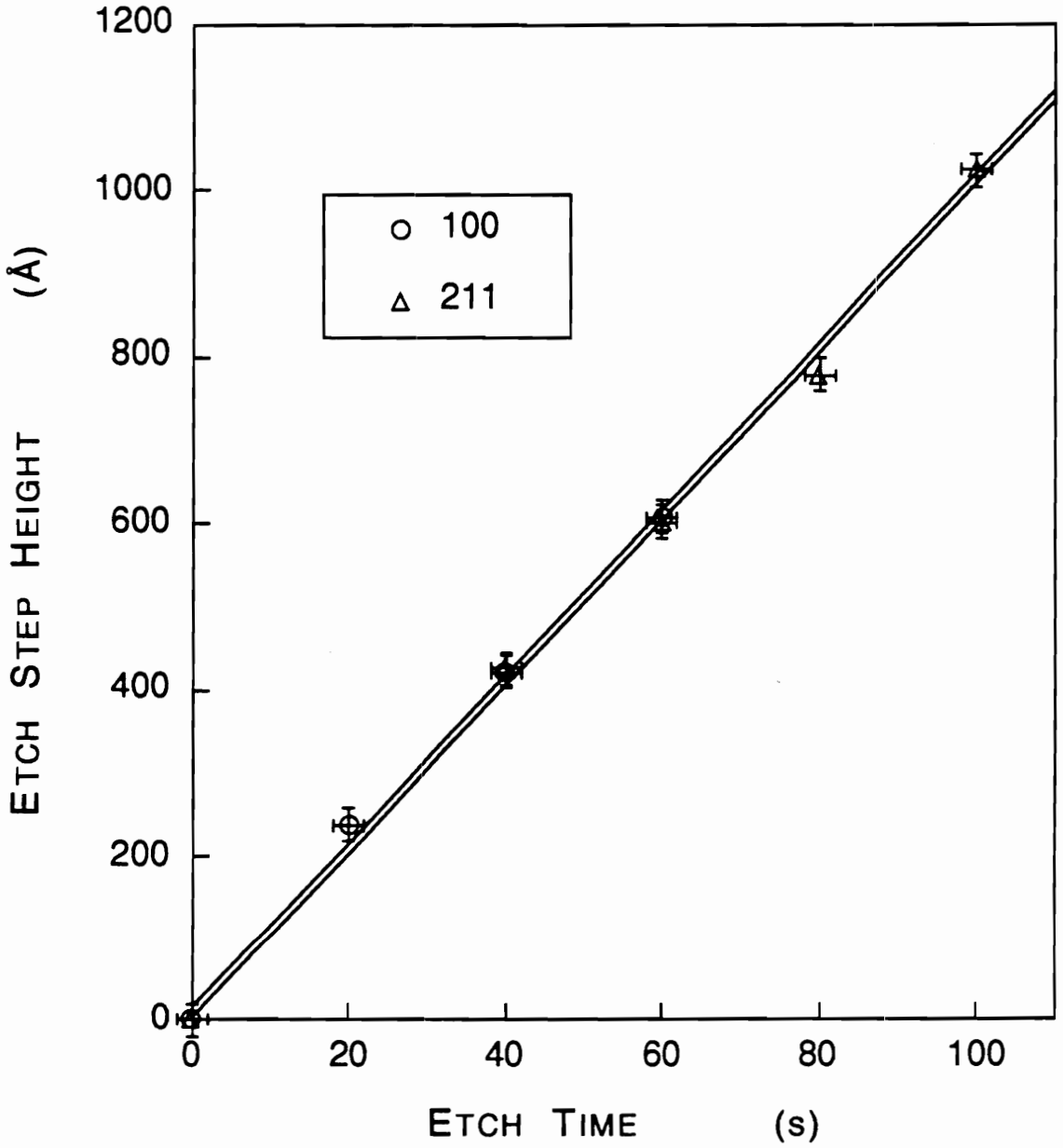

Fig. 2.2: Etch step heights as a function of etch time for both (100) and (211) faces (circles and triangles, respectively) of GaAs. The slopes of these curves yield an etch rate of 10 Å/s for both faces.

maximum etch step in the calibration is 800 Å, so only the implanted material was monitored. C-GaAs has a lower etch rate of 530 Å [Holtz] and the calibration would have been affected by etching more than 1200 Å.

From these results, it was determined that depth profiling measurements should be done at intervals of 20 seconds (200 Å) for the Si-implanted samples. Since the etch procedure is somewhat imprecise with respect to the time scale (the time intervals for dipping, removing, and drying are not easily controlled), the etch steps are only approximately 200 Å, and the percent error in depth is larger (about 20 Å absolute error) for these samples than for the Be-implanted ones which use one-minute etch intervals. The Be-implanted samples are the same ones used by Holtz.

2.2 Raman Scattering

In this section, only a brief account of the equipment will be given; the full details can be found elsewhere [Holtz]. Figure 2.3 provides a schematic of the experimental set-up. The discussion here will center on the experimental methods which affect the interpretation of the data.

For the experiments done in chapters four and five the SPEX 1403 0.85 meter double monochromator was used. In chapter six, the 1404 was used; both machines have a spectral range of 11,000 to 31,000 cm-1. The difference between them is the resolving power. The 1403 uses 1800 lines/mm gratings,

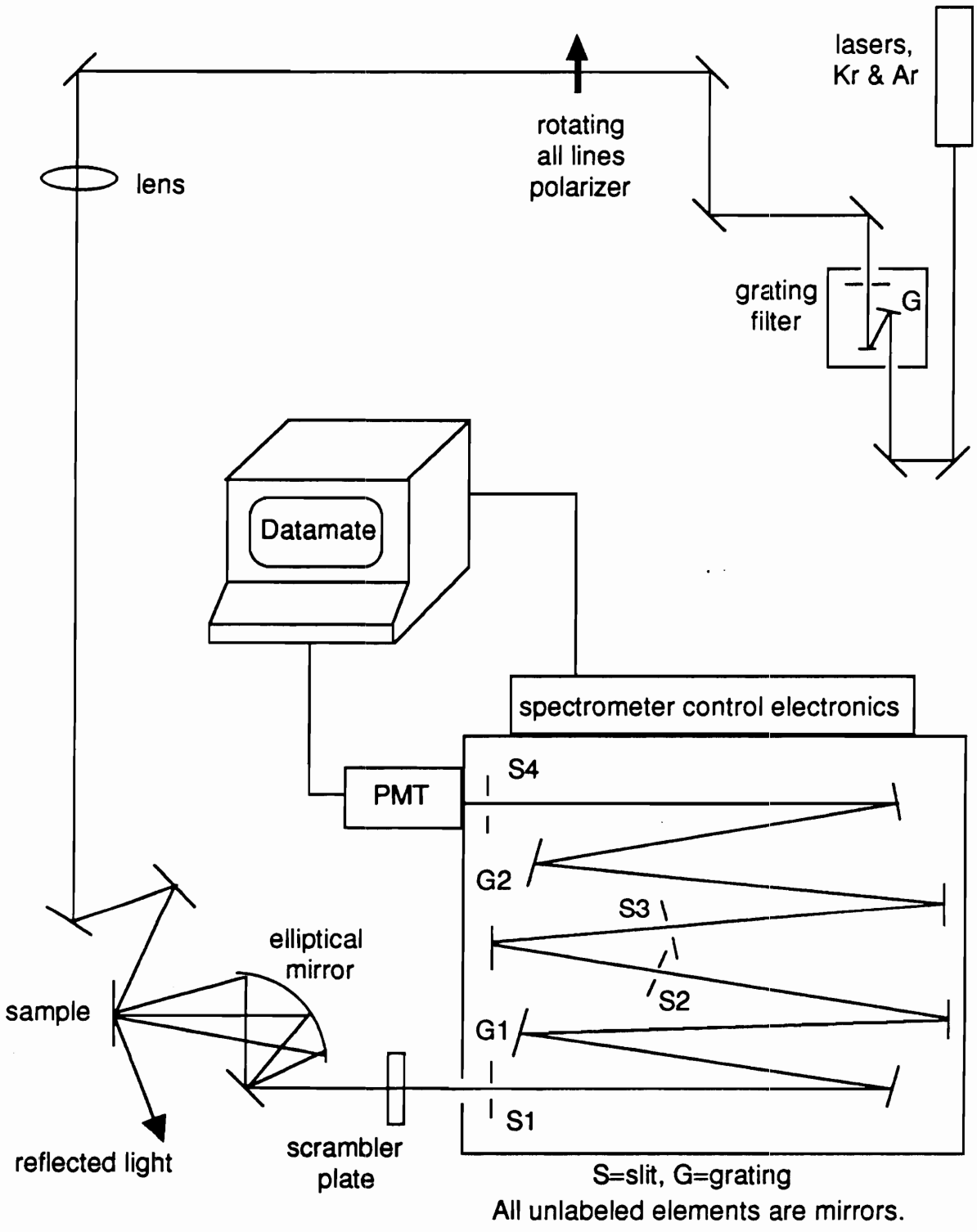

Fig. 2.3: Schematic diagram of the Raman scattering set-up.

compared to 1200 lines/mm for the 1404, and has a higher resolving power. Only the resonance Raman experiments were done on the 1404.

For these resonance studies, a Spectra-Physics model 375 B dye laser was used with stilbene three as the dye to provide excitation in the region of photon energies (2.85 - 2.94 eV) near the E_1, 2.89 eV, gap energy of c-GaAs. The dye laser pump source was an 18 watt Spectra-Physics model 2045 visible Ar^+ laser operating in all lines violet mode at a power of about 5.5 watts. Power output from the dye laser (with fresh dye) ranged from 80 to 150 mW, with the peak in the power at 432 nm. Scattered light was detected with an Hamamatsu R928 PMT and data collection was automated with the DM 3000 software running on an eight MHz IBM compatible PC. The resolution was about 8 to 9 cm^{-1} for the range of wavelengths used.

The available laser lines for the non-resonant Raman experiments come from a Coherent Innova 90-K Kr^+ laser and a Coherent Innova 90-5 Ar^+ laser. The lines used in the experiments were the Ar^+ 4579, 4765, 4880, and 4965 Å lines and the Kr^+ 6471 Å lines. The resolution for the experiments in chapters four and five was about 4.5 cm^{-1}. In chapter six, the resolution was about 7.0 to 8.5 cm^{-1}. The power output from these lasers fluctuates by about three percent per hour after an initial warm-up time of an hour. In order to protect the data from being affected by any power instabilities, multiple scans were performed

with short integration times. For instance, if the Raman signal to noise ratio was quite small, one may need to sit at each frequency in the scan for 60 seconds to integrate out the noise. If there are 600 frequencies to scan over, one scan will take 10 hours, and the shape of the signal could be distorted by non-random power losses in the source. If the time scale of these power changes is on the order of an hour before distortions are introduced, then an integration time of one second will produce 60 undistorted but noisy scans after 10 hours. Averaging the scans will yield a cleaner spectrum.

Before the incident laser light hits the sample, it is passed through a tunable grating filter to remove the unwanted laser plasma lines which could otherwise cause spurious peaks in the Raman spectra. The filtered light is then passed through an all lines polarizer to allow for the setting of different polarizations for each experiment. Most of the experiments were performed with light polarized in the scattering plane (H-polarized) in a near-Brewster angle configuration in order to maximize the transmitted light and increase the Raman signal. Only the experiments in chapter five were not.

All experiments were done in a quasi-backscattering geometry, which has the advantage of diverting the reflected light away from the scattered light collection optics (see Figure 2.3) thus reducing stray light. Since GaAs has a high index of refraction for the frequencies of the incident light in these experiments, even a 45° angle of incidence will mean the transmitted light

is no more than 10° away from the surface normal. The selection rules for backscattering discussed in chapter one apply. There will be a slight change in the rules due to a component of the incident light polarized in a direction normal to the surface when the incident light is H-polarized. This accounts for the appearance of a weak TO component which is forbidden for the (100) plane of zincblende in a backscattering set-up. In experiments where it was crucial to avoid the TO peak, the incident light was polarized perpendicular to the scattering plane (V-polarized) and theoretically, only the intensity of the LO peak should have been slightly less than that predicted by the selection rules (whether it was actually less was not determined).

The problem of the intensity difference is eliminated by using the intensity of comparable Raman features of c-GaAs as a means of normalizing Raman spectra (e.g. when measuring the LO peak intensity of implanted GaAs, use the LO peak of c-GaAs; when measuring the implanted GaAs 2LO peak intensity, use the c-GaAs 2LO peak intensity as a norm). For samples which had both front and back sides polished to optical quality, simply flipping the sample to its back side provided an unimplanted and smooth c-GaAs surface at exactly the same focusing position as its implanted front side. For samples which had a dull back side, the sample holder was modified so that a sample's front surface (i.e. the surface closer to the entrance slit of the spectrometer) rather than its back would always be at the same position regardless of the thickness of the sample. The samples were

mounted on the back side of a plate with a hole cut in it, and were clamped at the back by a spring-action clamp which changed position to accommodate different sample thicknesses. Normalization was then performed by a simple kinematic replacement of the sample with a piece of c-GaAs. These procedures assume that both the implanted and c-GaAs sample surfaces have the same degree of roughness since roughness can reduce the reflectivity of the sample, and the Raman intensity is dependent on sample reflectivity. A big advantage of these procedures is that frequency dependent terms in the Raman scattering cross section are removed (e.g. ω^4 dependence). There is no need to correct the spectra for the bias of the spectrometer towards particular frequency ranges or for any frequency dependent system responses (e.g. the detector response and the bandpass). A comparison between spectra taken with greatly different incident laser wavelengths is justifiable, barring other considerations (e.g. optical penetration depth) which may or may not be important for the particular system studied.

The backscattering geometry has to be used since GaAs has a high absorption coefficient, α, for the range of laser lines used. The optical penetration depth, $1/(2\alpha)$, for the laser lines in these experiments are listed in Table 2.2. Figure 2.4 shows the optical penetration depth as a function of incident photon energy for both a-GaAs and c-GaAs, generated from a Lorentz harmonic oscillator analysis (see chapter three) of their reflectivity spectra. The laser line used in each experiment was chosen so

TABLE 2.2: Optical penetration depths of the laser lines used in the experiments for crystalline and amorphous GaAs.

Incident Photon Energy (eV)	Wavelength (Å)	Optical penetration Depth (Å) from Figure 2.4	
		c-GaAs	a-GaAs
1.92	6471	1275	242
2.41	5145	548	134
2.50	4965	455	122
2.54	4880	416	117
2.60	4765	360	111
2.71	4579	259	100
2.85	4350	130	88
2.87	4320	117	86
2.89	4290	104	85
2.9	4275	98	84
2.92	4246	94	83
2.93	4231	91	82
2.94	4217	89	82

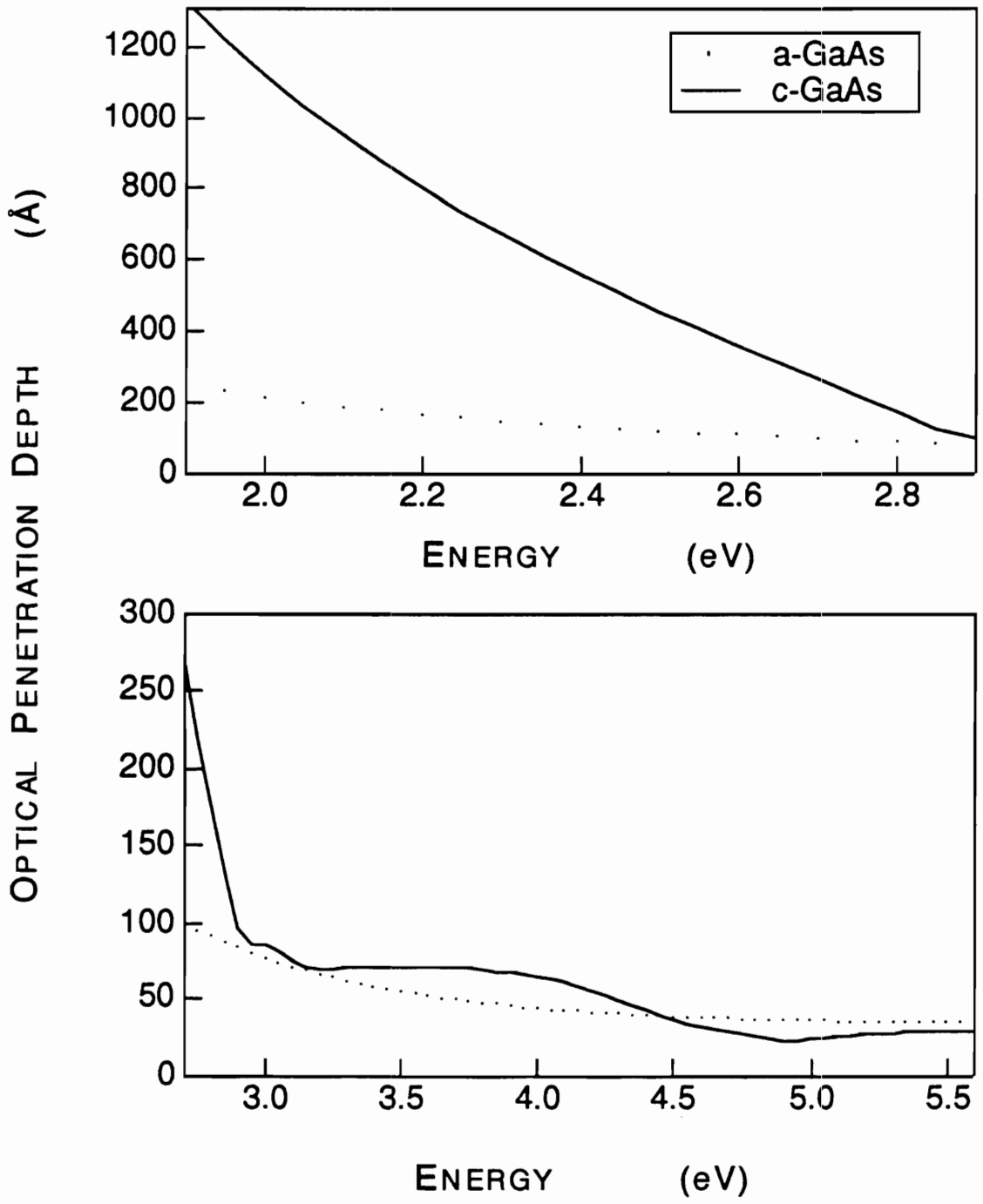

Fig. 2.4: Optical penetration depth of c-GaAs and a-GaAs as a function of incident photon energy. Top: 1.90 to 2.90 eV. Bottom: 2.70 to 5.60 eV. Solid curve is for c-GaAs while dots represent a-GaAs.

as to probe only those layers of the sample which were appropriate to the purpose of the experiment. For example, the depth profile experiments used 4579 Å light with a penetration depth of about 100 to 200 Å [Aspnes & Studna, Theeten & Erman] for a mixture of c-GaAs and a-GaAs since the etch step was only 200 Å.

For spectra which involved scanning in the region of vibrational and rotational frequencies (10 to 175 cm^{-1}) of the constituent molecules in air (mainly N_2 and O_2), the air at the sample surface was purged by a constant stream of argon gas. Otherwise, the spectral features of the air in the region of the focus of the incident light would appear due to the excitation from the laser beam [Holtz].

The light that scattered from the sample was then passed through an f/1.4 elliptical mirror. Movement of this mirror would focus the light down to a point centered at the entrance slit to the monochromator. Very good vertical positioning could be obtained by slight adjustments in the sample position and the coarse adjustment knob of the mirror. However, the horizontal positioning provided by the mirror can cause the spot size of the focused light to increase, resulting in a loss of Raman signal for small enough entrance slit widths. To remove this difficulty, the scrambler plate (a quarter wave plate through which the scattered light passes in order to remove the monochromator preference to particular polarizations by converting plane polarized light to circularly polarized light) was modified. It was placed

in a holder that would allow it to rotate about an axis parallel to the entrance slit. By rotating the plate, the scattered light can be positioned horizontally without changing its spot size. Accurate positioning can then be achieved by monitoring the focused light through the periscope attachment and maximizing the fraction of the focused light in the periscope's field of view.

In some of the experiments, the peak positions of the Raman features needed calibration. This was done by inserting two or three neutral density filters (depending on the power at the laser head) between the scrambler plate and the entrance slit. The monochromator slits were adjusted to obtain a sharp peak (full width half maximum < three cm^{-1}) and to decrease the Rayleigh signal to a level that can be handled by the photomultiplier tube (PMT). A scan was then performed in the frequency region of the incident laser frequency. The Rayleigh peak position was taken to be zero wavenumbers.

The resolution of the system depends mainly on the entrance and exit slits and the density of the gratings. For the 1403, Holtz generated an empirical relationship between the linear dispersion and the wavelength:

$$\Delta l/\Delta\bar{\nu} \approx 0.043\ \lambda - 140 \qquad (2.1)$$

where λ is in Å and $\Delta l/\Delta\bar{\nu}$ is in μ/cm^{-1}. The spectral bandpass, B, is related to this dispersion and the slit width, W, by

$$B = \frac{W}{\Delta l/\Delta\bar{\nu}}. \qquad (2.2)$$

Using these two equations, the bandpass can be found for any combination of slit width and incident laser wavelength.

For all experiments which gave measurements of the FWHM, a correction for the effect of the bandpass of the instrument was made with the following equation:

$$\Gamma^2 = \Gamma_0^2 + B^2 \qquad (2.3)$$

where Γ is the observed linewidth and Γ_0 is the natural linewidth. The relation is valid for small B, on the order of two to five cm^{-1}. This is the magnitude of B in all experiments where the linewidth was of interest.

Light that passes through all four slits of the SPEX 1403 is detected by an RCA C31034A-02 PMT. The PMT is kept at a temperature of about -20 °C with a water cooled thermo-electric cooler. In the summer months, the coolant water is warmer and the tube cannot be kept as cold as in the winter months. Consequently, lower dark count rates were obtained in the winter (about five cps compared to about 40 cps in the summer with a tube voltage of 1390 volts). The contacts at the base of the PMT were occasionally checked to ensure that no condensation formed and introduced conduction paths which would increase the dark count.

Noise in the recorded spectra can be smoothed out with a Savitsky-Golay smoothing algorithm that is supplied with the SPEX Datamate mini-computer spectrometer controller. However, when the expected lineshapes of the Raman spectra were known,

curve-fitting using the Levenberg-Marquardt routine was performed on the data to yield the peak characteristics; curve fitting is more reliable than smoothing when the lineshape is known.

The estimates of error for peak characteristics using the methods described here are, at best, about ±5% for the intensity, ±0.5 cm^{-1} for the peak position and ±0.5 cm^{-1} for the linewidth. These estimates were obtained by repeating experiments (about five times) and performing a simple error analysis.

2.3 Ultraviolet Reflectivity

A full description of the apparatus and the software used in these experiments can be found elsewhere [Feng]. A schematic diagram of the set-up is provided in Figure 2.5. This discussion will also center only on those aspects which affect data interpretation.

The light sources used provide a large range of incident photon energies. Helma cells model OP-100 deuterium lamps (D_2) provided the ultraviolet light (2.85 to 5.60 eV) while GE ribbon tungsten lamps were the sources in the visible region (1.60 to 3.25 eV). The overlap of photon energies between sources is important, since separate scans for each region must be taken. There is some slight mismatch between these scans in the overlap region, and a composite scan can be made by considering the average ratio between the reflectivities in the overlap region of the high energy scan to those in the low energy scan. The low energy reflectivities are then multiplied

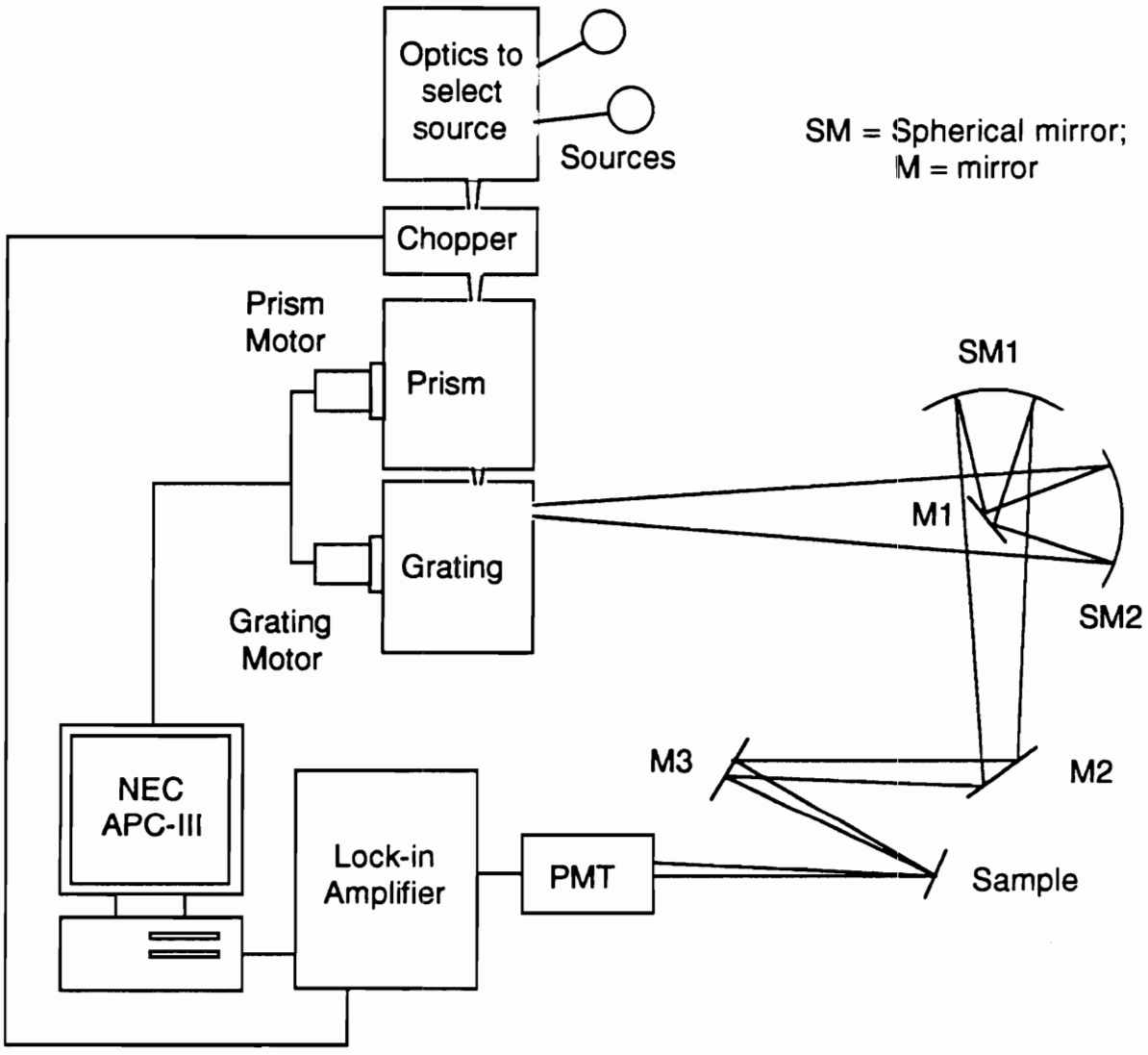

Fig. 2.5: Schematic diagram of the ultraviolet-visible reflectivity set-up.

by this ratio and the resulting low energy spectrum is joined to the high energy one. A greater number of overlapping data points will produce much better spectra. For instance, in chapter three, nine overlapping points were used and the ratio varied between 1.00 and 1.03. For all other reflectivity measurements, only one overlapping point was used.

The light sources have to be carefully monitored since their performance degrades over time. The stability of the sources was measured using a strip chart recorder attached to the EG&G model 5207 lock-in amplifier which took signals from the EMI 9558QA PMT. The spectrometer was held fixed at one photon energy (2.00 eV for tungsten, 4.65 eV for D_2) and the variation in the output as a function of time was recorded. New D_2 bulbs need a warm-up time of about an hour and will provide stable performance (less than two percent change per hour) for three hours before its output drops. Older bulbs provide a smaller period of stability (about two hours) but need the same warm-up time. Tungsten bulbs, on the other hand, require longer warm-up periods when new (about three hours) and are stable for an hour before a drop in the average output (noise fluctuations of one to two percent) of about two percent occurs. Older bulbs need only an hour to warm-up and are stable for an hour. If the stability of the source as a function of time is needed to correct spectra, measurements should be made in the same time period that the spectra are taken since these characteristics vary with the age of the bulbs.

Another factor in the stability of the output signal is the stability of the PTI model OC 4000 light chopper. The particular chopper in the lab is old, and a warm-up time of two days with the chopper set at its lowest frequency is needed before the chopper can stay at a fixed frequency. Since the response of the PMT is dependent on the chopping frequency, instability in the chopper is reflected as an instability in the PMT output. To improve the stability, several different frequencies were tested, and it was found that a setting of 39 Hz produced the most stable output and the best signal to noise ratio. The chopper frequency would increase to only 40 Hz after one day (provided that the two day warm-up time is observed).

To produce a spectrum, three measurements are needed: a background reading, a source intensity scan and the actual sample measurement. The background levels consist of contributions to the measured source and sample readings from the sample holder and any stray light in the system; they are, on the average, less than two percent of the source and sample intensities and rarely exceed five percent over the incident photon energy range of 1.60 to 5.60 eV. The source intensities are needed to account for the frequency dependence of the source output. A sample with a known reflectivity is used to measure the source intensity; aluminum (Al) and c-GaAs were used. Some problems were encountered with the Al mirrors, since each individual sample has to be calibrated, and as they age, their reflectivity decreases especially in the ultraviolet region. Corrections

to the spectra collected with the old Al mirrors were made by recalibrating the Al mirror reflectivity with c-GaAs as the reflectivity standard. The spectra that needed correction were multiplied by the ratio between the recalibrated reflectivity and the old mirror reflectivity. With the background, source, and sample intensities labelled as I_b, I_m, and I_s, and the source reflectivity as R_m, the reflectivity of the sample, R_s, is

$$R_s = \frac{I_s - I_b}{I_m - I_b} R_m . \qquad (2.4)$$

The spectra obtained in this way are automatically corrected for the presence of an oxide layer on the GaAs surfaces. For the known reflectivity of GaAs, the reflectivity of oxide-free GaAs is used even though the c-GaAs sample has a native oxide layer about 30 Å thick. Since the measured GaAs samples will have an identical oxide layer, the reduction in reflectivity due to this layer is factored out; the oxide layer is "optically" removed. Although the correction is an approximate one, it is quite convenient. The oxide layer has a much greater effect in the high energy region (where the E_2 peak is located) and is expected to produce negligible effects on the low energy region (E_1, $E_1+\Delta_1$ peaks). The reproducibility of the measurements in chapter three is within 3 to 4 % in the ultraviolet region and within 1 to 2 % in the visible.

Given the constraints of the system - the number and length of scans needed as well as the stability of the sources

- experiments must be done with great care. Each low energy scan from 1.60 to 3.25 eV takes approximately 13 minutes, while the high energy scans from 2.85 to 5.60 eV take about 18 minutes. Since at least three scans are needed to generate a spectrum, the high energy scans have only an allowance of six minutes every hour, while the low energy scans have an extra 21 minutes. Since there is at least a two hour period of stability for the high energy scans, two spectra can be obtained and averaged to reduce noise. For the low energy scans, however, only an hour is allotted. The best that can be done is to make one scan each for the background and the source and two scans for the sample. The low energy spectrum obtained in this way is noisier than the high energy spectrum.

To deal with these problems, scans can be made on separate days and averaged to reduce noise. Also, the signal to noise ratio must be maximized by optimizing the focusing conditions and increasing the range of the PMT output. This is done by finding the incident photon energy at which the sample intensity is at a maximum (two eV for tungsten, 4.65 eV for D_2). With the spectrometer sitting at this point, the focusing is fine tuned to increase the lock-in amplifier readings. Then the voltage on the PMT is increased until the amplifier reading is close to the maximum voltage that the amplifier can handle (i.e., without going over five volts; three volts was typically used).

The spectrometer has a Perkin-Elmer model 160 prism stage and a Perkin-Elmer model 16U grating stage. The slit

widths for both stages were set such that the resolution is no larger than .01 eV. The Compumotor CX57-83 stepping motors moved the prism and the grating and were controlled by a NEC-APC III computer via RS-232C. The interval between data points in each scan was 0.05 eV, and this was enough to resolve the doublet feature at three eV in c-GaAs. Finally, the data from the lock-in amplifier was also collected via RS-232C by the computer.

The estimates of error in these experiments were also accomplished by taking several (about 20) readings and performing a simple error analysis. Errors tend to be larger in the higher energy photon range, and are quite dependent on the uniformity of optical quality over the sample surface. Experiments that are done by measuring the same area of the sample yield at most five percent and on the average two percent error in reflectivity, while non-uniform surfaces can cause a 25% error near 5.60 eV. Great care was taken to measure the same area of the sample surface (choosing the area which yielded the highest PMT readings), and when necessary the amount of exposed material was reduced by reducing the size of the hole in the sample holder.

Increased accuracy is also achieved by increasing the number of overlapping points between the high and low energy scans. Previous versions of the spectrometer operation software (SPEC5) allowed only one overlapping point at 3.2 eV. A modified version, SPEC6, allows the high energy scan to go down to 2.85 eV, while the low energy scan can go up to 3.25 eV.

With an energy interval of .05 eV, nine overlapping points are obtained.

Rather than smoothing the spectra obtained to reduce noise, curve fitting methods are employed (see chapter three).

CHAPTER THREE
THE USE OF INTERBAND REFLECTIVITY FOR DEPTH-PROFILING THE DAMAGE LAYER IN ION-IMPLANTED GaAs

3.1 Introduction

In order to have better control over device manufacturing processes, it is important to characterize the damage produced by ion implantation. Several optical methods have been employed, such as Raman scattering [Holtz et al., 1988], photoreflectance, electroreflectance [Bottka et al.], spectroscopic ellipsometry [Erman et al., Aspnes et al., Erman and Theeten] and ultraviolet reflectivity [Feng and Zallen, Borghesi et al.].

Data collected with techniques that deal with the dielectric function (e.g. reflectivity) have traditionally been analyzed using the Kramers-Kronig equations. The drawbacks of using Kramers-Kronig analysis are mainly due to the lack of data since non-physical effects arise unless Kramers-Kronig analysis is performed over a wide enough energy range to include all relevant excitations in the spectrum. Improvements of Kramers-Kronig analysis are mainly based on extending the data to a wider range. Jezierski tested his improved Kramers-Kronig analysis algorithm on a synthesized reflectivity spectrum made up of three classical oscillators.

Instead of just using the classical oscillators to test Kramers-Kronig analysis algorithms for limited data sets, one can curve

fit reflectivity data to a sum of oscillators [Feng and Zallen, Verleur, Spitzer and Kleinman]. Spitzer and Kleinman analyzed the infrared lattice bands of quartz by using a sum of lattice oscillators to represent the complex dielectric function. Verleur extended the idea to other frequency regions and applied it to the study of the reflectivity of bulk silicon. Erman et al., applied an oscillator analysis to determine the optical properties of ion-implanted GaAs. They used the effective medium approximation [Bruggeman; Aspnes, 1982] and assumed that the volume fraction which was crystalline had the same dielectric function as the bulk material; they showed that a description of the implanted material as a mixture of amorphous (a-) and crystalline (c-) GaAs was inadequate for reproducing the observed optical properties. Feng and Zallen also analyzed ion-implanted GaAs but they reversed the Bruggeman effective medium approximation to determine ε_μ, the dielectric function of the microcrystalline portion in terms of ε, the dielectric function of the implanted material and ε_a, the dielectric function of a-GaAs. They showed that ε_μ depended on the microcrystal size. Borghesi et al. did not make use of an effective medium approximation due to the microcrystal size effect but employed the oscillator analysis in order to make a phenomenological study of Ge-implanted Si.

In this study, the Be-implanted samples will be modeled as a mixture of amorphous GaAs (a-GaAs) and microcrystalline GaAs (μ-GaAs). Damage depth profiles will be in terms of the oscillator parameters of μ-GaAs. The profiles generated from

individual linewidth parameters for the interband peaks are compared to the depth profile generated from the sum of these. It will be shown that more information can be gathered from the procedure involving the sum and that this procedure yields profiles which are in reasonable agreement with previously measured Raman scattering damage depth profiles. A connection between the Raman data and the reflectivity data will also be established in terms of the Lyddane-Sachs-Teller relation, reinforcing the validity of the oscillator analysis.

3.2 Oscillator Analysis

3.2.1 General Method

Figure 3.1 is a flow chart that summarizes the procedure used in the analysis. The difference between the experimentally measured reflectivity data and the reflectivity values calculated from the oscillator-analysis dielectric function are minimized by a modified Levenberg-Marquardt algorithm [Math/PC-Library, IMSL]. The dielectric function is constructed as a sum of seven Lorentzians [Erman et al., Feng and Zallen, Verleur, Spitzer and Kleinman]:

$$\varepsilon(\omega) = \varepsilon_{\infty} + \sum_{i=1}^{7} \frac{F_i^2}{\omega_i^2 - \omega^2 - i\,\Gamma_i\,\omega} \qquad (3.1)$$

where $\varepsilon(\omega)$ is the dielectric function at frequency ω, ε_{∞} is the dielectric function at infinity (high frequency asymptote) and F_i, ω_i, and Γ_i are the ith oscillator strength, position, and linewidth

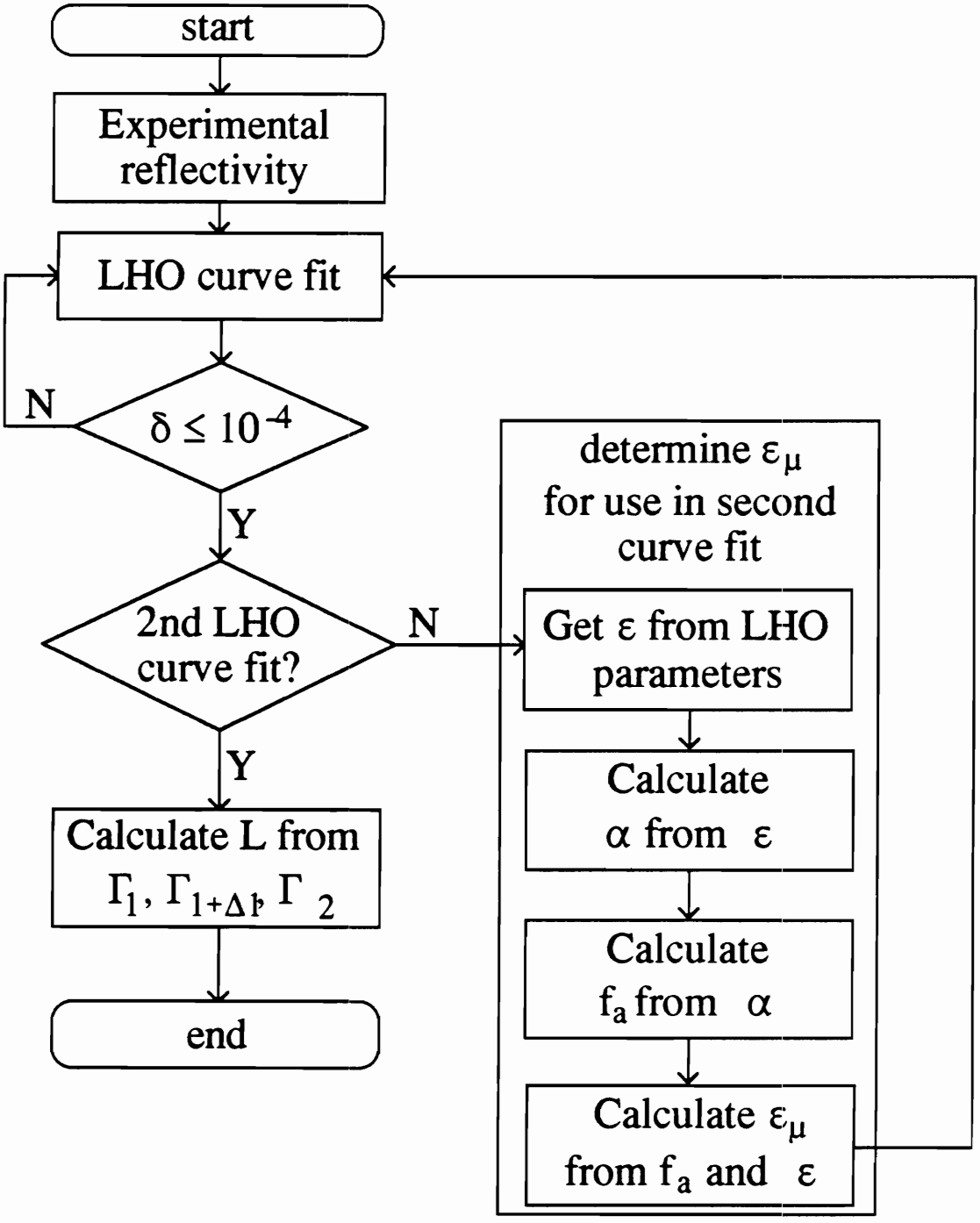

Fig. 3.1: Flowchart for the oscillator analysis used to get the microcrystal sizes and the amorphous volume fractions. Note that the first curve fit is a fit to the reflectivity, while the second curve fit is a fit to the microcrystalline dielectric function.

respectively. Seven oscillators were needed in this study to adequately model the spectrum as has been found also by previous workers studying GaAs [Erman et al., Feng and Zallen]. A calculated reflectivity spectrum was generated from the real and imaginary parts of the dielectric function. The set of 22 parameters is varied on each iteration of the curve fitting procedure in order to minimize the quantity

$$\delta = \left[\sum_{i=1}^{N} |\,\mathrm{fit}(\omega_i) - \mathrm{data}(\omega_i)\,|^2 \right] \Big/ \left[\sum_{i=1}^{N} |\,\mathrm{data}(\omega_i)\,|^2 \right] \qquad (3.2)$$

where N is the number of data points, fit is the value calculated by the curve fit, and data are the experimentally measured values. (Tests were previously carried out by Feng & Zallen to show that the curve fitting procedure is satisfactory.) In all of the fits to the measured reflectivity, $\delta < 10^{-4}$.

From the oscillator parameters, the dielectric functions of the samples are known. With the dielectric function, the absorption coefficient can be calculated:

$$\alpha = (4\pi/\lambda)\{[(\varepsilon_1^2 + \varepsilon_2^2)^{1/2} - \varepsilon_1]/2\}^{1/2} \qquad (3.3)$$

where α is the absorption coefficient, λ is the wavelength of the incident light, and ε_1 and ε_2 are the real and imaginary parts of the dielectric function respectively. Using α, one can estimate the amorphous volume fraction, f_a, of the sample [Holtz et al., 1988; Feng and Zallen]:

$$\alpha = f_a\alpha_a + (1 - f_a)\alpha_c \qquad (3.4)$$

where α_a and α_c are the absorption coefficients of a-GaAs and c-GaAs, respectively. α_a [Aspnes, private communication] and α_c [Aspnes and Studna] were determined in the same manner as α from their respective reflectivity spectra. f_a was extracted by curve fitting α to equation 3.4 in the energy region between 2.0 and 2.4 eV. It was shown that in this low-energy region the absorption coefficient, α_μ, of μ-GaAs is well approximated by α_c even for the most heavily damaged sample [Feng and Zallen]. For higher-energy regions near the interband critical points in the electronic joint density of states, the approximation breaks down because α_μ becomes significantly different from α_c [Feng and Zallen].

With f_a known, the effective medium approximation can be reversed to find ε_μ, the dielectric function of the microcrystalline component, in terms of ε_a, the known dielectric function of a-GaAs, and ε, the dielectric function of the sample [Feng and Zallen]:

$$\varepsilon_\mu = \varepsilon(1 + 2B)/(1 - B) \qquad (3.5)$$

where $B = f_a(\varepsilon-\varepsilon_a) / [(2\varepsilon + \varepsilon_a)(1-f_a)]$. The μ-GaAs dielectric function is then fitted with seven oscillators and the parameters are used to characterize the sample.

An uncertainty-principle argument is employed to extract the microcrystal size from the linewidths of the E_1, $E_1+\Delta_1$, and

E_2 peaks [Feng and Zallen]. The linewidths, $\Gamma_\mu(E_i)$, of these oscillators are expressed as a sum of the linewidth for the oscillator in c-GaAs, $\Gamma_c(E_i)$, and a width due to the finite size effects:

$$\Gamma_\mu(E_i) = \Gamma_c(E_i) + A(E_i)L^{-1} \tag{3.6}$$

where A is a constant that depends on the interband peak. It was shown that the size effect broadening is proportional to the reciprocal of L, the mean diameter of the microcrystals. A smaller microcrystal implies a shorter excited state lifetime since an electron or hole will not have to travel as far before "colliding" with the microcrystal boundary. Using the uncertainty principle, a shorter lifetime means a greater spread in energy; hence the linewidth of the oscillator becomes broader.

The values of $A(E_1)$ and $A(E_2)$ were taken from Feng and Zallen. Table 3.1 shows the values of A corresponding to the interband critical points E_1, $E_1+\Delta_1$, and E_2. It also includes the values $4\pi|dE/dk|_{max}$, the energy band dispersion, which is equated to A by an alternative uncertainty principle argument; a decrease in L means an increase in the momentum spread for each state, and an energy spread occurs as a result of the energy band dispersion. The value estimated for $A(E_1+\Delta_1)$, 15 ev·Å, is much closer to its associated dispersion than the value found by Feng and Zallen. The low value they obtained was inconsistent with the GaAs band structure and was not understood.

Table 3.1: Slopes, A_i , of the linear relations between the linewidth parameters and the inverse microcrystallite size. Values for $4\pi|dE/dk|_{max}$ were estimated by Feng and Zallen.

Critical Point	A Feng and Zallen ev·Å	A this study ev·Å	$4\pi \|dE/dk\|_{max}$ ev·Å
E_1	18	18	16
$E_1+\Delta_1$	9	15	16
E_2	21	21	34

3.2.2 Limitations and Solutions

This oscillator analysis is not without its difficulties. The algorithm used in the curve fit is not constrained to produce only physically meaningful parameters (e.g. one can obtain negative values for linewidths). Since the final parameters are very sensitive to the choice of the initial parameters, a wrong choice can yield non-physical results. Another difficulty caused by this sensitivity to the initial guess is that several sets of parameters can be obtained which represent a convergence in the curve fitting routine. Figure 3.2 shows a surface which represents an error function (like δ in equation 3.2) in a two dimensional parameter space. The curve fitting algorithm converges when it finds a valley on the surface. If the initial parameter set places the value of the error function at point A, the curve fitting routine will most likely produce the parameters corresponding to point B. However, point C is also a valley with a value lower than point B. The parameter set at point C may be more meaningful and consistent with physical observations. As the number of parameters increases, the more crucial the initial guess becomes since the number of local minima in the error function is likely to increase.

Another complication occurs when a value δ_t for δ is specified as a terminating condition for the curve fit. The number of points in the error function which satisfy this condition increases even more rapidly than the number of local minima as the number of parameters increase. Imagine a plane intersecting a

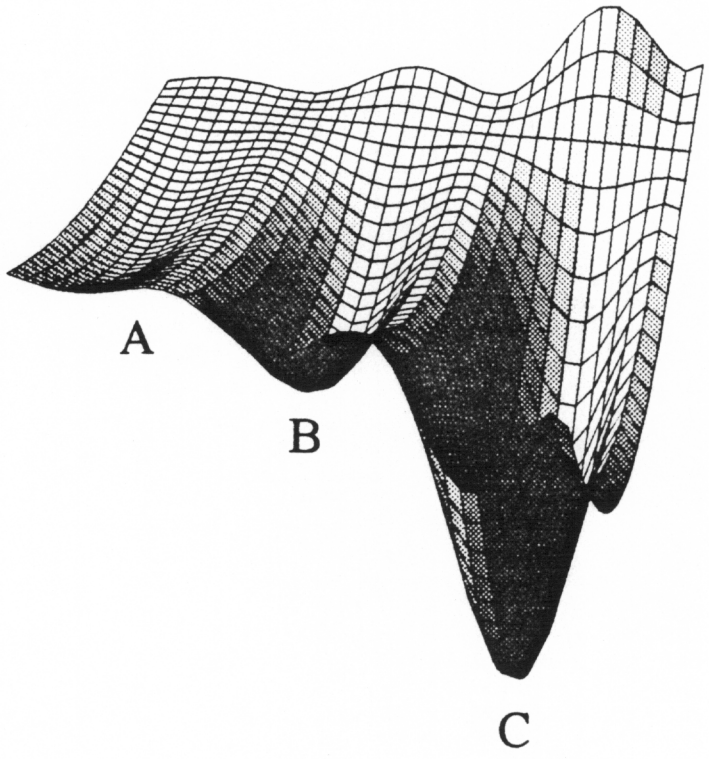

Fig. 3.2: A surface in two-parameter space representing a hypothetical error function. Points labelled A, B, and C are referred to in the text.

valley at a height δ_t and parallel to the plane defined by the parameter-coordinate axes; all the points in that intersection satisfy the terminating condition, and which one is chosen depends on the point on the rim of the valley which serves as an initial guess. In this case, the initial guess for the parameters becomes even more crucial. However, by providing lower values of δ_t one decreases the differences between the possible sets of final parameters.

In order to overcome these difficulties, an additional level of fluctuation-damping was introduced in the following way. Reflectivity spectra were grouped according to similar characteristics. These groups are shown in figures 3.3, 3.4, and 3.5. The high-damage cluster represents the most damaged samples, and their reflectivity spectra are similar. This group consists of samples etched up to 2 minutes. The samples etched for 3 and 4 minutes form the transition cluster; their reflectivity spectra are midway between that of the high-damage cluster and that of c-GaAs. They represent a gradual return to crystallinity and a drop-off in damage. The last 2 samples, etched for 5 and 6 minutes, form the low-damage cluster; they have reflectivity spectra which are almost like that of c-GaAs. The reflectivity spectrum for c-GaAs is included in figures 3.3, 3.4, and 3.5 for comparison.

Each cluster was assigned its own set of initial parameters. The initial parameters used for the high-damage cluster were taken to be the output parameters generated by fitting the

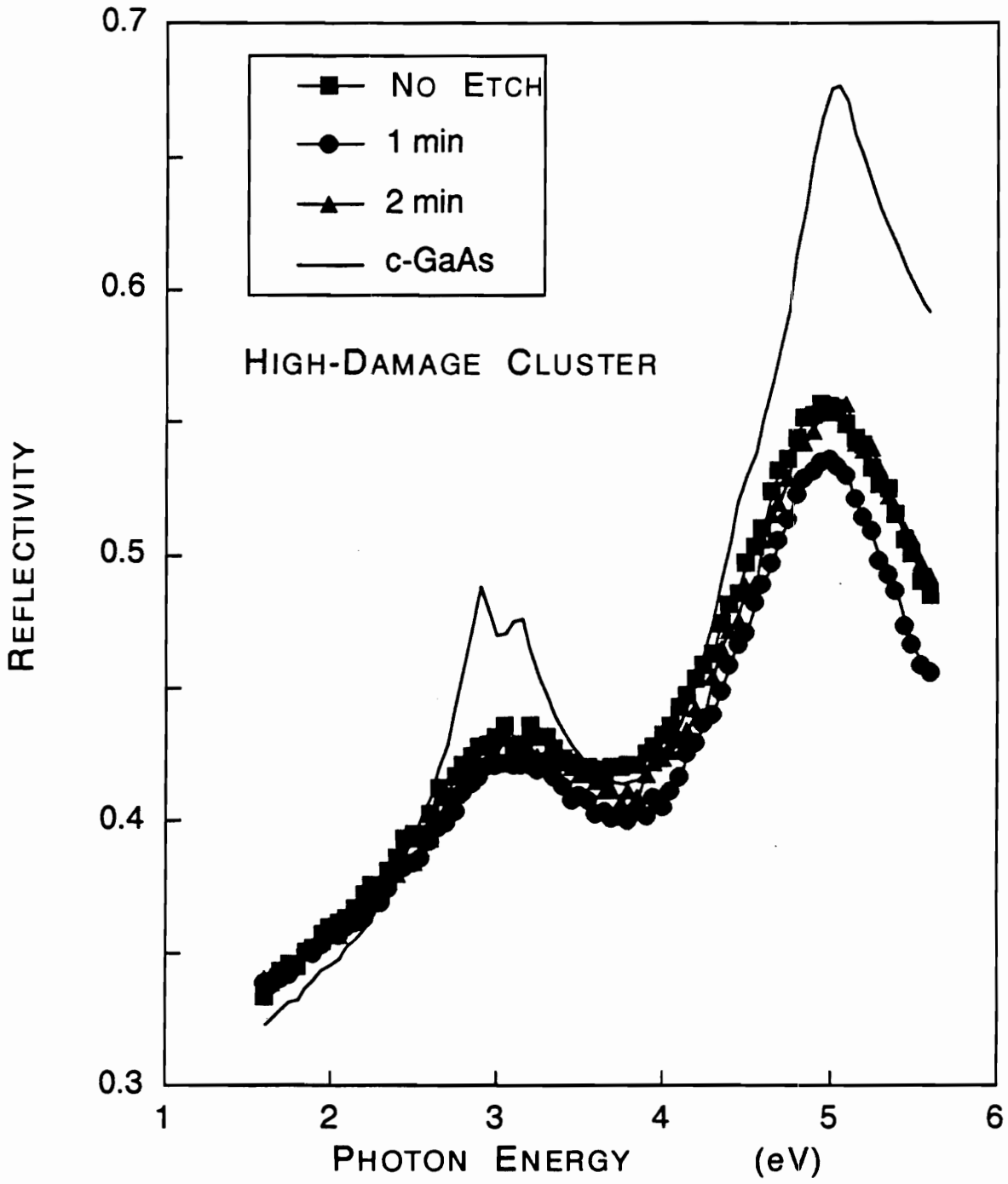

Fig. 3.3: Reflectivity spectra for the high-damage cluster. Squares represent data for the unetched sample, circles show the data for the one-minute etched sample, and triangles represent data for the two-minute etched sample. The c-GaAs reflectivity spectrum is shown for comparison.

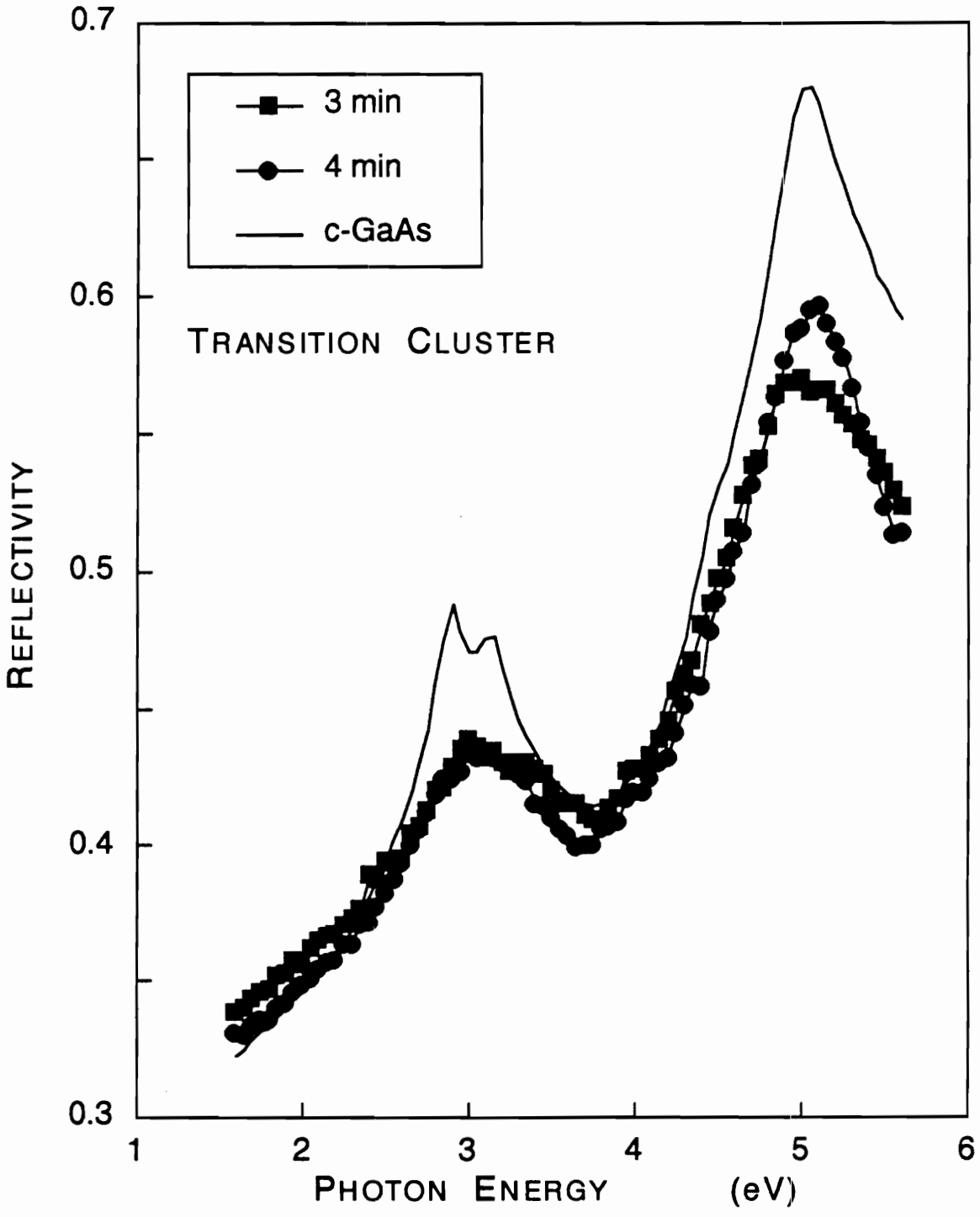

Fig. 3.4: Reflectivity spectra for the transition cluster. Squares and circles are data points for the three and four minute etched samples, respectively. The c-GaAs reflectivity spectrum is shown for comparison.

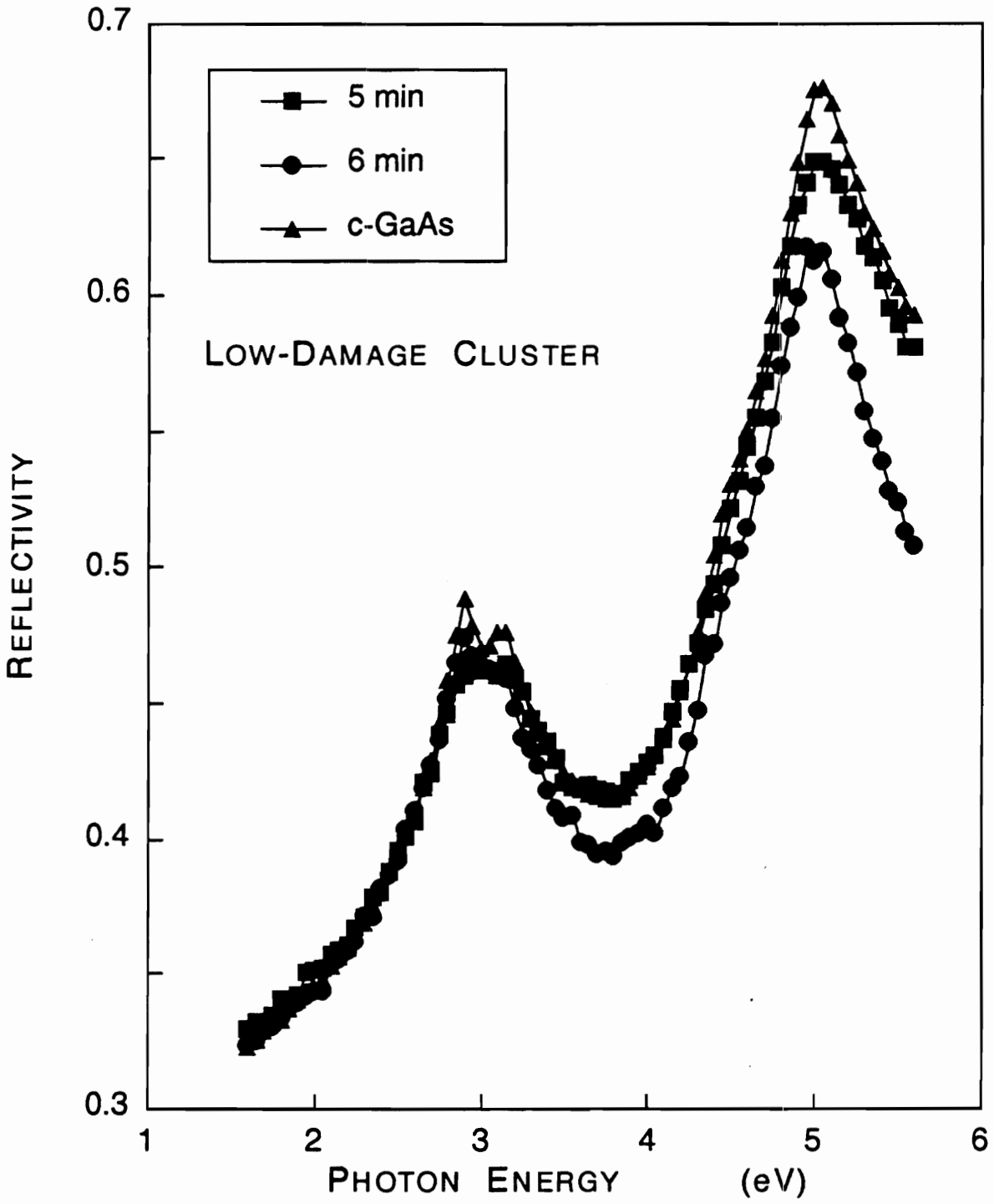

Fig. 3.5: Reflectivity spectra for the low-damage cluster. Data for the five and six minute etched samples are drawn as squares and circles respectively. Triangles represent c-GaAs reflectivity data.

reflectivity of the unetched (as-implanted) sample, using the crystal parameters as the starting point for generating this fit. Similarly the transition cluster used parameters which were the final output of a curve fit to the 3 minute etched sample with crystal parameters as a first guess. The low-damage cluster used the crystal parameters directly as its initial parameter set. The crystal parameters resulted from two successive curve fits: a fit to the c-GaAs reflectivity spectrum (using as an initial guess the c-GaAs parameters determined by Feng & Zallen) while holding ε_∞ fixed, and a fit to the real and imaginary parts of the c-GaAs dielectric function (generated from the parameters of the first fit) with ε_∞ allowed to vary. (The curve fit for the dielectric function is better behaved than that for the reflectivity.) The fits are more reasonable when their starting points are a close match to the actual data.

Another aspect of the procedure deals with ε_∞. This parameter was not allowed to vary in the reflectivity fits, since the fits were more consistent when this particular parameter was fixed. Also, with fewer parameters the difficulties previously described are partially relaxed. An estimate for ε_∞ was determined from the qualitative behavior of the reflectivity spectra and from the value determined by Feng & Zallen for their most damaged sample. The high-damage cluster used their value of 2.38; ε_∞ was varied linearly from 2.38 to 1.55 (Feng & Zallen's value for c-GaAs) between the 2 minute and 6 minute etched samples which represented a gradual return to crystallinity. This choice

of behavior for ε_∞ is a self-consistent one, as will be seen by the values which result when allowing it to vary in the dielectric function fits; it is also consistent with Raman peak shifts (obtained by Holtz et al., 1988) and the Lyddane-Sachs-Teller relation as will be seen in the next section.

Once the composition (f_a, f_μ) and the dielectric function of the mixture was determined, the μ-GaAs dielectric functions were extracted. The fitting procedure for these functions was better behaved and straightforward, since there were effectively twice as many data points to fit (the fit was a simultaneous fit to both the real and imaginary parts). The c-GaAs parameters were used as the initial guess (except for the ε_∞'s which were the same as the values used in the reflectivity fits) for all samples and all parameters were allowed to vary. The error function was weighted by a factor of two around the interband peaks in order to tighten the fits in these regions. In all dielectric function fits, $\delta \leq 10^{-4}$.

Another limitation in this analysis is that although an oscillator is needed with an energy (peak position parameter) beyond the range of the actual data to provide high frequency contributions to the data in the range, portions of the fitting functions that lie outside the data range cannot be taken too seriously. When using all the parameters for analysis, one must be aware that such an oscillator can cause problems.

Finally, it must be noted that since the amorphous volume fraction is determined using the absorption coefficient values in

the range 2.0 to 2.4 eV, it represents an average value over a depth of about 600 Å. The optical penetration depth for c-GaAs is about 800 Å at 2.2 eV [Aspnes and Studna]; the corresponding value for a-GaAs is about 200 Å [Theeten and Erman]. The optical penetration depth for the mixed material lies somewhere in between. However, the rest of the analysis carried out using the parameters around E_1, $E_1+\Delta_1$, and E_2 are averages over only 100 Å since the optical penetration depth in these regions is less than 100 Å.

3.3 Damage Depth Profiles

Figure 3.6 shows the linewidth parameters $\Gamma(E_1)$, $\Gamma(E_1+\Delta_1)$, and $\Gamma(E_2)$ as a function of etch depth. The microcrystalline parameters produce damage depth profiles that are in good qualitative agreement with the Raman profiles. However, since making use of only one parameter to do a damage profile means extracting information from a small region of energy, these damage profiles are not as good as that of Figure 3.7, made by considering information averaged over all three interband oscillators, and that of Figure 3.8, which makes use of the full dielectric function in its derivation.

To produce Figure 3.7, the value of A in equation 3.6 is assumed to be the same for all three interband oscillators. A larger value for $A(E_1+\Delta_1)$ (15 eV·Å) than that found by Feng and Zallen (9 ev·Å) is needed in order to make the microcrystal sizes deduced from $\Delta\Gamma(E_1+\Delta_1) \equiv \Gamma_\mu(E_1+\Delta_1) - \Gamma_c(E_1+\Delta_1)$, consistent

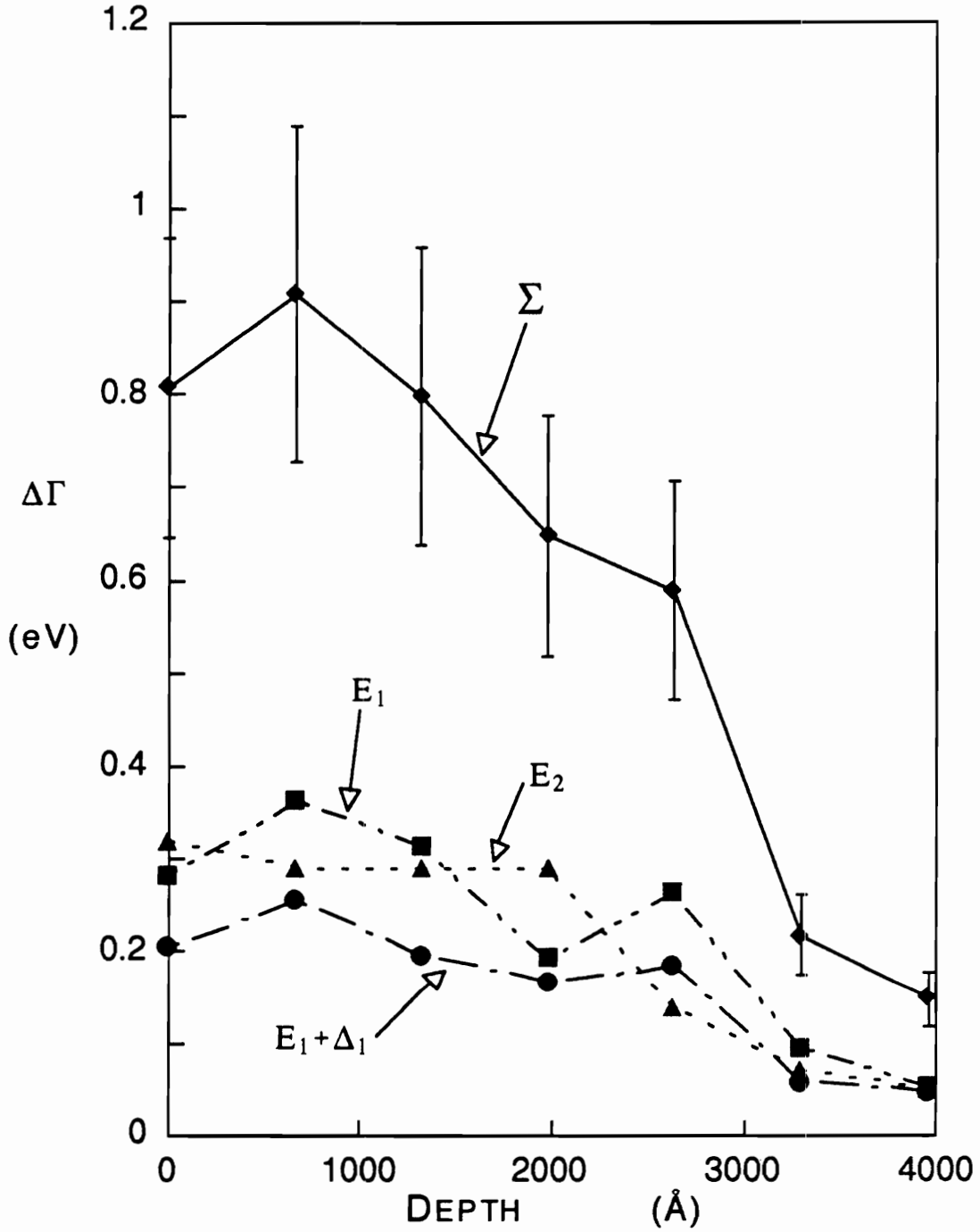

Fig. 3.6: Linewidth broadening of the interband peaks vs. etch depth. The curve marked Σ is the sum of the other three curves. The c-GaAs values for the linewidths of the interband peaks are 0.20, 0.34, and 0.34 for $\Gamma(E_1)$, $\Gamma(E_1+\Delta_1)$, and $\Gamma(E_2)$, respectively. Error bars represent deviations of the three $\Delta\Gamma$ curves from $\Sigma/3$.

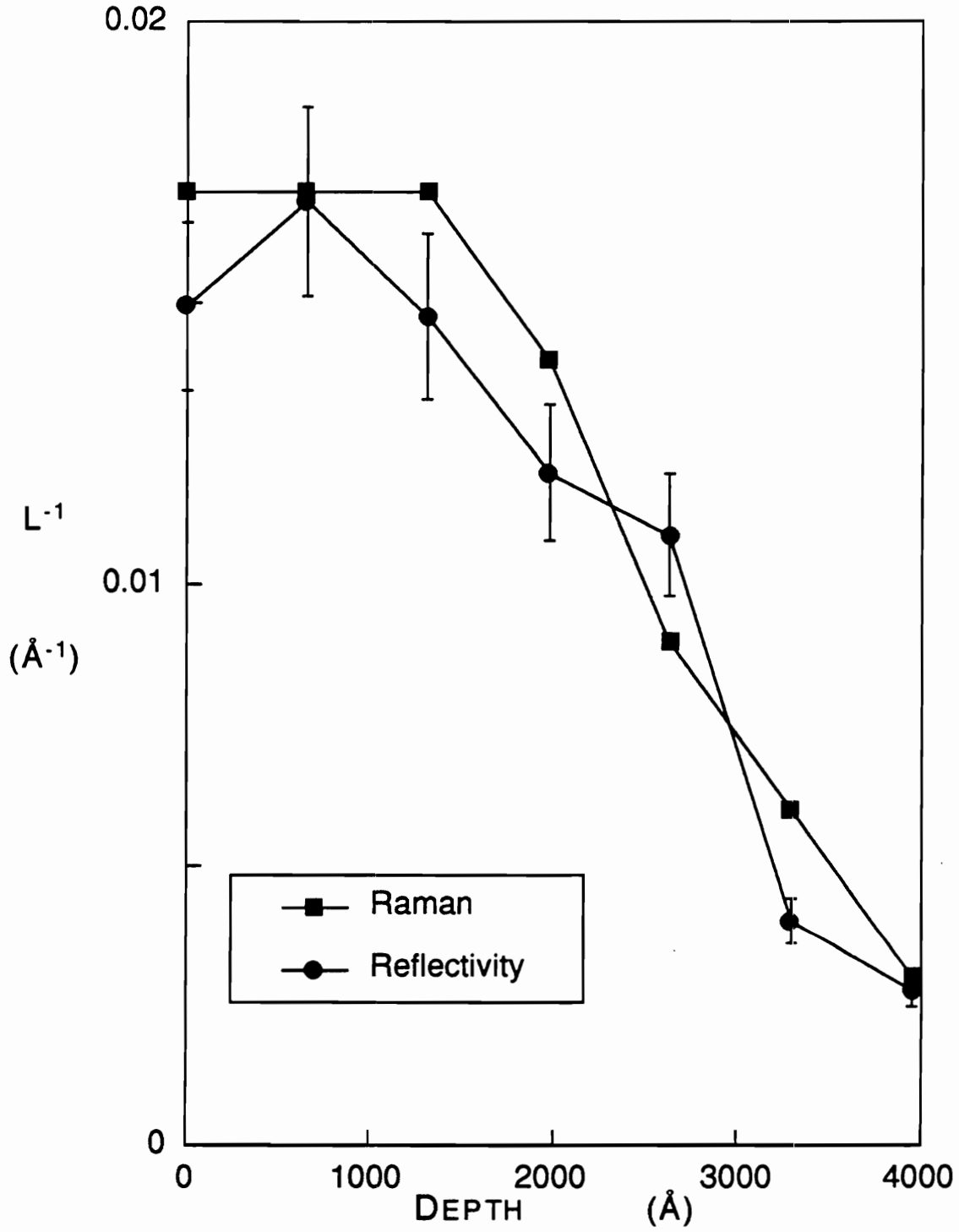

Fig. 3.7: Inverse microcrystal size vs. etch depth. Raman data, are shown as squares [Holtz et al., 1988]. Circles represent data derived from the oscillator analysis of reflectivity spectra. Error bars are estimated from plateau region fluctuations.

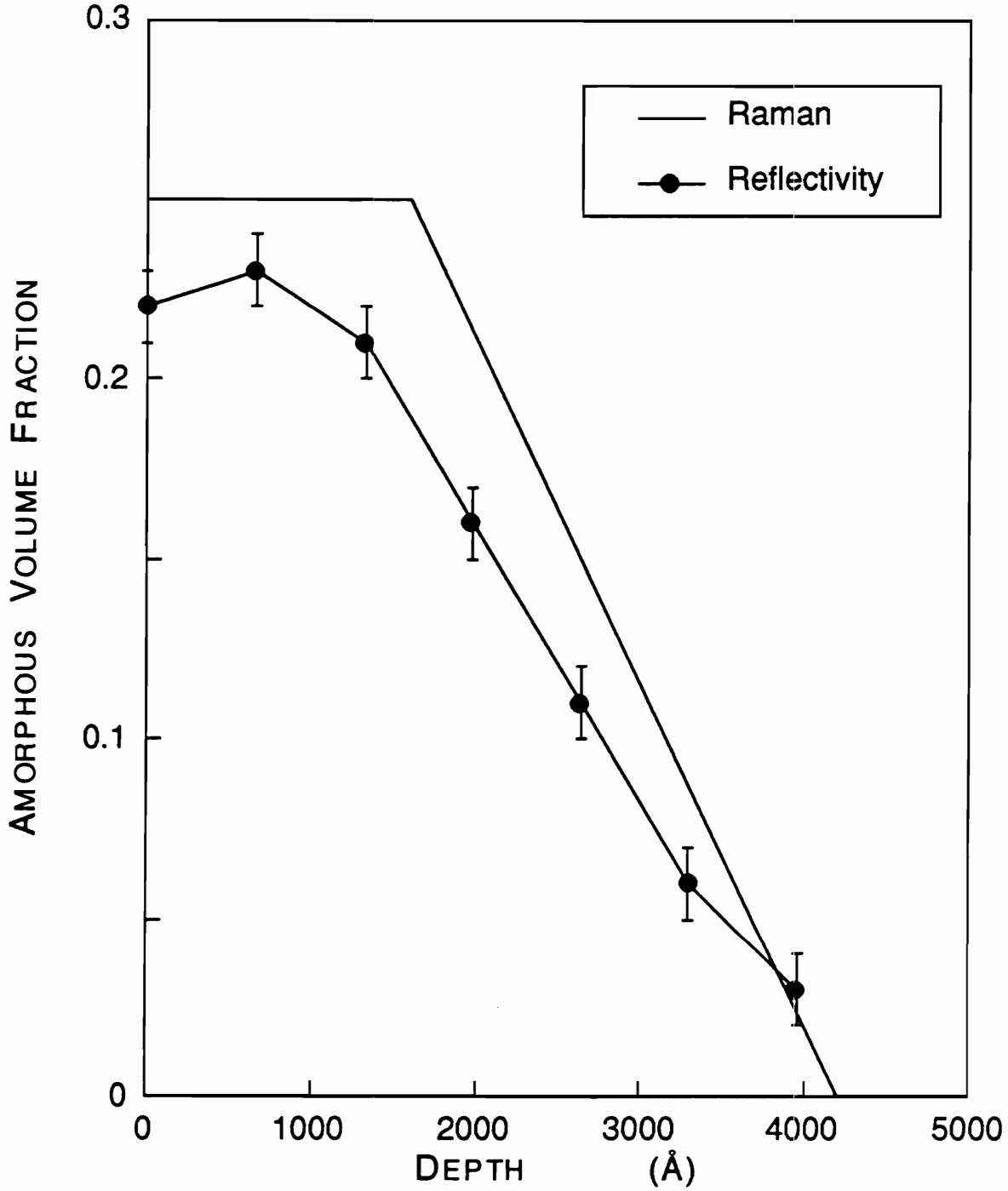

Fig. 3.8: Amorphous volume fraction vs. etch depth. The lines without points represent Raman data [Holtz et al., 1988]. Circles show data obtained from an oscillator analysis of the reflectivity spectra. Error bars are estimated from fluctuations in the plateau region.

with those deduced from $\Delta\Gamma(E_1)$ and $\Delta\Gamma(E_2)$. Since $A(E_1)$ and $A(E_2)$ are 18 and 21 eV·Å, and $A(E_1+\Delta_1)$ is not too different from these, we take the value of A to be the average of all three values, 18 ev·Å. The length measure of the characteristic microcrystal size, L, can then be determined from:

$$L^{-1} = (3A)^{-1} \sum_i \Delta\Gamma(E_i) \qquad (3.7)$$

where the sum is over all three interband broadenings. By using this sum, the fluctuations in the individual linewidth parameters are averaged over, improving the "signal-to-noise ratio." The variation with etch depth of the sum in the right hand side of equation 3.7 is plotted in Figure 3.6 as the curve labelled Σ.

Figure 3.7 shows the inverse microcrystal size as a function of etch depth for both reflectivity data (determined from Figure 3.6 and equation 3.7) and Raman data [Holtz et al., 1988]. Figure 3.8 shows the amorphous volume fractions as a function of the etch depth derived from the oscillator analysis (eq. 3.4) compared with those derived from the Raman data of Holtz et al., 1988.

Both figures 3.7 and 3.8 show that this analysis yields results in agreement with the Raman data of Holtz et al., 1988. A plateau region is observed up to a depth of about 1500 Å. Between 1500 and 4000 Å the amount of damage drops off linearly from the maximum damage to no damage at all, indicating that the total damage layer depth is 4000 Å.

Figure 3.9 shows ε_∞ vs etch depth. This parameter shows the same qualitative damage depth profile as the ones obtained using the amorphous volume fraction and the inverse microcrystal size. ε_∞ gives the same plateau depth (1500 Å) as the Raman data. This damage depth profile is consistent with the choice made for the initial values of this parameter in the curve fitting routine.

3.4 The Static Dielectric Constant: Independence from the Microcrystal Size

The variation in the amorphous volume fraction and the linewidth parameters with a variation in the amount of damage has been explained in the oscillator analysis section. A speculative explanation for the variation of the high frequency dielectric constant with microcrystal size now follows.

The behavior of ε_∞ can be understood if ε_{0p}, the static dielectric constant is assumed to be independent of microcrystal size. In that case, variations in ε_∞ with microcrystal size can be explained in terms of the uncertainty principle and a slightly modified Lyddane-Sachs-Teller relation. Figure 3.10 is a sketch of the real part of the dielectric function for GaAs [based on Blakemore]. The graph is labelled with the names used in the following explanation. There are two regions in the dielectric function; the first region is due to phonon excitations (greatly exaggerated for clarity), and here the Lyddane-Sachs-Teller relation applies, relating ε_{0p} to $\varepsilon_{\infty p}$. The second region corresponds to the electronic

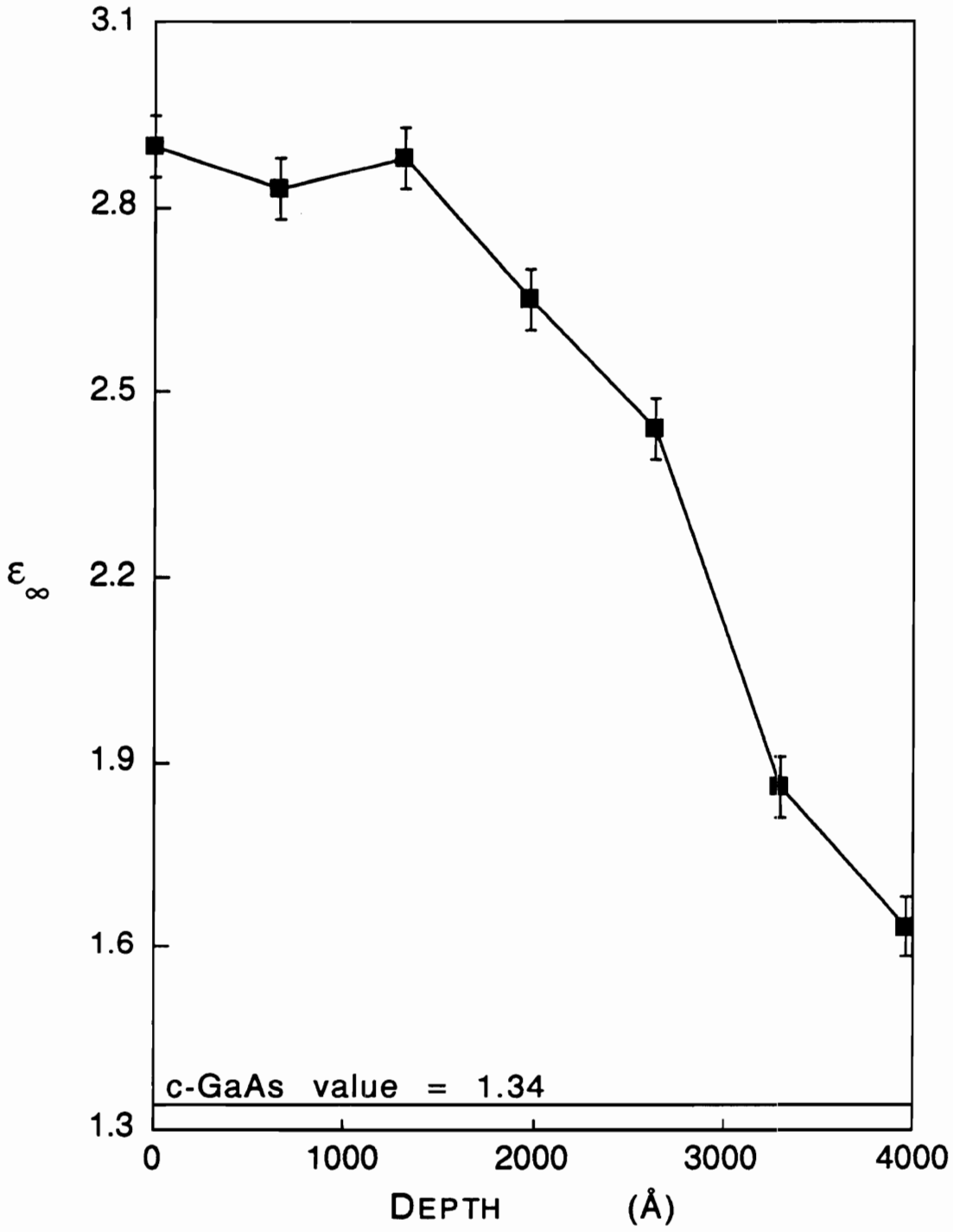

Fig. 3.9: High frequency dielectric constant vs. etch depth. A line is drawn at the c-GaAs value of 1.34. Error bars are estimated from fluctuations in the plateau region.

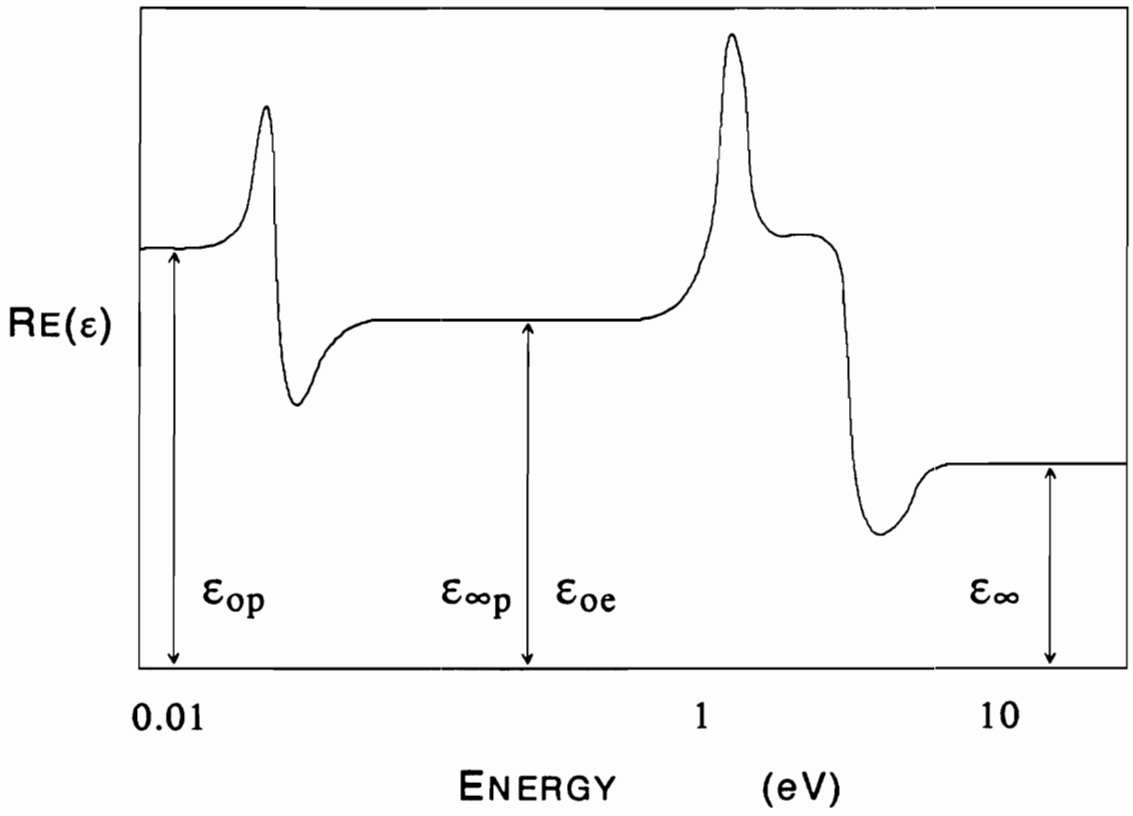

Fig. 3.10: A sketch of the real part of the c-GaAs dielectric function in the energy range 0.01 to 10 eV, based on figure 20 of Blakemore. The phonon region is greatly exaggerated for clarity. Regions where the function levels off are labelled by the values in those regions. The static dielectric constant, the high frequency dielectric constant in the phonon region, and the electronic high frequency dielectric constant are labelled as ε_{0p}, $\varepsilon_{\infty p}$, and ε_{∞} respectively.

excitations and is the region probed in this work. $\varepsilon_{\infty p}$ is equivalent to ε_{0e} which is the sum of ε_∞ and the squares of the ratios of the oscillator strengths to the oscillator positions.

Using the terminology of Figure 3.10, an expression for the static dielectric constant can be obtained using the oscillator parameters and a modified Lyddane-Sachs-Teller relation:

$$\varepsilon_{0p} = (\omega_L/\omega_T)^2 \left[\varepsilon_\infty + \sum (F_i/\omega_i)^2 \right] \qquad (3.8)$$

where ω_L and ω_T are the dominant longitudinal and transverse optic phonon frequencies in the microcrystal, respectively, and F_i and ω_i are the oscillator strengths and positions respectively. As the microcrystals decrease in size, their LO phonon peak positions (ω_L) and the F_i decrease. The ω_i hardly change. For the static dielectric constant to be independent of microcrystal size, ε_∞ must increase. Table 3.2 shows the quantities in equation 3.8 and a calculated value of ε_{0p} for all the samples. The samples hardly show any variation, and when a line was fitted to a graph of ε_{0p} vs. microcrystal size, a slope on the order of 10^{-6} and an intercept of 13.43 was achieved. This indicates that the value of ε_{0p} is constant with respect to variations in microcrystal size. The mean and standard deviation of this set of values for ε_{0p} was calculated to be 13.44±0.3. This is in excellent agreement with the value obtained by Samara of 13.19±0.39. The deviation observed for the 3 minute etched sample is due to the 7th oscillator which lies beyond the data region; although this oscillator accounts for contributions to the

Table 3.2: Quantities used in the calculation of the static dielectric constant from equation 3.7.

etch time, minutes	ω_L†, cm^{-1}	ω_T, cm^{-1}	$\sum (F_i/\omega_i)^2$	ε_∞	ε_{op}
0	288	269	8.68	2.90	13.27
1	288	269	8.57	2.83	13.07
2	288	269	8.85	2.88	13.43
3	289	269	9.56	2.65	14.09
4	290	269	9.07	2.44	13.38
5	290.55	269	9.72	1.86	13.51
6	291.05	269	9.69	1.63	13.27
c-GaAs	291.3	269	10.14	1.34	13.46
				mean±s.d.:	13.44 ± 0.3

†Values for these frequencies are based on Holtz et al.

dielectric function within the data range, ε_∞ and hence ε_{0p} are dependent on the accuracy of the fit of the 7th oscillator in its own energy region outside the collected data.

The variation of ε_∞ provides a connection between the Raman data and the reflectivity spectra; it shows the significance of the strength and energy position parameters of all the oscillators. ε_{0p} was shown to be constant despite the variation of most of the parameters (the energy positions were relatively constant) from sample to sample; in view of the fact that even small errors in these parameters could significantly change the computed value of ε_{0p}, its constancy is a tribute to the stability of the oscillator analysis.

CHAPTER FOUR
THE STRUCTURAL RECOVERY AND ELECTRICAL ACTIVATION OF SI-IMPLANTED GaAs AS A FUNCTION OF ANNEAL TEMPERATURE

4.1 Introduction

Raman scattering has been shown to be an effective technique for studying implantation-induced structural damage in GaAs [Pollak and Tsu; Nakamura and Katoda, 1982, 1984; Cardona, 1987; Duncan; Tiong et al.]. These studies have shown that under standard implant conditions, the near-surface damaged layer is a mixture of amorphous GaAs (a-GaAs) and microcrystalline GaAs (μ-GaAs). The longitudinal-optic (LO) phonon peak observed from the microcrystalline component changes in width, position, and intensity as the microcrystal size and microcrystalline volume fraction change. In this chapter, the LO peak is used as a structural probe in order to investigate the structural recovery of implanted-and-annealed GaAs as a function of anneal temperature.

Besides observing recrystallization, one can use Raman scattering to estimate carrier concentrations and depletion layer widths in implanted-and-annealed GaAs. The behavior of the LO peak in the presence of carriers has been studied for (100) Si implanted GaAs [Shen et al]. This use of Raman scattering is also exploited in this work, to complement the electrical studies [Sen], mentioned below.

Ultraviolet reflectivity can also be used to probe microcrystallinity

via finite-size effects on the interband spectrum [Feng and Zallen]. This method probes a shallower near-surface layer than does Raman scattering since, in the ultraviolet, the optical penetration depth is less than 100 Å [Aspnes and Studna]. Also, since depletion widths are much larger than this, UV reflectivity spectra are scarcely affected by free carriers. They yield information about the amorphous/microcrystalline composition of the damaged layer through the use of oscillator analysis and an effective medium approximation, as in chapter three.

The damage in ion implanted GaAs severely affects electrical characteristics. Implantation-damaged material is highly resistive. It is often assumed that the cause is that the implanted atoms are not located in substitutional (electrically active) sites. However, amorphicity (and consequent carrier immobility) may also play an important role [Holtz et al., 1986]. In this work, electrical transport properties (resistivity, mobility, and carrier concentration) of the annealed samples were studied by means of van der Pauw Hall-effect measurements and four-point-probe measurements [Sen].

Other studies [Tandon et al.; Nakamura and Katoda, 1985; Kato et al.] of the annealing behavior of Si-implanted GaAs indicate a two-step process where recrystallization occurs at a much lower temperature than that required to achieve electrical activation. This sequential nature seems to be present regardless of whether the anneal was a furnace anneal or an infrared rapid thermal anneal. However, although the sequence was identified

for infrared anneals, it has never been explicitly shown for furnace anneals. Those studies made use of photoluminescence, Bragg case x-ray double crystal diffractometry [Tandon et al.], Raman scattering from Si local vibrational modes [Nakamura and Katoda, 1985], and four point probe resistivity measurements [Kato et al.].

In this chapter, the results of Raman-scattering, ultraviolet reflectivity, and electrical experiments on a series of implanted samples which have undergone various post-implant furnace anneals are reported. Structural recovery is modelled in terms of an evolving amorphous/microcrystalline mixture. This model, along with damage depth profiles obtained by chemical etch for as-implanted and for 400°C annealed samples, also reveals that substantial re-growth originates from microcrystals within the damage layer. This process appears to be at least as important as epitaxial re-growth from the undamaged substrate.

4.2 Experimental Methods

The details about the samples and the optical measurements can be found in chapter two.

Electrical measurements were carried out [Sen] to get the mobility and carrier concentration for all samples. Resistivity values were also obtained for samples annealed at 525°C and above. Gold-germanium dots were placed on the samples at a temperature of 430°C for 2 minutes to form the ohmic contacts for the Van der Pauw measurements. Because of this required

additional heating which would change the characteristics of the low temperature annealed samples, the four point probe method was used to measure resistivity for samples annealed at temperatures below 525°C.

4.3 The Anneal Process

4.3.1 Optical Studies

Figures 4.1 and 4.2 show the development of Raman and reflectance spectra, respectively, as the (standard furnace) anneal temperature is increased. (The peak in each Raman spectrum is the LO phonon line; the broad amorphous GaAs Raman peaks have been removed). Both sets of spectra reveal that most of the damage from ion implantation is removed by 525°C, since both Raman and reflectance spectra look almost identical to their respective crystalline spectra at this temperature. The only noticeable difference between the 525°C reflectance spectrum and its crystalline counterpart is that the doublet structure is unresolved at 525°C, indicating residual damage for a shallow (<100Å) surface layer. The Raman spectra show that the crystal lineshape (peak positions, Full Width at Half Maximum (FWHM)) is recovered by 525 °C, but the intensity follows an unusual nonmonotonic behavior. This will be discussed in more detail later, when it will be shown that two phenomena influence the Raman intensity.

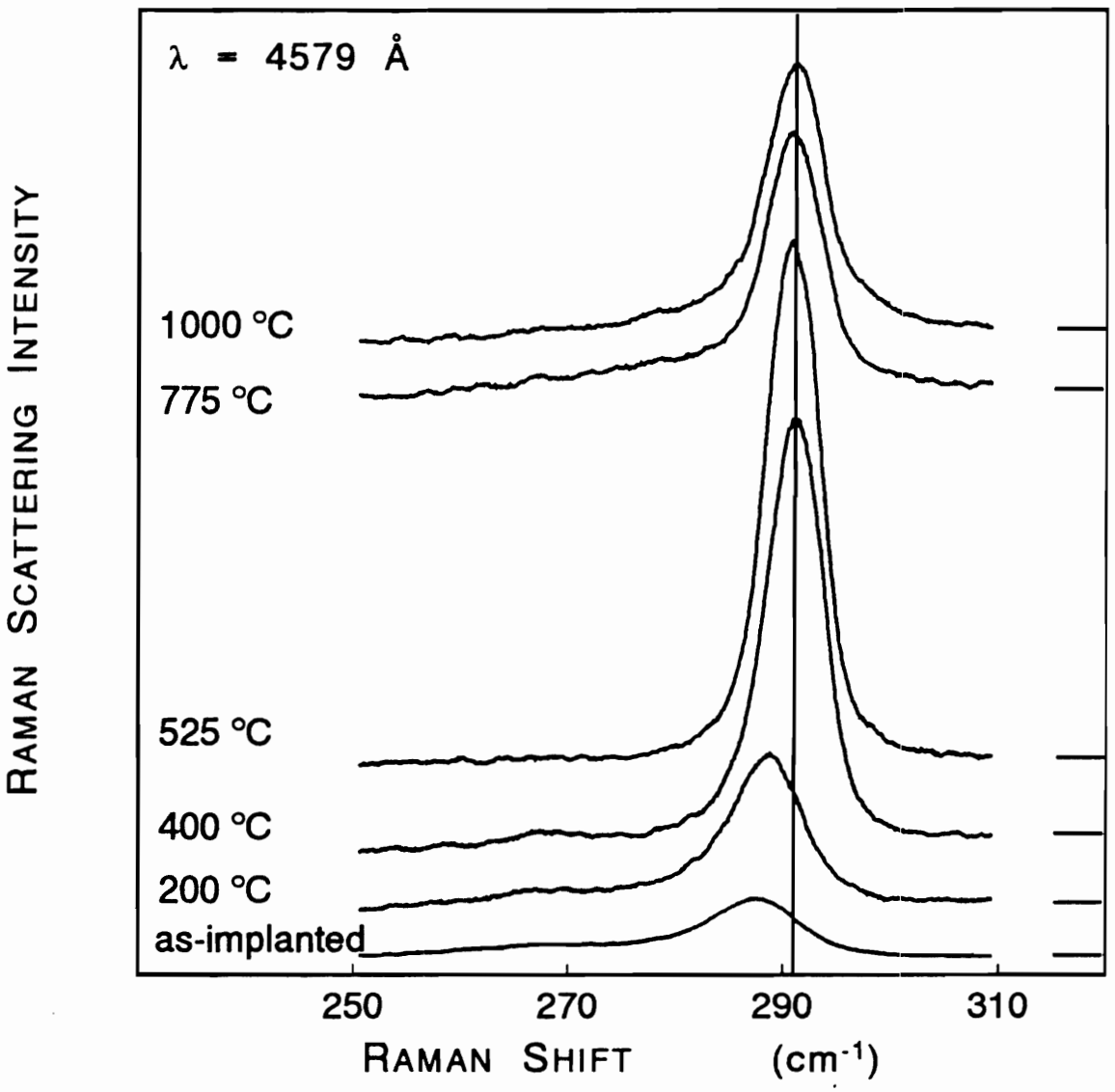

Fig. 4.1: Raman scattering spectra (taken at room temperature in near backscattering geometry using 4579 Å) following furnace anneal at the temperatures shown. The spectrum of the unannealed as-implanted material is at the bottom. All of the spectra are normalized to the same vertical scale by means of a c-GaAs reference standard. Baselines are shifted for clarity and are indicated by the tick marks on the right. The vertical line marks the LO position in c-GaAs.

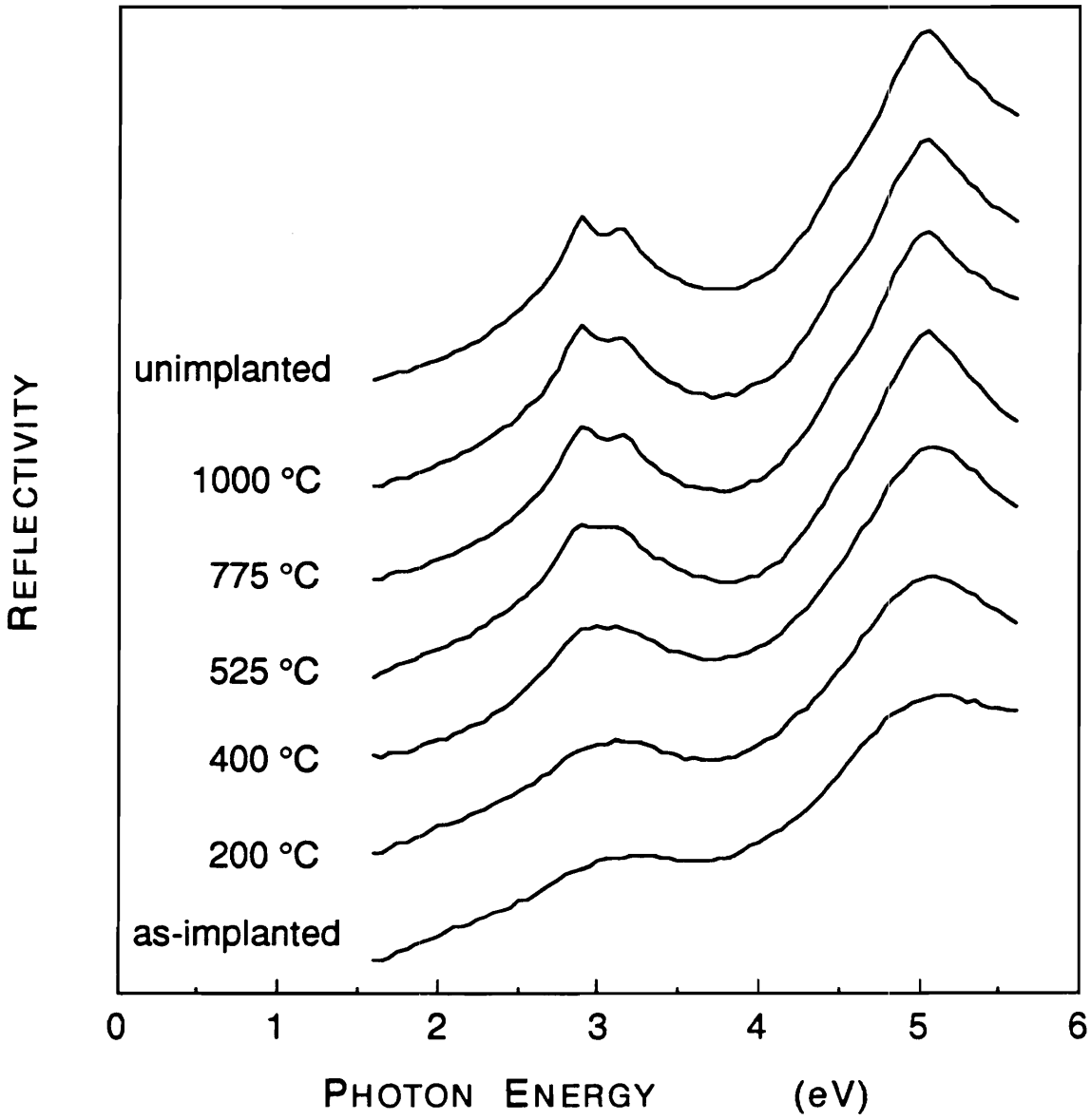

Fig. 4.2: Interband reflectivity spectra (taken at room temperature in near-normal incidence) following the furnace anneal at the temperatures shown. The reflectivity for a c-GaAs sample is shown at the top. The spectra are vertically shifted in equal increments.

4.3.1a Reflectivity

Since the reflectivity spectra probe a shallow surface layer at the critical points in the electronic joint density of states (E_1, $E_1+\Delta_1$, E_2) and the depletion region is much deeper than this surface layer (see Table 4.1 for depletion widths determined from Raman scattering), one does not have to worry about any possible changes in the dielectric function due to the presence of carriers, as long as the E_1, $E_1+\Delta_1$, and E_2 peaks are used for analysis. But even for the part of the spectrum that represents an optical penetration depth beyond the depletion widths in this study, the presence of carriers should not have a noticeable effect, if any, on the dielectric function because, if it did, the spectra in this region for the samples with high carrier concentrations would not look exactly like the unimplanted c-GaAs spectrum. Hence, this set of spectra provides purely structural information.

The spectra in Figure 4.2 were analyzed with seven oscillators as described in chapter three. For reflectance fits, the error function $\delta < 10^{-4}$, and for fitting to the dielectric function, $\delta \sim 10^{-3}$.

The parameters from the reflectance fit were then used to obtain the optical absorption coefficient, α, as a function of energy. This in turn was used to determine the amorphous volume fraction, f_a, from the approximate equation $\alpha = \alpha_a f_a + \alpha_c(1-f_a)$. Although this expression is only approximate since α_c, the c-GaAs α, is not the same as α_μ, the microcrystalline α, it is a fairly good approximation for regions away from the

Table 4.1: Optically derived depletion widths and carrier concentrations.

Sample	Depletion Width, Å		Carrier Concentration, cm^{-3}	
	4579 Å	6471 Å	4579 Å	6471 Å
525°C	–	1070	–	8 E 16
775°C	180	240	5.5 E 17	4 E 17
1000°C	200	180	4.7 E 17	5.5 E 17

critical points [Holtz et al., 1988; Feng and Zallen]. The region between 2.4 and 2.7 eV was used in this work. However, the optical penetration depth for this region for c-GaAs ranges from 200 to 500 Å and so it would seem that the actual region studied with this analysis is a 500 Å layer. From the damage depth profiles (Figure 4.10) one can observe a plateau out to at least 500 Å for samples annealed up to 400°C. For the as-implanted sample, although the plateau extends out to only 300 Å, the surface layer is mostly a-GaAs (60 to 80 %, see Figure 4.3a) and the optical penetration depth for a-GaAs is less than 150 Å for incident photon energies greater than 2.4 eV. (The optical penetration depth for a-GaAs was derived from α_a). For the samples annealed at higher temperatures, only the 525°C sample is not completely crystalline and has a very small damage layer (as evidenced by the similarity of their reflectance spectra to that of c-GaAs). Hence the material probed is uniform and the amorphous fraction obtained for this region can be used to study the top 100 Å layer. The only analysis which will not be as exact as the others is the analysis carried out for the 525°C sample; some improvement is possible using the f_a derived from the 4579 Å Raman spectrum (see discussion in the next section) since the probe depth is only 260 Å [Aspnes and Studna].

After obtaining the amorphous volume fraction, a reversal of the Bruggeman effective medium approximation would then yield the dielectric function for the microcrystals. Finally, this

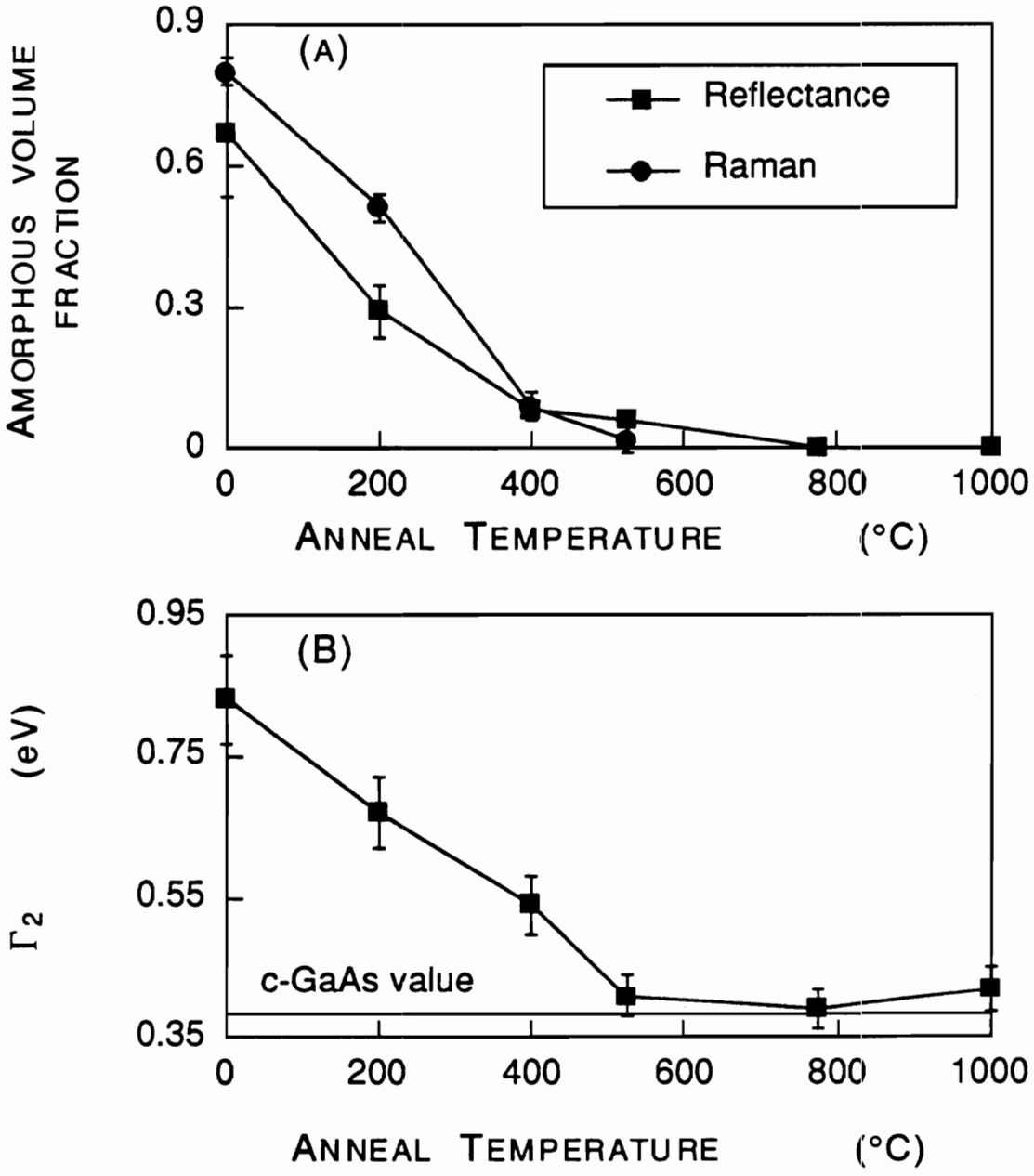

Fig. 4.3: (a) Amorphous volume fractions deduced from the Raman intensity results of Figure 5.1 and the reflectivity results of Figure 5.2. (b) Oscillator-analysis linewidth of the E_2 peak arising from the microcrystalline component in the damage layer.

function was fitted using the oscillator analysis and the parameters obtained were used (e.g. Figure 4.3) to provide an indication of the structural recovery of the material. For a more detailed account of this analysis method see chapter three.

Figure 4.3 displays the almost complete recovery of the crystal structure by 525°C. The linewidth, Γ_2, (in Figure 4.3b) of the oscillator corresponding to the E_2 peak in the microcrystals narrows as the anneal temperature is increased, and its value is practically the same as that in the crystal. (The value of Γ_2 for the as-implanted sample is taken for the sample as a whole rather than for the microcrystals alone since it was very hard to fit the dielectric function of the microcrystalline portion.) This linewidth is related to the size of the microcrystal via the uncertainty principle. A sharper line means a larger microcrystal size. Beyond 525°C the value is constant and is the same as that in the crystal. The amorphous volume fraction (Figure 4.3a) displays the same behavior as the Γ_2 linewidth; this analysis determines that recrystallization is essentially complete at 525°C. This is in agreement with previous studies showing recrystallization at 500°C [Kato et al., Shigetomi and Matsumori] and 550°C [Nakamura and Katoda, 1985].

4.3.1b Raman Scattering

In all analyses, the broad amorphous component of the spectra was subtracted out before getting the LO peak characteristics. Figure 4.4 shows the FWHM of the LO peak as a function of

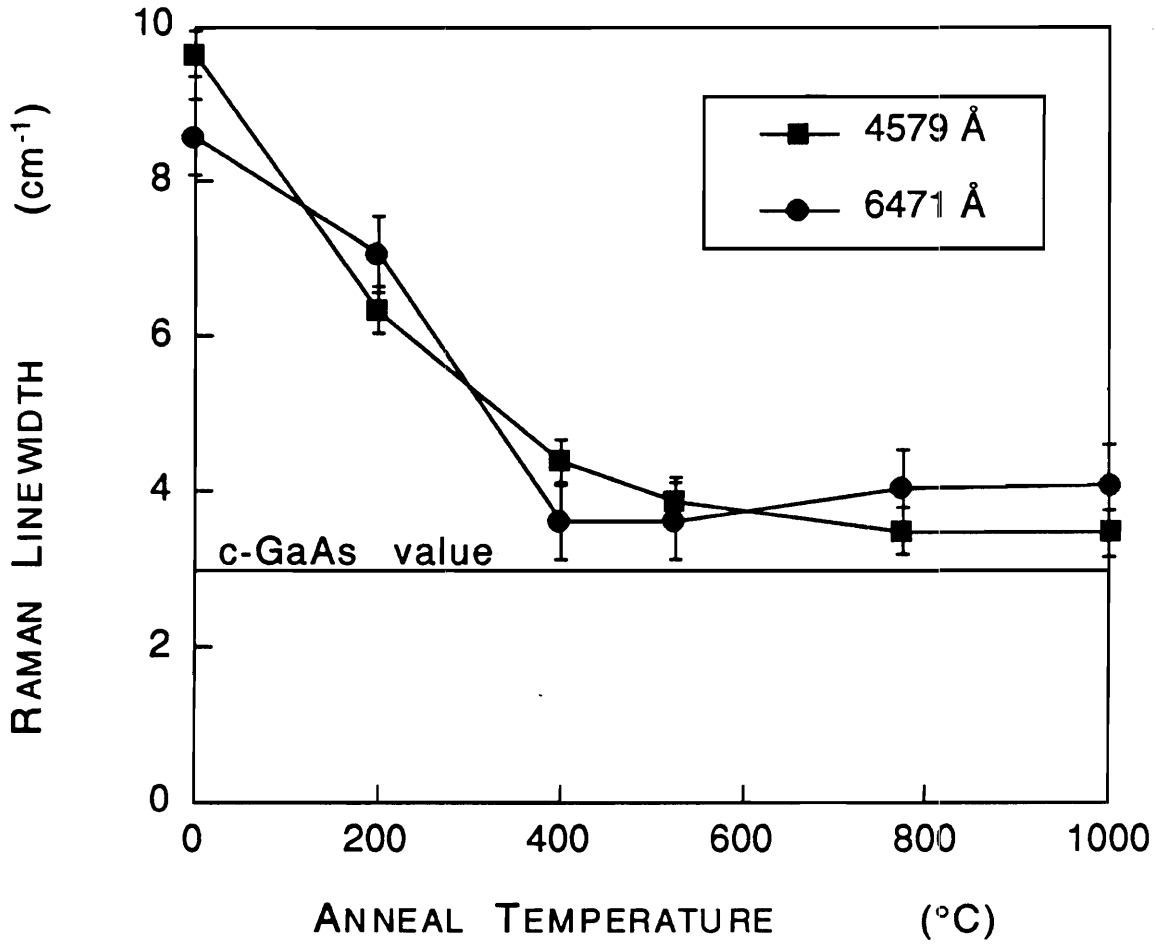

Fig. 4.4: Linewidth (FWHM) of the Raman LO peak as a function of anneal temperature. Squares represent data taken with 4579 Å light, while circles are for data taken with 6471 Å light.

anneal temperature. The 4579 Å light probes only the first 260 Å of the sample (probing depth = $1/(2\alpha)$), but the 6471 Å light goes to a depth of 1500 Å [Aspnes and Studna]. Differences in the spectra taken with the different lines are a result of differences in the material being probed. (The 6471 Å spectra are convolutions of different lineshapes since the damage decreases as one goes deeper into the sample. See Figure 4.10 for the damage depth profiles.) In both cases, at 525°C, the FWHM approaches a plateau. While the FWHM for the crystal is a little lower than the value at which the anneal sequence FWHM settled down to, the FWHM of the LO peak at 525 °C and above could be affected by the presence of carriers (note the higher values for the 6471 Å spectra for these temperatures). The dependence of the FWHM on the microcrystal size is explained in chapter one; the decrease in the LO FWHM indicates the onset of recrystallization as the microcrystals get bigger.

Figure 4.5 displays the behavior of the LO peak intensity (normalized to that of c-GaAs) as a function of anneal temperature. Once again, at 525°C, the intensity is restored, to within experimental error, to the value for c-GaAs indicating structural recovery. An estimate of the amorphous volume fraction can be obtained from the following equation, suitable for the spectra obtained with the 4579 Å line:

$$f_a = 1 - \{I^*\alpha_a \; / \; [\alpha_c + (\alpha_a - \alpha_c)^*I \;]\} \qquad (4.1)$$

In this equation, I is the normalized LO intensity. An assumption

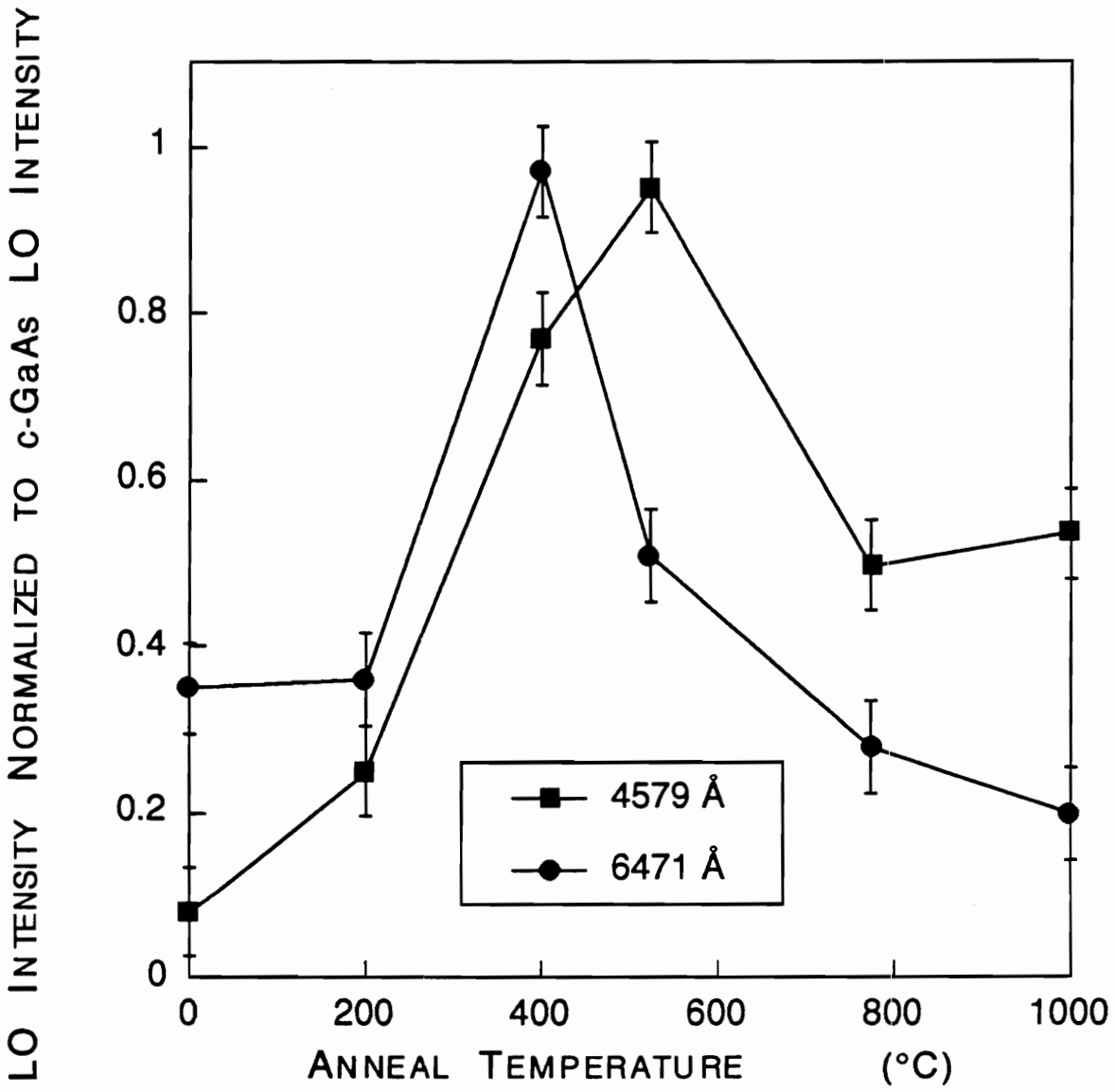

Fig. 4.5: Intensity of the Raman LO peak (normalized to c-GaAs LO peak) as a function of anneal temperature. Squares represent data taken with 4579 Å light, while circles are for data taken with 6471 Å light.

is made that the material probed is uniform in the amorphous volume fraction and that the absorption coefficient of the material can be expressed by $\alpha = \alpha_a f_a + \alpha_c(1-f_a)$. The equation above is derived from the equation:

$$I = \frac{\int_0^\infty f_C(x)\exp\left(-2\int_0^x \alpha(x')dx'\right)dx}{\int_0^\infty \exp(-2\alpha_C x)\,dx} \qquad (4.2)$$

The amorphous volume fractions derived from equation 4.1 are plotted in Figure 4.3, for anneal temperatures up to about 500 °C. There is an additional mechanism which enters at higher anneal temperatures. This mechanism is responsible for the pronounced dropoff in LO intensity evident on the high-temperature side of Figure 4.5.

Samples annealed to 525°C or higher are essentially complaetely crystalline, as shown by the interband reflectivity spectra. Yet these samples exhibit LO Raman intensities weaker than that characteristic of c-GaAs. It is known that such a reduction in intensity occurs in the presence of carriers [Shen et al., Pinczuk et al., Mills]. A high carrier concentration means a shallow depletion region. If the penetration depth of the incident laser light is larger than the depletion width, some of the light will penetrate the carrier-containing region. Within this region, the LO phonon is exponentially damped out as it is replaced by

coupled phonon-plasmon modes at shifted frequencies. The observed LO intensity is therefore decreased when the depletion width becomes smaller than the optical penetration depth, and the depletion width in turn decreases with increasing carrier concentration. This effect therefore provides a Raman-based handle on the size of the carrier concentration, at high carrier concentrations.

For the high temperature anneals, an estimate of the depletion width can be obtained from the normalized (relative to c-GaAs) LO intensity. Within the depletion layer, the Raman efficiency is taken to be the same as that of c-GaAs. The observed intensity dropoff is then attributed to the optical penetration into the carrier-containing layer beneath the depletion layer, since the carrier-containing layer does not contribute to the LO scattered intensity. The normalized LO intensity, I, can then be written as [Pinczuk et al.]:

$$I = 1 - \exp[-L_d / d_{opt}] \qquad (4.3)$$

where L_d is the depletion layer width and $d_{opt} = 1/(2\alpha)$, the optical penetration depth of the incident light. Note that to make this estimate, the probing light must pass through two layers: first a depletion region, then a region with a carrier concentration greater than 10^{16} cm^{-3}. (See next paragraph for an explanation of this value.) If the probing light were to go beyond the second region into a layer where the material behaves as virgin c-GaAs, corrections would have to be made to exclude this

layer. (Such corrections were made for the 775 and 1000 °C annealed samples probed with the 6471 Å light). For 6471 Å light ($d_{opt} = 1/(2\alpha_c) = 1500$ Å), only 55% of the signal penetrates the top 1200 Å layer :

$$\frac{\int_0^{1200\text{Å}} \exp(-2\alpha_C x)dx}{\int_0^{\infty} \exp(-2\alpha_C x)dx} = 0.55 \qquad (4.4)$$

A crude correction is made by multiplying the measured c-GaAs normalized intensity by 55% before solving for the depletion width. The results of the corrections are in good agreement with the electrical measurements.

From these depletion widths, the carrier concentrations can be derived using the analysis of Shen et al. Briefly, the method is as follows. Poisson's equations are solved for the depth, x, as a function of the potential at x, V(x). The depth at which the potential, V_0, implies a carrier concentration, N, of less than or equal to $N_0=10^{16}$ cm^{-3} (by way of the net positive charge density, ρ) is then considered to be the depletion width; $V(L_s) = V_0$. (The method is insensitive to the choice of N_0 as long as it is less than 10^{16} cm^{-3}; when $N \leq 10^{16}$ cm^{-3}, the plasmon frequency ω_p^+ is equal to the LO phonon frequency.) The expression for L_s contains information about the donor concentration N_D also via ρ; from equations (e.g., Yang) relating

N and N_D for non-degenerate material ($N < 10^{18}$ cm^{-3}) N can be expressed in terms of L_s (Figure 1.8).

Using this analysis, the carrier concentrations were derived and are shown in Table 4.1. The value for N for 525°C is determined using the 6471 Å Kr laser line. The 4579 Å incident light could not detect the depletion width for this sample since its penetration depth was too shallow for it to probe the plasmon region.

The values of the carrier concentration show that a maximum is reached at 775°C. The value at 525 °C is less than half of the final value. While the structural recovery at 525 °C was practically complete, electrical activation was not even half done; electrical activation was completed by 775 °C. A sequence in temperature involving two decoupled processes is therefore observed; structural recovery occurs first, at 525 °C, then electrical activation is achieved by 775 °C.

4.3.2 Electrical Studies

Figure 4.6 [Sen] is a plot of the mobility vs. anneal temperature. Damage reduces the electron mobility in a sample. This can be seen by comparing the mobility of the 775°C annealed sample (structurally recovered as indicated by optical experiments) with that of the unannealed sample. The restoration of high values of mobility is therefore an indication of structural recovery. Figure 4.6 shows that structural recovery is achieved by 525°C, since this is the temperature at which the value of

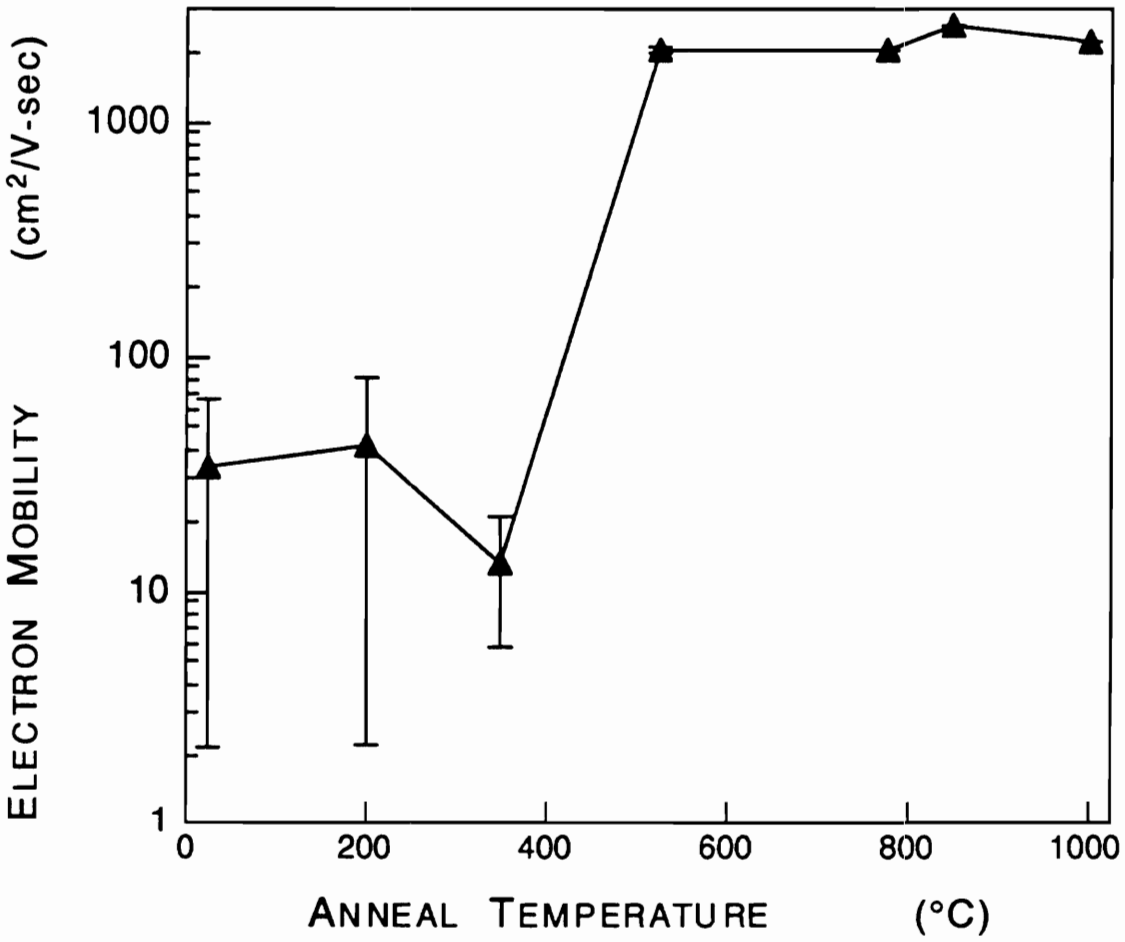

Fig. 4.6: Electron mobility vs. anneal temperature.

the mobility starts to level off.

Figure 4.7 [Sen] also shows that structural recovery occurs at 525°C. The resistivity increase in the low temperature region is similar to the observations of Kato et al. This may be attributed to the annealing out of defect-induced hopping states. At 525°C, the resistivity drops by over three orders of magnitude. Thereafter, the effect saturates. This is in agreement with the plot for mobility, indicating that a different conduction process is now involved (conduction band electrons). This step becomes possible when recrystallization is accomplished.

Figure 4.8 is a plot of carrier concentration vs. anneal temperature. (For samples annealed at lower temperatures, the carrier concentration values in Figure 4.8 are upper limits since the hopping conductivity was not subtracted from the dc conductivity in the calculations for the carrier concentration.) The values obtained from van der Pauw measurements [Sen] are in very good agreement with the values obtained from the Raman LO peak intensities. They also show that the carrier concentration at 525°C is less than half of its final value, which is achieved by 775°C.

4.3.3 The Separation of Structural Recovery and Electrical Activation

The electrical studies support the same conclusion as the optical studies: the temperature-range separation, during annealing, of structural recovery and electrical activation. Crystallinity is

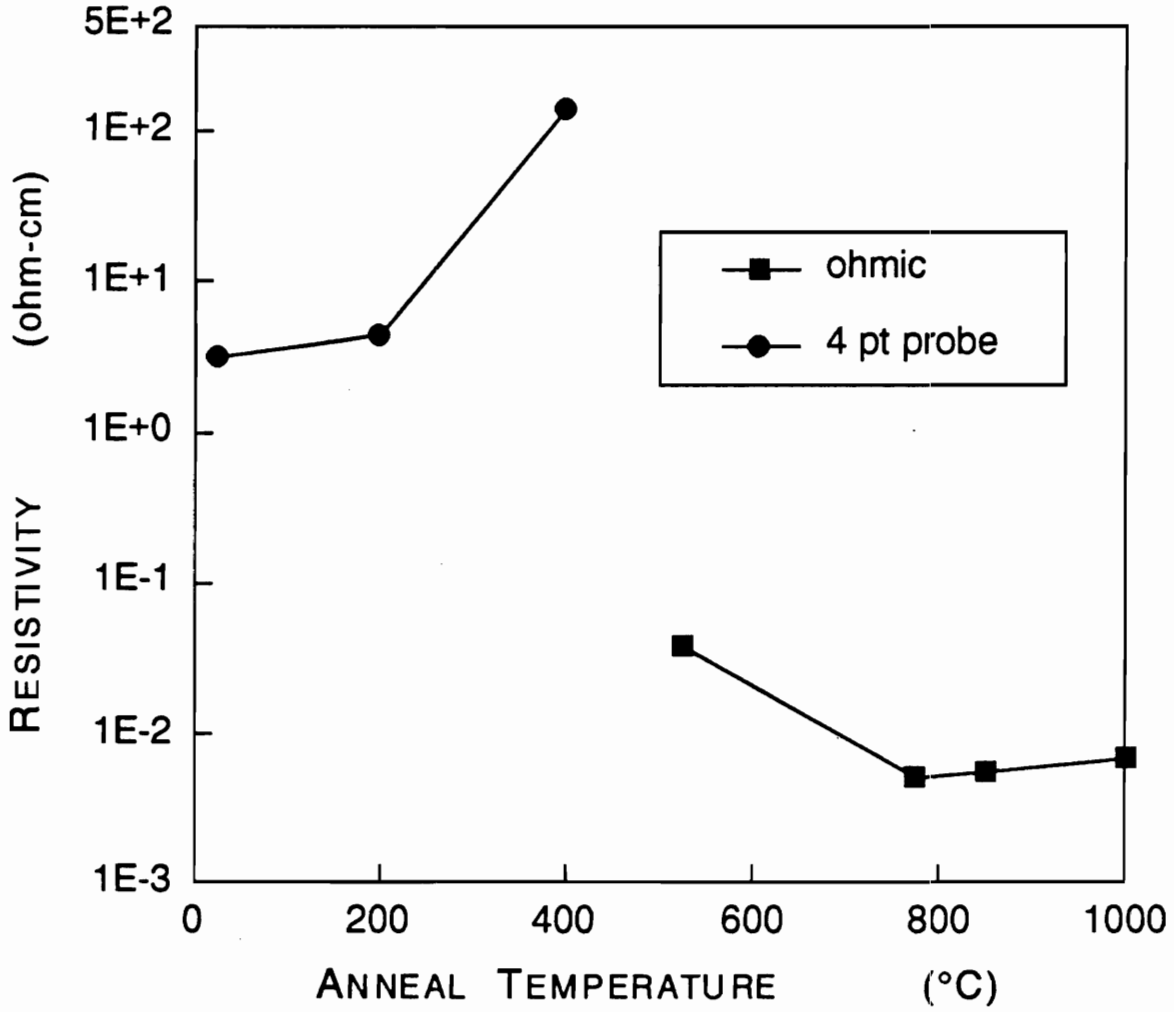

Fig. 4.7: Resistivity vs. anneal temperature. Error bars are obscured by the symbols.

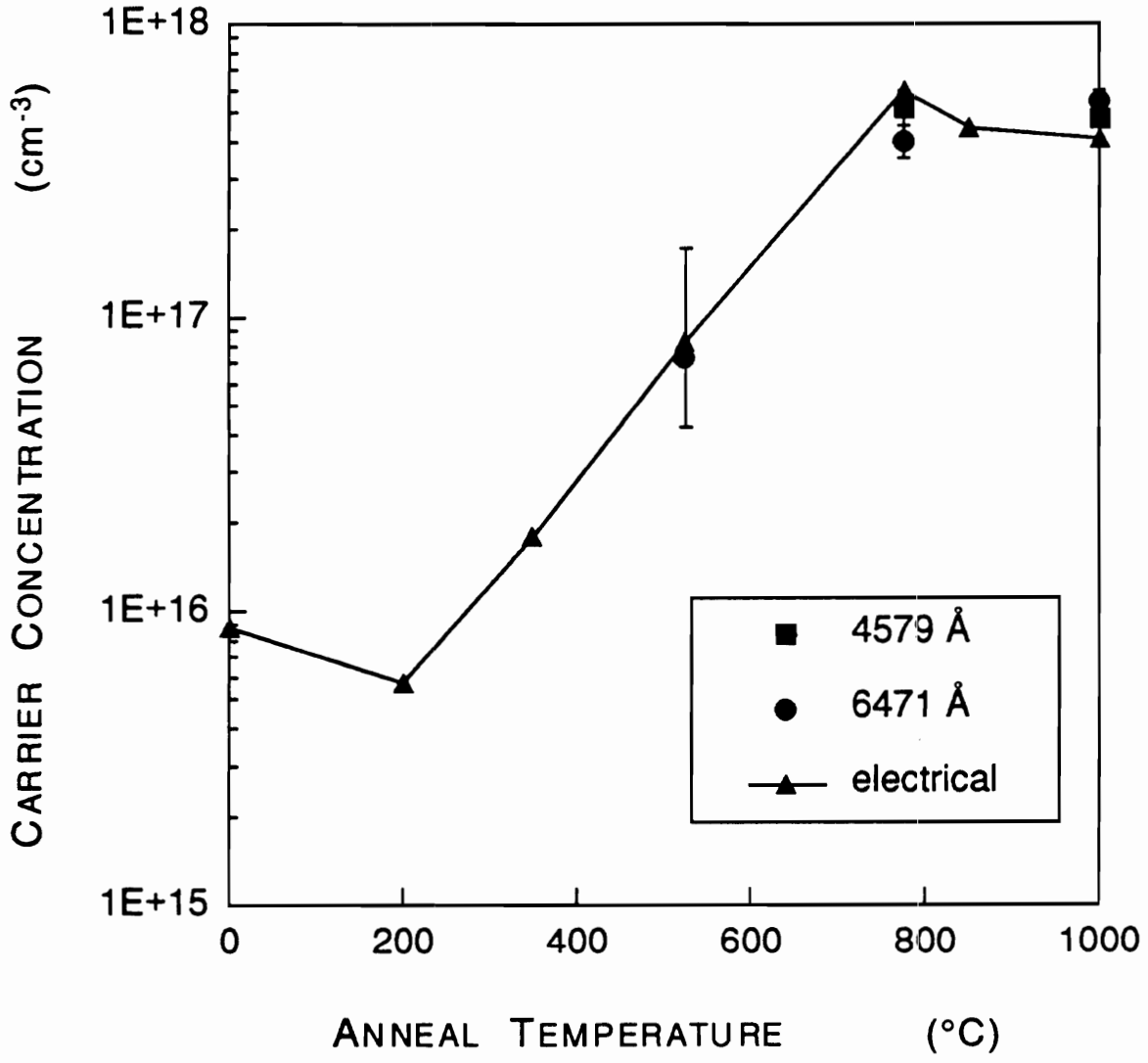

Fig. 4.8: Carrier concentration as a function of anneal temperature. Values at temperatures below 525°C represent upper limits. Squares represent values derived from Raman measurements with 4579 Å light, circles represent Raman derived values as well but for 6471 Å light, and triangles (connected by straight lines) represent electrical measurements. Some error bars are obscured by the symbols.

recovered first by 525°C, as evidenced by the mobility measurements; while electrical activation is not completed until after 775°C, as shown by the carrier concentration. Figure 4.9 displays this sequence. The activation efficiency, η ($\eta \equiv N \cdot L_n/F$, where N is the carrier concentration, L_n = 1200 Å is the implanted layer width, and F = 4×10^{13} cm^{-2} is the implant fluence), and the inverse of the linewidth of the LO Raman line are plotted against the anneal temperature. The inverse Raman linewidth is a measure of the structural recovery toward crystallinity, while the activation efficiency gauges the electrical activation. The lag in the activation efficiency relative to the Raman linewidth strikingly demonstrates the decoupling of the recrystallization and electrical activation processes. At 525°C anneal, structural recovery (a.k.a. recrystallization a.k.a. "healing") is essentially complete, but electrical activation has barely begun.

The higher temperature required for electrical activation can be explained by the need for higher temperatures to remove residual defects (interstitials, vacancies) and to allow the interstitial Si atoms to move into Ga sites. In order to facilitate the discussion, assume that the number of defects left in the sample after annealing at 525°C is equal to the difference between the carrier concentrations at 775°C and 525°C. This puts the number of Si interstitials that need to go into Ga sites at about 10^{17} cm^{-3}. With about 10^{23} atoms per cm^3 in a typical crystal, the number of defects is 1 in 10^6 atoms. This is hardly enough to change crystalline characteristics, but it can have an appreciable

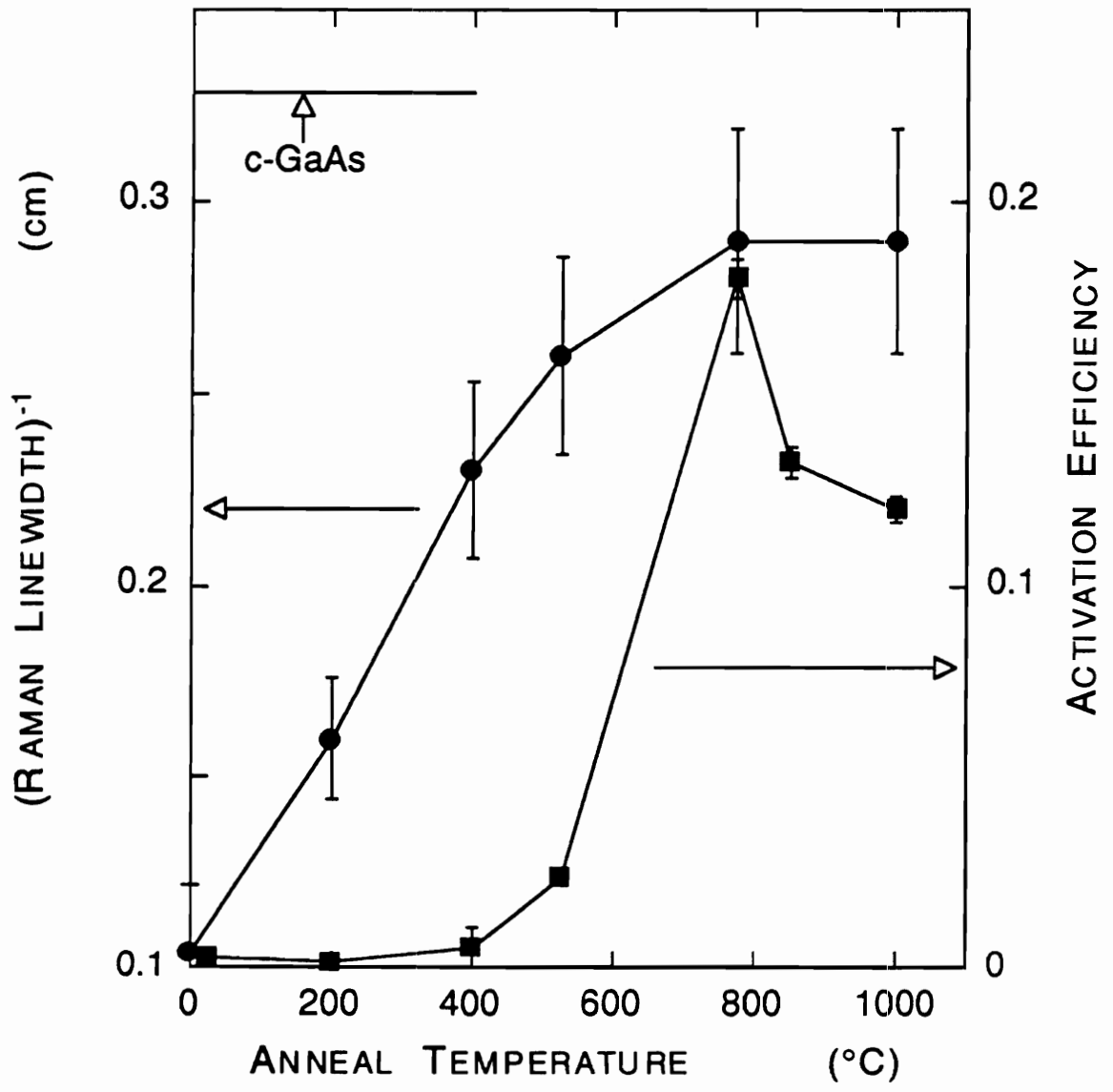

Fig. 4.9: The inverse FWHM (1/FWHM) (left hand axis) and the activation efficiency (right hand axis) are plotted as a function of anneal temperature. The activation efficiencies are upper limit values for temperatures below 525 °C; electrical measurements were used to derive the activation efficiencies. The inverse FWHM are taken from the 4579 Å Raman spectra.

effect on the number of carriers present. Note also that the carrier concentration drops at 1000°C, probably because of an increase in defects due to arsenic evaporation; again, the structural characteristics have not been affected, showing that the electrical activation is more sensitive than the structural recovery to the presence of a small number of defects. To improve the carrier concentration, it is important to anneal out these defects without introducing new ones.

These results are not in conflict with other studies that suggest a one-step process where electrical activation corresponds to recrystallization [Holtz et al.,1986]. Si localized vibrational modes for Si_{As} (silicon at an arsenic site) and Si_{As} - Si_{Ga} (silicon on neighboring sites) were observed in Raman spectra even before annealing, and it was suggested that annealing only serves to provide a crystalline structure. However, it is very hard to observe the Si_{Ga} (silicon at a gallium site) LVM and a measurement of the intensity of this mode would provide information on the number of carriers [Nakamura and Katoda, 1985; Wagner et al.,1990]. If such a measurement were to be done, the Si_{Ga} mode intensity would be expected to increase with anneal temperature even beyond the temperature for which the LO intensity has reached its value in the crystal. The ratio of the intensity of the Si_{Ga} mode to that of the LO peak should remain constant after recrystallization is achieved if electrical activation and structural recovery were the same process. Since no such study has been made, there is no conflict with the

results in this work. These results simply show that even if some Si atoms were already present at Ga sites, higher anneal temperatures are required to increase their number. In fact, an increase in the number of Si_{Ga} has been indirectly observed with cathodoluminescence as order is restored to the crystal [Gray et al.].

4.4 Microcrystals as Seeds for Crystal Growth

Figure 4.10 shows the Raman LO FWHM as a function of etch depth for the as-implanted sample and the 400°C sample. It is generally accepted that the interface between the damaged layer and the crystalline region advances toward the surface (epitaxial regrowth). This is in fact observed; the FWHM for the 400°C sample is restored to the value in the crystal after a depth of 1000 Å in contrast to the 1600 Å depth in the as-implanted sample. However, the FWHM values for the 400°C sample are consistently lower than the values for the as-implanted sample at each depth. Since the damaged layer-crystalline region interface has only moved up to 1000 Å, it is clear that crystalline growth is occurring throughout the whole damage layer and therefore the microcrystals are acting as seeds for crystal growth. This agrees with the interpretation of recrystallization occurring from both the surface and interface regions in the study of Nakamura and Katoda (1982). They suggested that the partly crystalline region was acting as a seed for crystal growth.

This observation is not inconsistent with studies showing

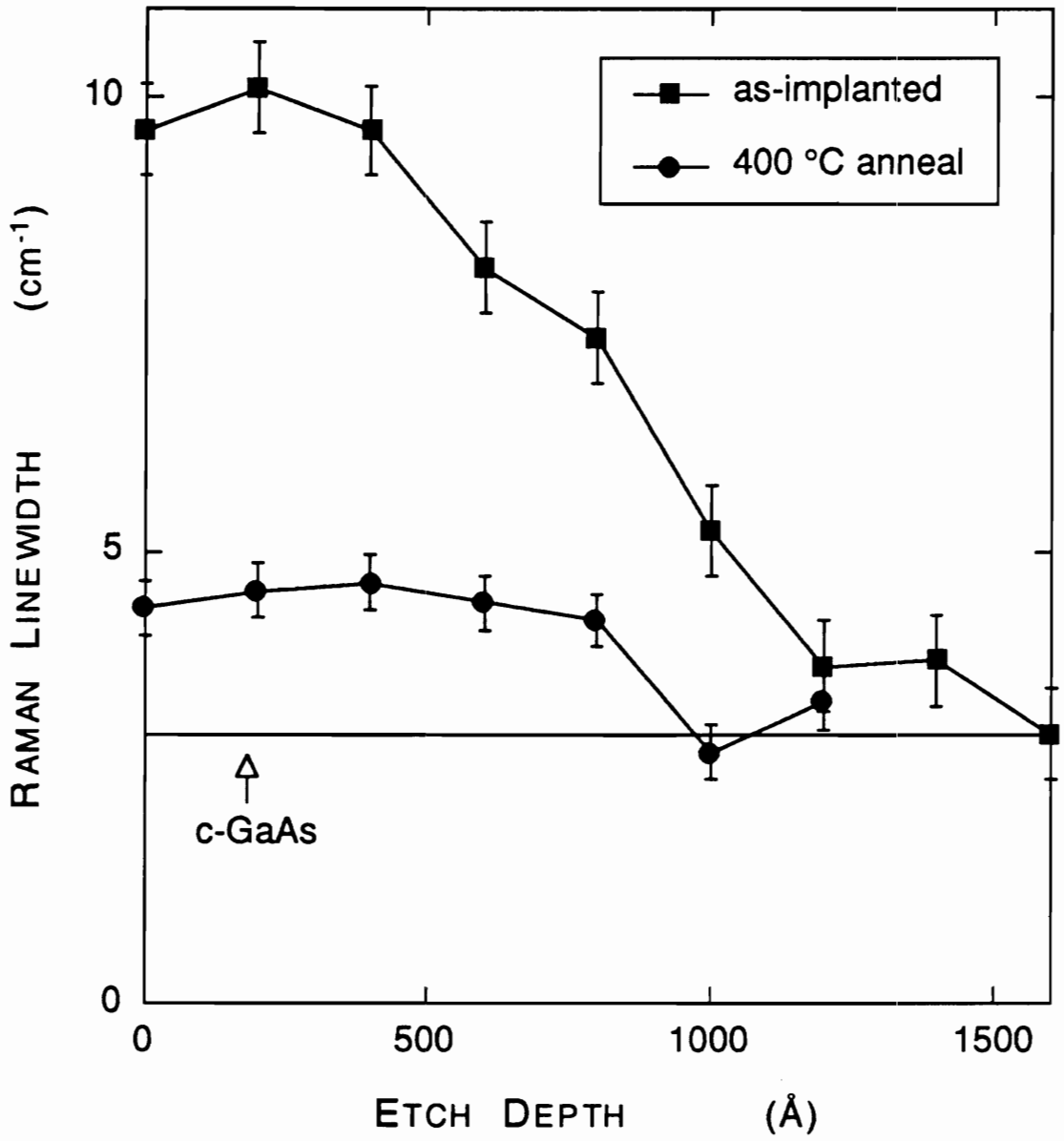

Fig. 4.10: FWHM damage depth profiles for the as-implanted (squares) and 400 °C (triangles) samples.

that crystal regrowth is epitaxial. Figure 4.11 shows the Raman scattering selection rules for the LO peak due to the microcrystals. In the configuration where the LO peak is forbidden for (100) GaAs, the microcrystal LO peak is missing. It is very clearly present over the amorphous GaAs bands in the configuration where LO phonon scattering is allowed. This means that the microcrystals retain the orientation of the unimplanted crystal. Hence, the microcrystals can act as properly oriented seeds; the damage layer-c-GaAs interface does not have to sweep to the surface to correct for misorientation.

An estimate of the growth rates can be obtained by invoking the spatial correlation model to estimate the sizes (mean diameter, L) of the microcrystals in the implanted layer. From this model, the average microcrystal diameter at the surface of the as-implanted sample is about 45 Å. After 400°C annealing, the diameter in the surface region increases to 85 Å. Therefore, at the surface, the growth rate is about 0.1 Å/°C.

The regrowth at the surface of the sample annealed at 400°C is mainly due to the increase in the microcrystal size rather than the joining of microcrystals to form fewer but larger microcrystals. This can be observed by noting that the number of microcrystals does not decrease after 400°C annealing. The number of microcrystals can be given by

$$N_{\mu c} = f_c V / V_{\mu c} \qquad (4.5)$$

where $N_{\mu c}$ is the number of microcrystals, f_c is the crystalline

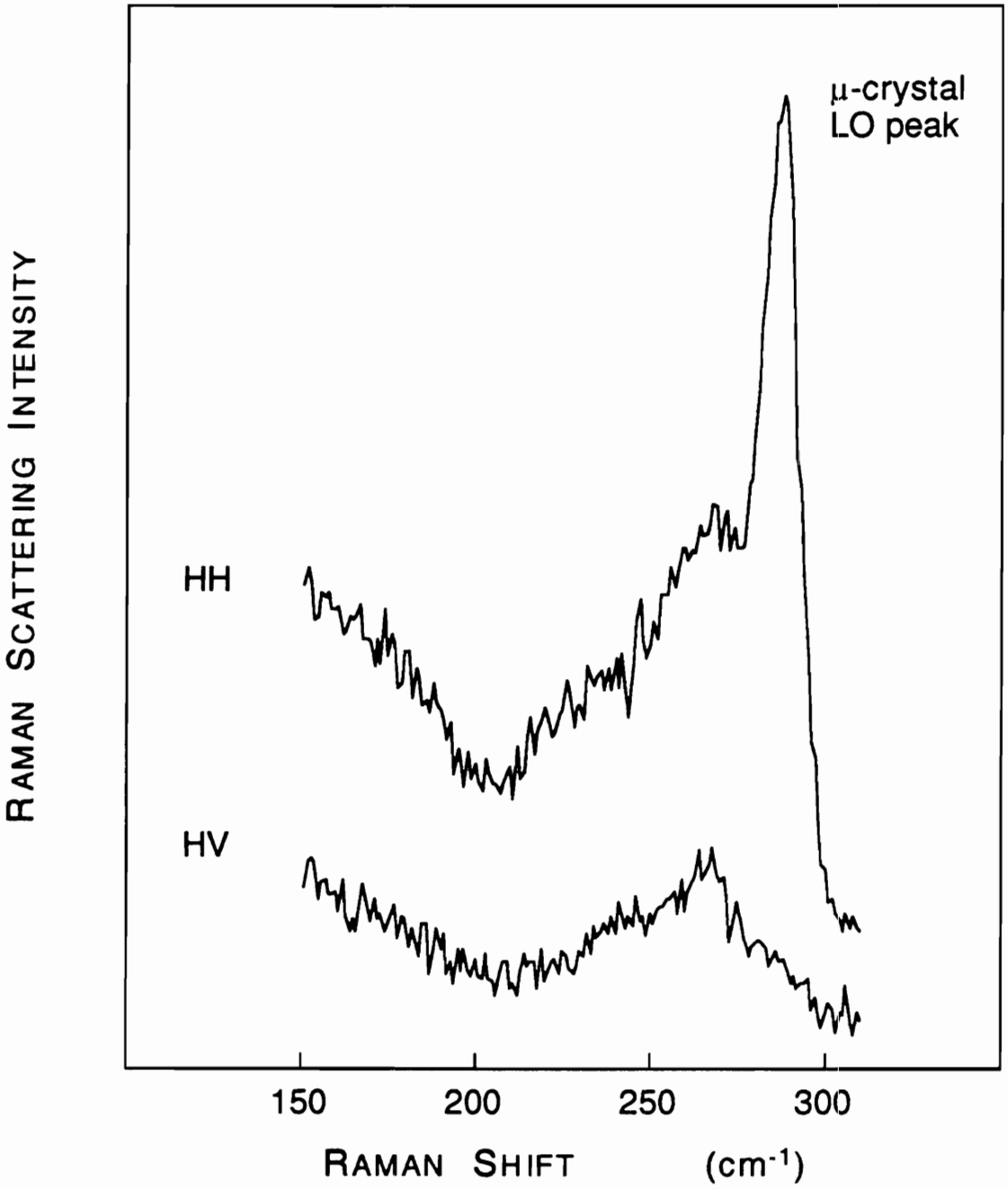

Fig. 4.11: Microcrystal selection rules. The top spectrum corresponds to an HH configuration and the bottom one corresponds to an HV configuration. H is parallel to (011) and V is parallel to $(0\bar{1}1)$. The broad bands are the amorphous GaAs component. The sample used here was the as-implanted one.

volume fraction, V is the total volume probed and $V_{\mu c}$ is the volume of a microcrystal with mean diameter L. Since V is constant, the number of microcrystals is proportional to f_c/L^3. Using the crystalline volume fractions calculated from the Raman intensities and the microcrystal sizes estimated from the FWHM of the Raman LO peak, the values for f_c/L^3 are 2.2 x $10^{-6}/Å^3$ and 1.5 x $10^{-6}/Å^3$ for the as-implanted and 400°C annealed samples, respectively. Within experimental error (mainly from the estimate of the microcrystal size) the number of microcrystals is constant. It is however, possible that some microcrystallites have grown together, causing a slight drop in the number of microcrystals.

At the damaged-undamaged interface region, the growth is much faster. A combination of regrowth processes is occurring here; both regrowth from the interface as well as microcrystal regrowth occur. Since the number of microcrystals in the layer between 1200 and 1600 Å is 2 orders of magnitude less than in the top layer, and the microcrystalline diameter is quite large (>400 Å), not much regrowth is needed to make this layer completely crystalline. Assuming that the major regrowth process in this layer is the joining of microcrystals, and that between 1200 and 1000 Å the major growth mechanism is the movement of the interface, then the interface advances by 200 Å after 400°C so the growth rate is 0.5 Å/°C. These numbers agree fairly well with the values given by Yoshida and Katoda for the annealing of heavily damaged material (implant fluence ~ 10^{16}

cm^{-2}) in the anneal range of 400 to 700 °C. They observed that the rate at the surface was 0.1 Å/°C and at the interface it was 0.3 Å/°C. (However, since their estimation for the rate at the interface was based on a Raman signal that also probed the surface region, one would expect a higher value for the rate at the interface.) Although the growth rates observed in this study are taken at a lower temperature range than the range for the growth rates of Yoshida and Katoda, the samples used in this study are less damaged (prior to any anneals) than the samples of Yoshida and Katoda; it is therefore reasonable to expect similar growth rates for lower anneal temperatures.

CHAPTER FIVE
(211) VERSUS (100) SILICON-IMPLANTED GaAs: A RAMAN-SCATTERING AND ULTRAVIOLET-REFLECTIVITY COMPARISON STUDY

5.1 Introduction

A recent report [Banerjee et al.] on improved device performance for Si-implanted GaAs MESFETs made with (211) GaAs substrates instead of the traditional (100) face prompted a study which showed only slight differences between (211) and (100) faces [Epp et al.]. Those differences favored (100) instead of (211) faces for device applications. The unusual carrier concentration profiles previously observed for the (211) face were not observed in that work, and the (100) face showed a flatter profile than the (211) face.

The Raman experiments by Epp et al. are reviewed in this chapter; the slight differences found between the (211) and (100) faces prompted the Raman experiments in this study for similar samples that were implanted at a higher fluence. Ultraviolet reflectivity spectra were also taken and it will be shown that they roughly agree with the Raman data.

Also, in this chapter, a new method of interpreting reflectivity data is developed in order to deal with etchant induced surface roughness. It seems that the samples implanted at higher fluences were more susceptible to becoming rough when exposed to the chemical etch used in this study.

5.2 Experiments

The samples used and the general details of the experiments are described in chapter two.

Incident light was polarized perpendicular to the scattering plane, and both polarizations of the scattered light were collected. The samples were oriented so that the LO peak would appear (incident light polarized parallel to $(0\bar{1}1)$ for (211) and parallel to $(0\bar{1}1)$ or (011), depending on the dimensions of the sample, for (100)). The back sides of these samples were used for normalization purposes (since they are c-GaAs surfaces of optical quality) and were mounted so as to have the same incident polarization as the front side. Raman spectra for the 1.7 x 10^{13} cm^{-2} implanted and annealed samples (850°C, 30 second rapid thermal anneal) were collected under the same conditions, except that the laser line was 4880 Å.

5.3 Raman results

The LO Raman linewidth (the FWHM, full width at half maximum) for our various samples was measured. The Raman linewidth in implantation-damaged GaAs is increased by finite-size effects since the surviving crystalline fraction becomes nanocrystalline. The greater the damage, the finer the microcrystals become and the larger the linewidth becomes [Tiong et al.; Holtz et al., 1988].

Table 5.1 shows the Raman selection rules for both LO (longitudinal optical) and TO (transverse optical) peaks for

Table 5.1: Raman scattering backscattering selection rules for the (211) face of zincblende materials as a function of θ, the angle between x and $(\bar{1}11)$.

Configuration	LO	TO
$z(xx)\,\bar{z}$	$(2/3)\,(d_{LO})^2 \sin^4\theta$	$(4/3)(d_{TO})^2$ [$9\cos^2\theta(\ (\sin^2\theta)/2 - (\cos^2\theta)/3\ )^2 + \sin^2\theta(\ 2\cos^2\theta - (\sin^2\theta)/2\ )^2$]
$z(xy)\,\bar{z}$	$(2/3)(d_{LO})^2(\sin^2\theta)^* \cos^2\theta$	$(4/3)(d_{TO})^2$ [$\cos^2\theta\ (\ (\cos^2\theta)/2 - 2\sin^2\theta\ )^2 + \sin^2\theta\ (\ 2\cos^2\theta + (\sin^2\theta)/2\ )^2$]
$z(yy)\,\bar{z}$	$(2/3)\,(d_{LO})^2 \cos^4\theta$	$(4/3)(d_{TO})^2$ [$\cos^2\theta\ (\ (\cos^2\theta)/2 - 2\sin^2\theta\ )^2 + 9\sin^2\theta\ (\ (\sin^2\theta)/3 - (\cos^2\theta)/2\ )^2$]

where x, y, z are unit vectors:

$x = (-(\cos\theta)/\sqrt{3},\ ((\cos\theta)/\sqrt{3})-((\sin\theta)/\sqrt{2}),\ ((\cos\theta)/\sqrt{3})+((\sin\theta)/\sqrt{2}))$

$y = ((\sin\theta)/\sqrt{3},\ (-(\sin\theta)/\sqrt{3})-((\cos\theta)/\sqrt{2}),\ (-(\sin\theta)/\sqrt{3})+((\cos\theta)/\sqrt{2}))$

$z = (2,\ 1,\ 1)/\sqrt{6}$

(211) zincblende surfaces, in the backscattering configuration. Very general polarization directions were used in order to find out for which value of θ (measured from $(\bar{1}11)$) will the ratio of LO to TO peak intensities be a maximum; that value was determined to be $\theta = \pi/2$ from the selection rules in Table 5.1. The selection rules for $\theta = \pi/2$ are shown in Table 1.3. The polarization configuration in these experiments was chosen in order to minimize the difficulty of extracting the TO peak to isolate the characteristics of the LO peak. For (100) surfaces, the backscattering selection rules are much simpler; only the LO peak is allowed. See Table 1.3.

In all the Raman spectra, the TO peak as well as the broad band arising from the presence of amorphous GaAs were subtracted before the FWHM of the LO peak was measured and used to quantify the damage.

Figures 5.1 and 5.2 show the Raman spectra for the 1.7 x 10^{13} cm^{-2} (100) and (211) Si-implanted GaAs etch sequences, respectively. Figure 5.3 shows the Raman linewidth depth profiles derived from these spectra. The smooth curves shown in Figure 5.3 are Gaussian fits to the data. The depth profiles are very similar in shape, but the results indicate that the implanted near-surface damage layer exhibits more structural damage in the (211) case than in the (100) case.

A similar Raman study was carried out on (100) and (211) samples implanted with a higher fluence, 4 x 10^{13} cm^{-2}. Figures 5.4 and 5.5 show the spectra for the (100) and (211) etch

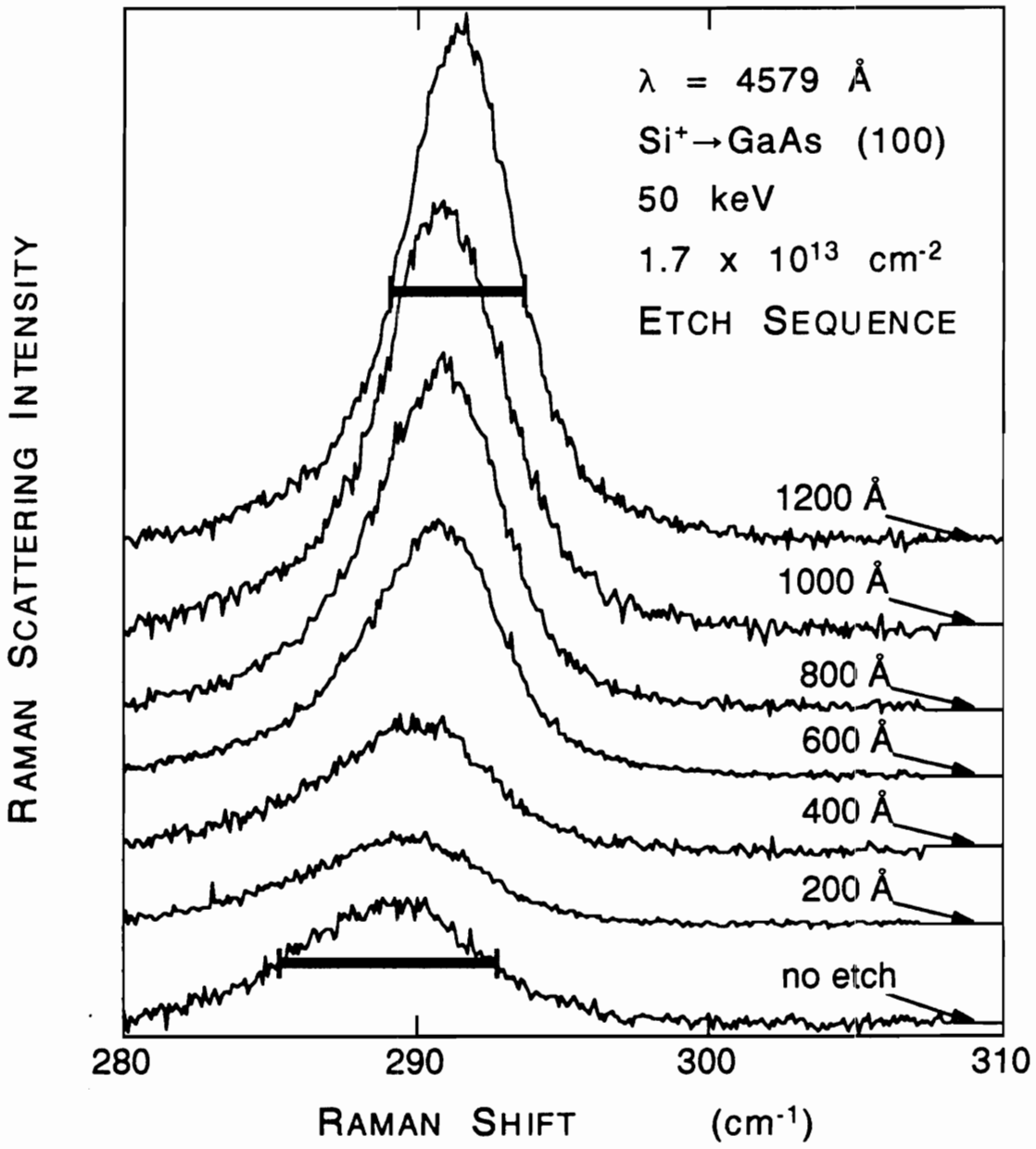

Fig. 5.1: Raman spectra of the LO peak for various etch depths of the (100) , 1.7 x 10^{13} cm^{-2} Si-implanted GaAs samples. The etch sequence goes from bottom to top as the etch depth increases. The a-GaAs contribution has been subtracted, and the spectra are normalized to (the LO peak of) c-GaAs.

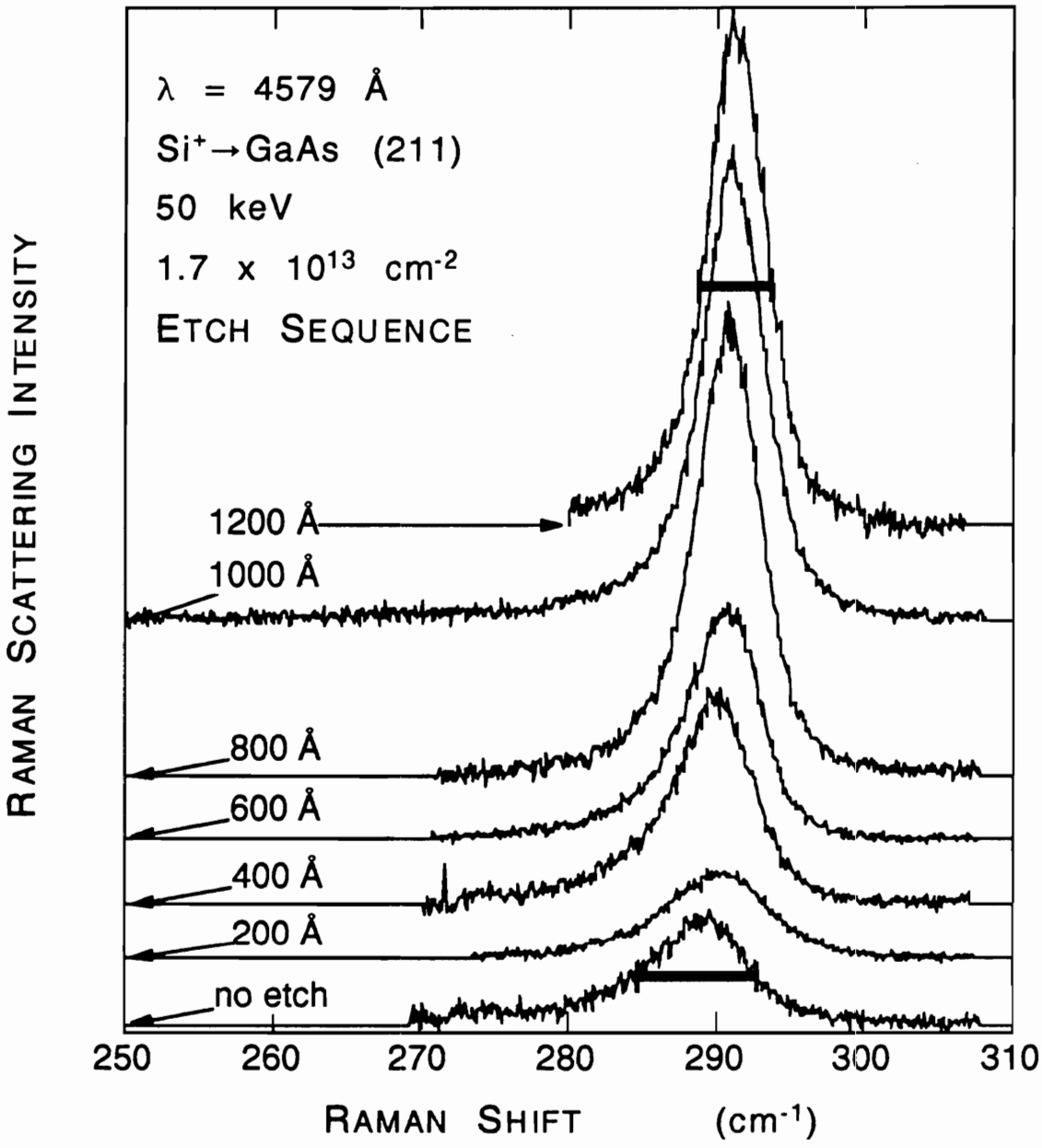

Fig. 5.2: Raman spectra of the LO peak for various etch depths of the (211) , 1.7 x 10^{13} cm^{-2} Si-implanted GaAs samples. The etch sequence goes from bottom to top as the etch depth increases. The a-GaAs contribution has been subtracted, and the spectra are normalized to (the LO peak of) c-GaAs. The TO peak has also been subtracted.

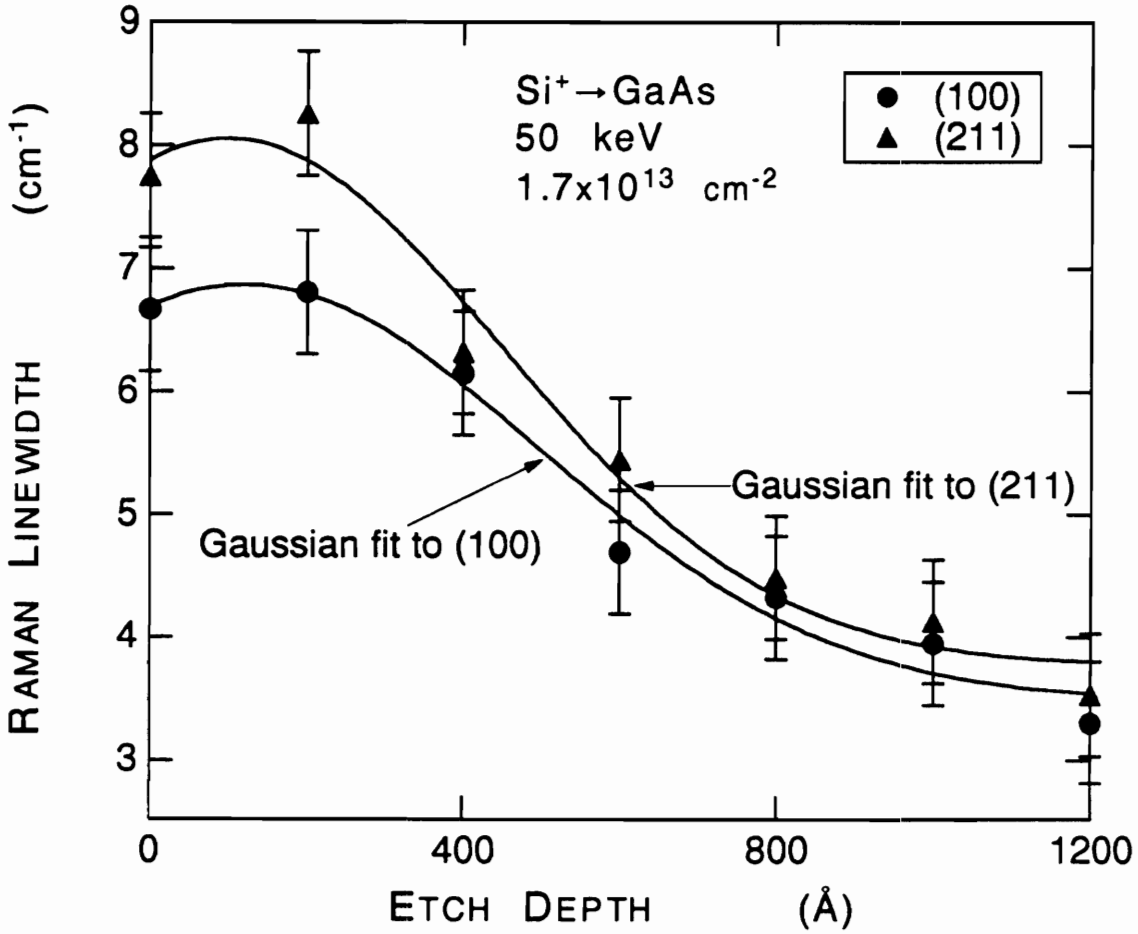

Fig. 5.3: Full Width at Half Maximum vs. etch depth taken from Figures 5.1 and 5.2 (fluence = 1.7 x 10^{13} cm^{-2}). Circles and triangles represent (100) and (211) data points respectively. The smooth curves are Gaussian fits to the data points.

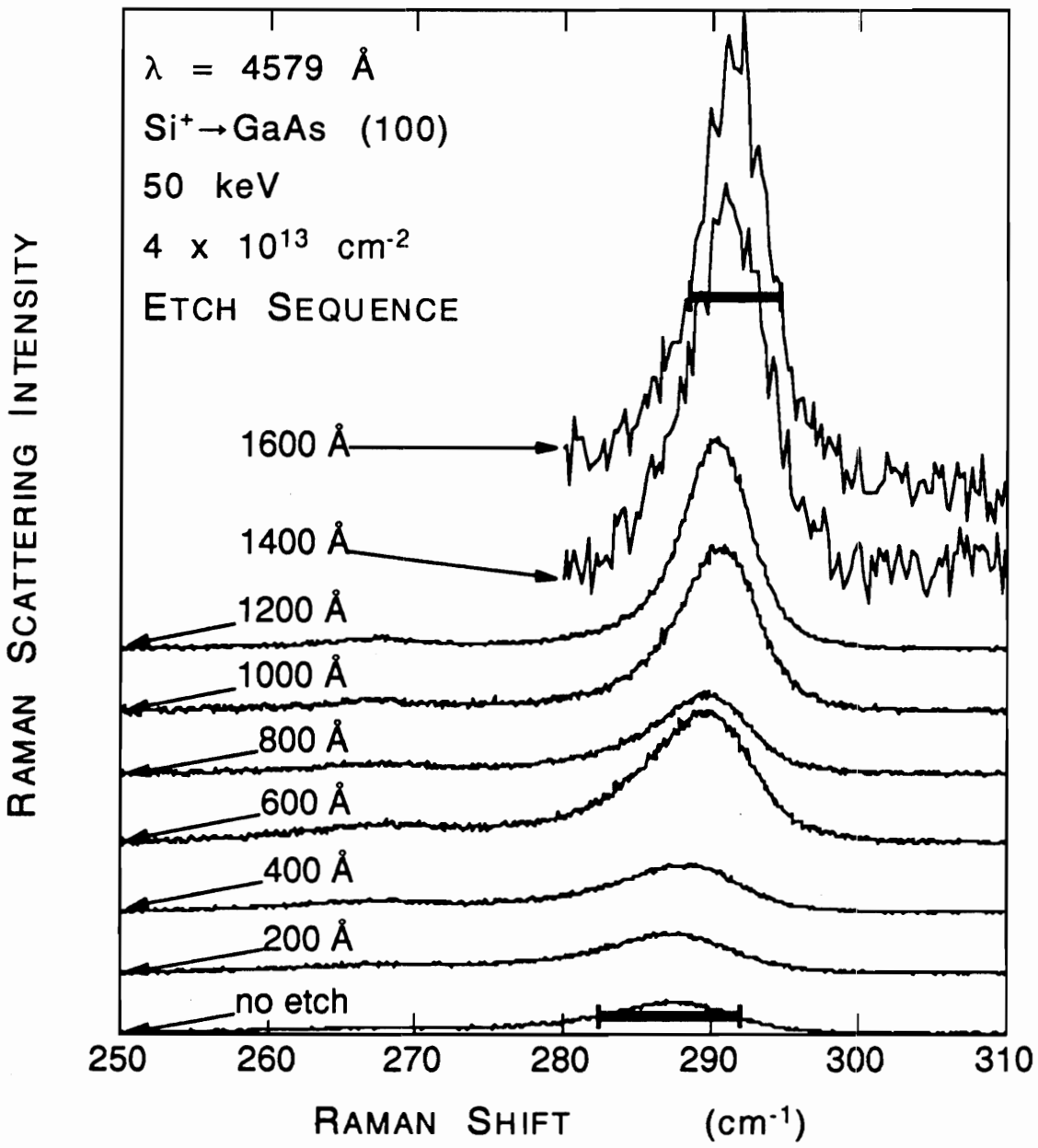

Fig. 5.4: Raman spectra of the LO peak for various etch depths of the (100), 4 x 10^{13} cm^{-2} Si-implanted GaAs samples. The etch sequence goes from bottom to top as the etch depth increases. The a-GaAs contribution has been subtracted, and the spectra are normalized to c-GaAs.

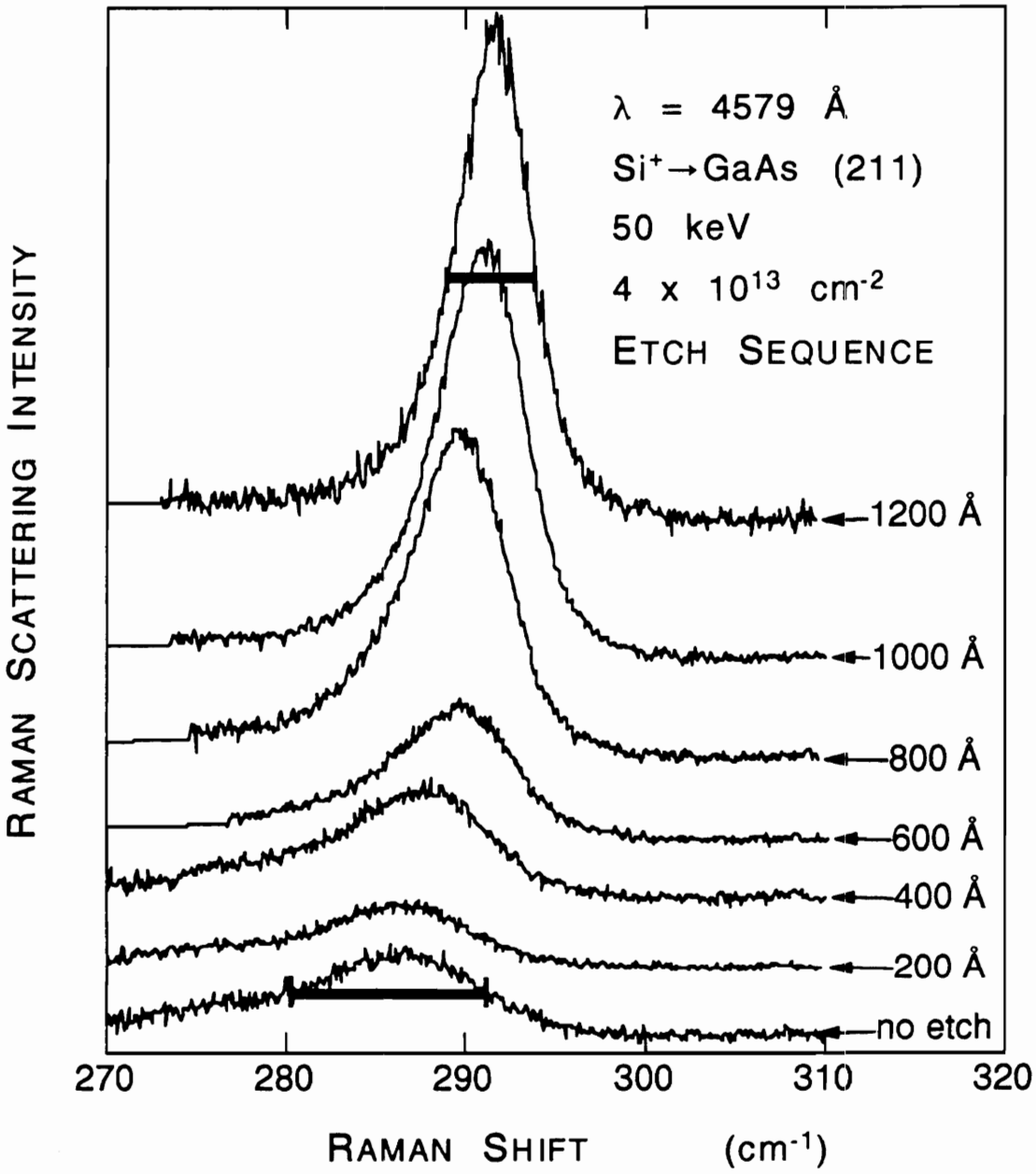

Fig. 5.5: Raman spectra of the LO peak for various etch depths of the (211), 4 x 10^{13} cm^{-2} Si-implanted GaAs samples. The etch sequence goes from bottom to top as the etch depth increases. The a-GaAs contribution has been subtracted, and the spectra are normalized to c-GaAs. The TO peaks have also been subtracted.

sequences respectively. Figure 5.6 shows the Raman linewidth depth profiles obtained from Figures 5.4 and 5.5. The smooth curves in Figure 5.6 are Gaussian fits to the data. The difference between the near-surface damage of the (100) and (211) implants appears to have decreased compared to that observed for the lower-fluence implant. This may be an indication that some saturation in the amount of damage is beginning to appear, and that the (211) samples are closer to saturation than the (100) samples. (Saturation in damage has been observed as the implant fluence increases [Gibbons].) The Gaussian profiles also indicate that the difference in the total damage layer depth between the (100) and (211) implants seems to have increased, with the higher fluence (100) implant showing a deeper damage (Gaussian) tail.

Figure 5.7 shows the Raman spectra for the annealed samples (30 sec, 850°C, rapid thermal anneal). From these spectra, the depletion widths and the carrier concentrations can be estimated as in chapter four. The result is that the (211) implant has a larger depletion width than the (100) implant: 210 ± 25 Å versus 150 ± 20 Å. This corresponds to a lower carrier concentration for the (211) implant: $4.5 \pm 0.7 \times 10^{17}$ cm^{-3} vs. $6.8 \pm 0.7 \times 10^{17}$ cm^{-3}. (The carrier concentration was determined from the depletion width vs carrier concentration graph, Figure 1.8 [Shen et al.].) While this difference is small, it is consistent with the (211) sample having more damage. After annealing, there appear to be more residual defects for the (211) implant.

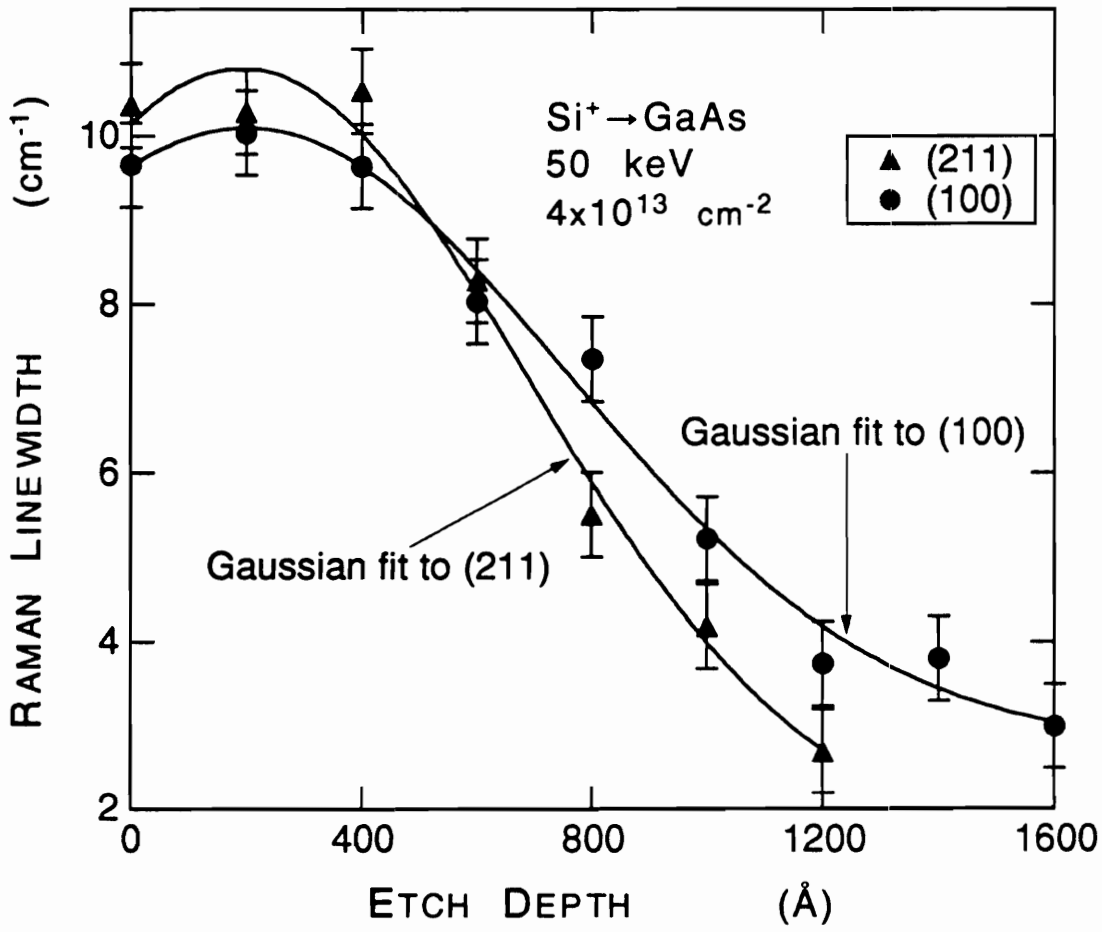

Fig. 5.6: Full Width at Half Maximum vs. etch depth taken from Figures 5.4 and 5.5 (fluence = 4 x 10^{13} cm^{-2}). Circles and triangles represent (100) and (211) data points respectively. The smooth curves are Gaussian fits to the data points.

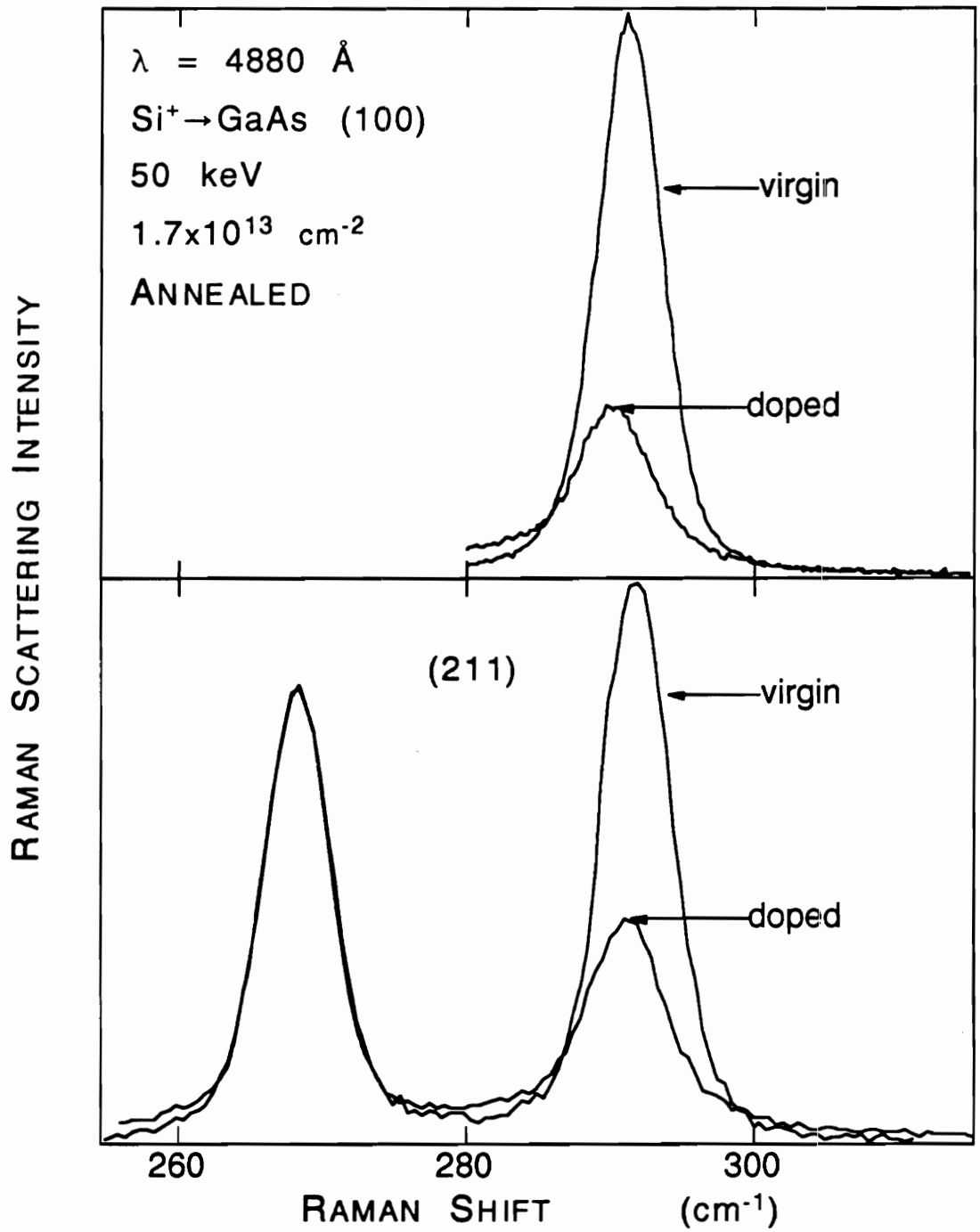

Fig. 5.7: Raman spectra comparing implanted and annealed samples (1.7×10^{13} cm^{-2}, 850 °C RTA) with virgin samples. Upper panel: (100) spectra. Lower panel: (211) spectra. The (211) spectra are normalized via the TO peak while the (100) spectra are normalized to the LO peak of c-GaAs.

Since these defects can act as compensators, the carrier concentration would be lower. There tends to be more As loss at the surface for a sample that is greatly damaged, and it would be more likely for the Si interstitials to move into As sites, thus compensating the Si at Ga sites. There also exists the possibility of Si being backscattered during implantation. Greater damage implies more collisions and therefore a greater possibility of backscattering. It follows that there would be less silicon present in the (211) face, and a lower carrier concentration is obtained upon annealing.

5.4 Ultraviolet Reflectivity Results

5.4.1 Roughness Effects on Reflectivity

One drawback of the etchant described in chapter two is that it introduces roughness in the surface of the etched material. (The arithmetic average roughness is defined as the sum of the absolute values of the differences between the position of the mean height and the positions of sampled points (e.g. peaks and valleys) on the surface divided by the number of sampled points.) The degree of roughness is apparently dependent on many factors that are very hard to control (e.g. post-etch drying time and rinse time, which are only a few seconds long). Hence samples that are etched using the same method will still have variations in roughness from sample to sample. Even the front (implanted side) and back (virgin) surfaces of a sample will have different roughnesses. Sample roughness was measured with a WYKO Topo-3D optical profilometer. Since each measurement

was done over a very small region (mm^2), several measurements at different positions were taken and averaged. Table 5.2 shows the arithmetic average roughness for samples etched up to 1200 Å. The etched samples are rougher than the unetched ones by an amount of the order of 100 Å. The effect is modest for (100) surfaces, but is more pronounced for (211) surfaces.

Roughness decreases the reflectivity of a surface [Zanzucchi and Frenchu, Jezierski and Pawlikowski, Dobrilla], and the decrease gets bigger as the wavelength of the incident light gets shorter [Schiffer]. This is consistent with the observation in this study that the reduction in the reflectivity of an etched c-GaAs sample (compared to that of unetched c-GaAs) increases as the incident photon energy increases.

Another factor that influences the measured reflectivity is the ratio of the roughness height to the optical penetration depth. Between 1.6 and 2.7 eV, the optical penetration depth increases as the photon energy decreases. Below 2.2 eV, the optical penetration depth is more than 500 Å and roughness effects are not so important in this spectral region. Above 2.8 eV, the optical penetration depth is between 50 and 100 Å, so that roughness effects are clearly important here.

Figure 5.8 displays the reduction in reflectivity due to roughness vs. the incident photon energy. This graph was obtained by dividing the reflectivity for etched c-GaAs (the unimplanted surface of the 400 Å etched 4 x 10^{13} cm^{-2} Si-implanted GaAs) by that of unetched c-GaAs . The curve can be modeled

Table 5.2: Arithmetic average roughness (R_a) in angstroms for the etched (211) and (100) Si-implanted GaAs samples.

Etch Depth, Å	0	200	400	600	800	1000	1200
R_a, (211)	310	430	440	490	320	320	810
R_a, (100)	360	370	400	420	380	410	390

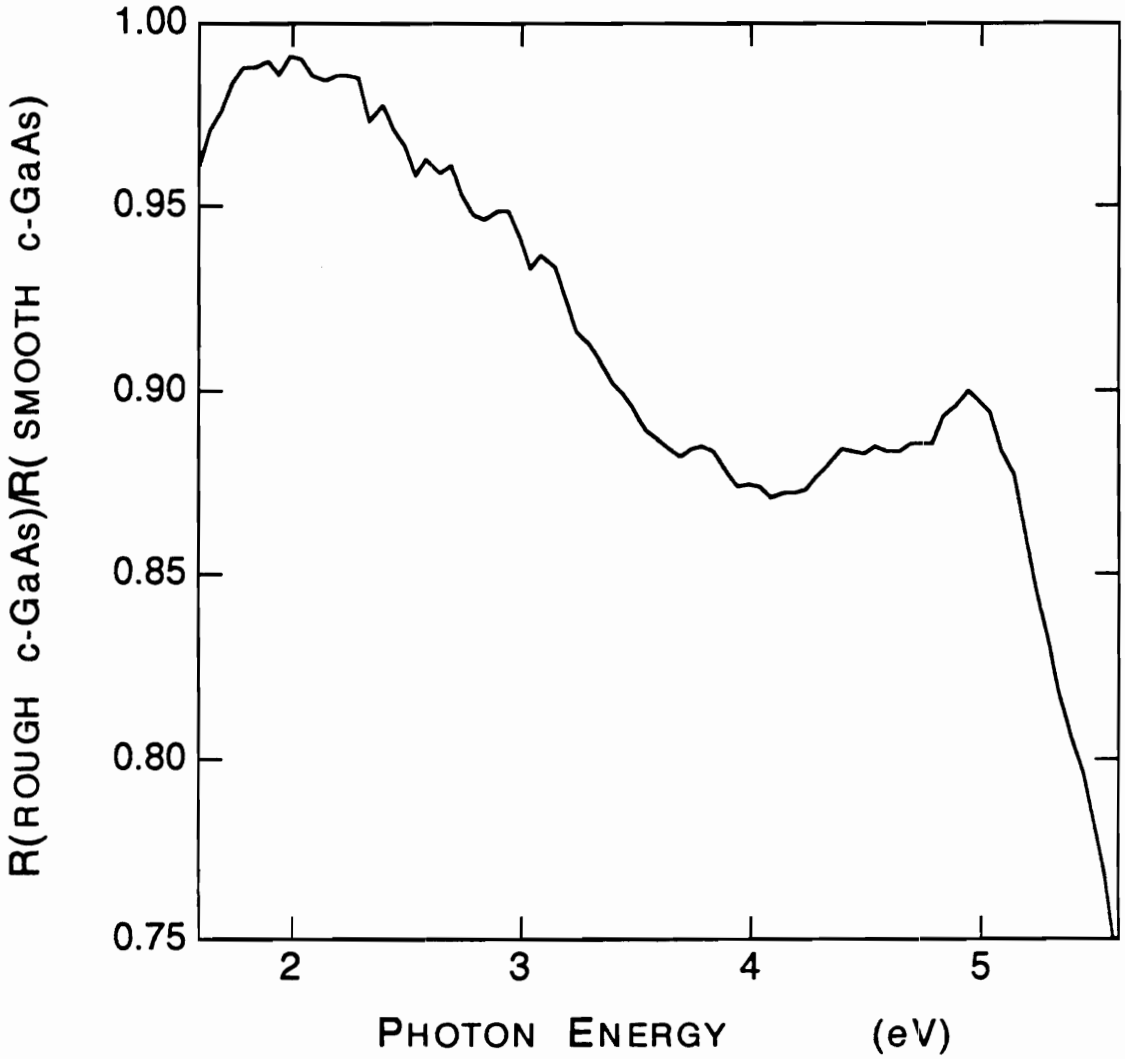

Fig. 5.8: Ratio of the reflectivity of a rough surface of c-GaAs to that of a smooth surface of c-GaAs. This curve displays the reduction in reflectivity, due to roughness, as a function of photon energy.

as a four-piece, piecewise linear function. The second and fourth pieces (2.2 to 4.0 eV and 5.0 to 5.6 eV) have a large slope, while the first and third pieces are practically flat. The large slopes are downward, consistent with the fact that near normal incidence, rough surfaces have a greater reduction in reflectivity for higher photon energies.

An oscillator analysis (similar to the one in chapter three) was carried out on the corrected reflectivities to determine the extent of ion implantation damage. The correction applied to the spectra is based on the observation that for all samples, whether implanted or crystalline, the reflectivity at 3.75 eV can never be lower than 41%. (See Feng and Zallen; note that as fluence (and therefore damage) increases, the value at 3.75 eV increases.) Spectra that had a lower value at 3.75 eV were corrected by dividing it by a four-piece piecewise linear roughness reduction curve which would bring the value of the reflectivity at 3.75 eV to 41%. The reduction curves were obtained by dividing the spectra of rough GaAs by that of smooth GaAs; various reduction curves were generated, each with a different value at 3.75 eV. Appropriate reduction curves were generated by interpolation in order to match the ratio $R(3.75\ eV)_{implanted}/0.41$. However, the oscillator analysis is quite sensitive to this correction and physically unrealistic parameters were obtained. Also, a sharpening of the oscillator linewidths associated with the E_2 electronic transitions occurs for the uncorrected spectra of the implanted samples.

Because of these problems, an alternate method was used to determine the extent of the implantation-related damage. This method was based on three observations: the slope of the c-GaAs reflectivity spectrum in the region between 4 and 5 eV is steep, while that of a-GaAs is close to zero, and the roughness correction factor in this region is also nearly constant. By taking the ratio of the reflectivity at 4.55 eV to that at 4.75 eV, the ratio of correction factors becomes negligible (i.e. it is about 1). Also, this ratio increases as damage increases, eventually approaching the value for a-GaAs. An advantage of this two-wavelength-technique is that only two data points are needed; to do an oscillator analysis, a whole spectrum (81 points) is used.

5.4.2 Two-Wavelength-Technique Results

Figures 5.9 and 5.10 show the reflectivity etch sequence for the (100) and (211) faces, respectively, of 4 x 10^{13} cm^{-2} Si-implanted GaAs. The spectra shown are uncorrected for roughness effects. It can be seen that the slope of the curve between 4 and 5 eV becomes steeper as more material is etched away. Also, though the doublet structure is evident at 1000 Å for the (211) face, a hint of it does not appear for the (100) face until a depth of 1400 Å. This is consistent with the Raman findings of a deeper damage layer for the (100) face. Figure 5.11 shows the damage depth profiles obtained with the two-wavelength-technique. These are also fitted with Gaussians. The (211)

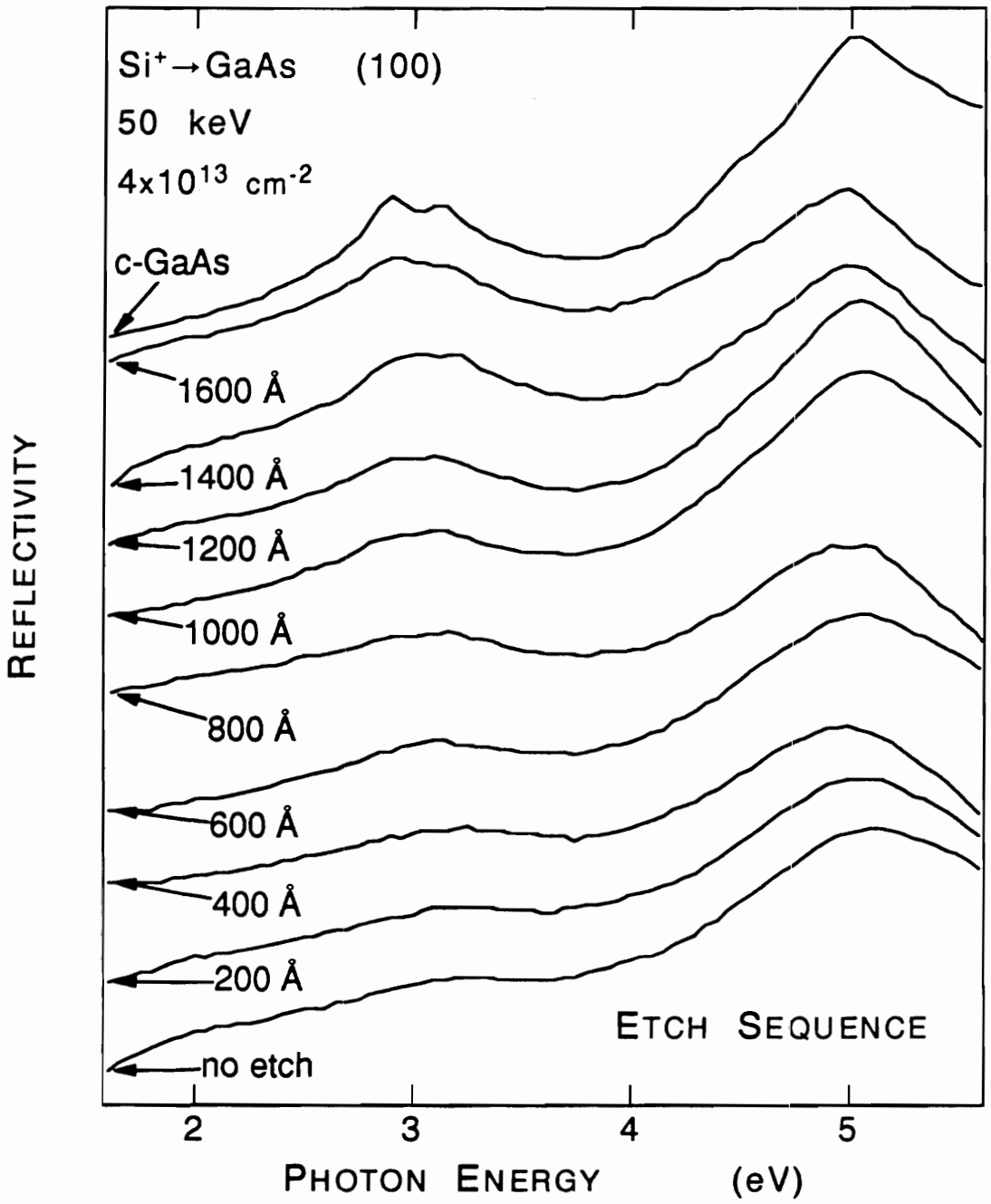

Fig. 5.9: Reflectivity spectra for various etch depths of the (100), 4 x 10^{13} cm^{-2} Si-implanted GaAs samples. The etch sequence goes from bottom to top as the etch depth increases. The spectrum for c-GaAs is shown at the top for comparison.

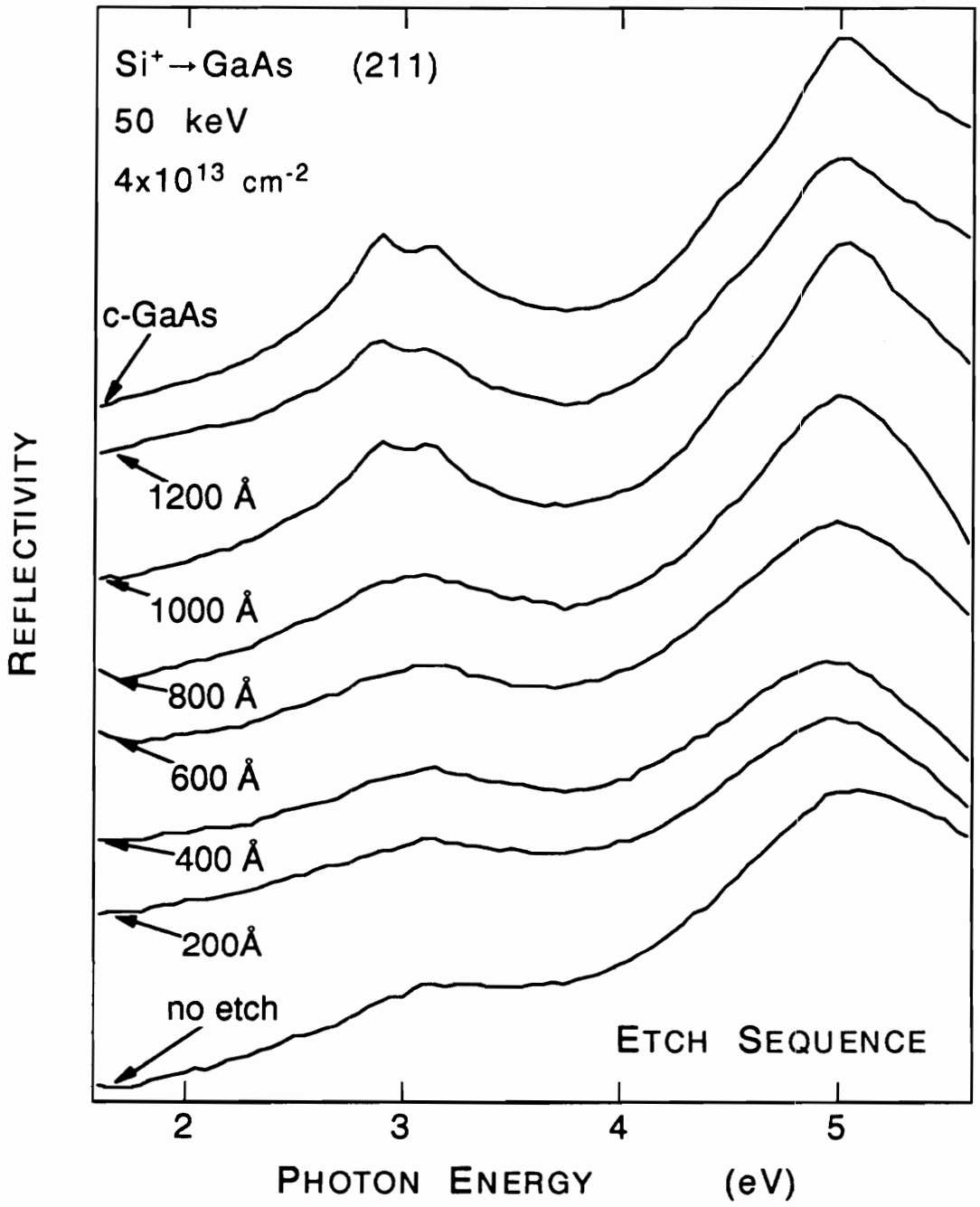

Fig. 5.10: Reflectivity spectra for various etch depths of the (211), 4 x 10^{13} cm^{-2} Si-implanted GaAs samples. The etch sequence goes from bottom to top as the etch depth increases. The spectrum for c-GaAs is shown at the top for comparison.

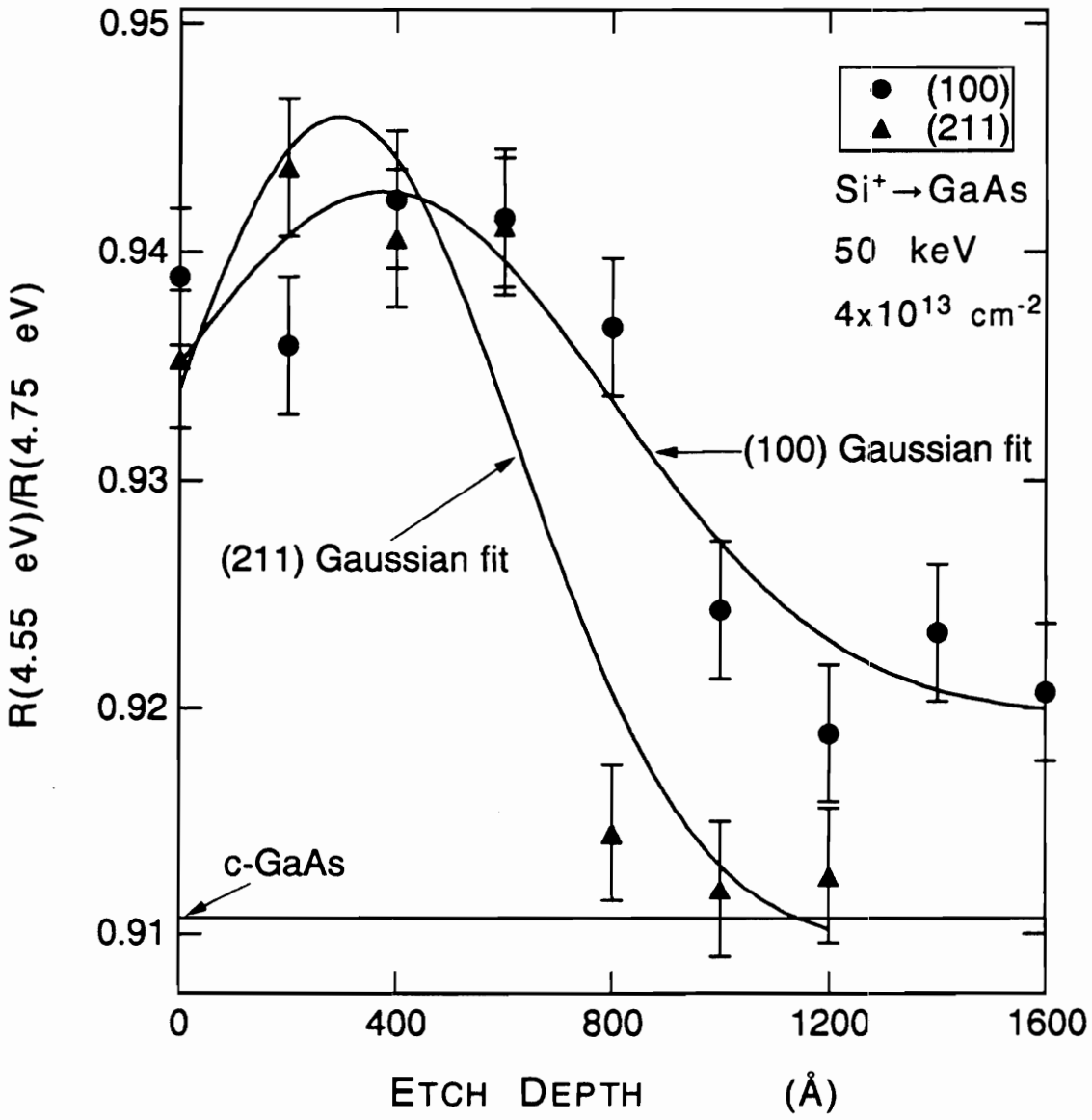

Fig. 5.11: Ratio of the reflectivity at 4.55 eV to that at 4.75 eV vs. etch depth. Circles and triangles represent (100) and (211) data points respectively. The curves are Gaussian fits to the data taken from Figures 5.9 and 5.10.

implant shows more damage near the surface and a smaller total damage layer depth than the (100) implant.

Although this two-wavelength-technique provides crude damage depth profiles, these profiles roughly agree with the Raman-based ones. Hence, despite the presence of variable roughness, ultraviolet reflectivity measurements in combination with chemical etch can still yield qualitative depth profiles of the implantation-induced damage layer.

5.5 Comparison of the Optically Derived Depth Profiles for (211) and (100) implants

The major difference between the (211) and (100) damage depth profiles is that the profile for the (211) face is in better agreement with the Si ion distribution profile predicted by the Lindhard-Scharff-Schiott (LSS) theory [Lindhard et al.]. For 50 keV Si ions implanted in GaAs, a Gaussian distribution with a projected range of 424 Å and a (projected) standard deviation of 254 Å is expected [Gibbons et al.]. That means that 98% of all the ions should be found within 1186 Å. Therefore no damage should be expected beyond 1200 Å, (it is highly unlikely that 2% of the atoms would cause detectable damage) and this is true only for the (211) face. It may be that the (100) face still allows for some slight channeling effects even when the ion beam is tilted 7° with respect to the (100) direction, thus allowing the damage to go beyond 1200 Å, as observed for the higher fluence implant. This is also consistent with less damage

at the surface for the (100) face; less damage means that there were less collisions, so that the ions still had more energy to travel deeper into the sample. It would seem that the local geometry of the (211) face, when tilted at the same angle as the (100) face during implantation, appears to be more random and therefore more closely conforms with the LSS predictions than the (100) face, since the LSS predictions are based on a target with a random arrangement of atoms. Although these LSS predictions are for dopant distributions with depth, the damage distribution with depth should be similar, with the peak of the damage profile at a shallower position since the implanted ion will, on the average, produce less damage near the end of its track. The peaks of the damage distribution Gaussians in all figures occur at depths less than 424 Å, the theoretical projected range, and the (211) peaks always occur at shallower depths than the (100) peaks.

These results indicate that the (211) implant does not have an advantage for device applications. With less damage for (100), there should be less defects after annealing and therefore a higher mobility and carrier concentration. Also, the existence of a plateau region in (100) but not in (211) would imply a flatter carrier concentration distribution for (100) upon annealing. An improvement in controlling the damage depth distribution for the (100) face would be expected if slightly greater tilt angles are used during implantation.

CHAPTER SIX
RESONANT RAMAN SCATTERING BY 2 LO(Γ) PHONONS AT THE E_1 GAP IN CRYSTALLINE AND MICROCRYSTALLINE GaAs

6.1 Introduction

The frequency of the 2LO(Γ) Raman scattering peak displays an oscillatory nature as the incident laser energy is varied across the $E_0+\Delta_0$ gap in GaAs. This behavior is attributed to the creation of LO phonons with different wavevectors, and the wavevector for which the scattering cross section is a maximum changes with the incident laser energy [Olego and Cardona]. The Raman cross section for an iterated electron-one-phonon scattering process due to the Fröhlich interaction at a three dimensional critical point is similar to that at a two dimensional critical point. This similarity can be seen by comparing the expressions for the Raman cross section obtained by Trommer and Cardona, Zeyher, and Martin and Falicov with the expressions given by Renucci et al. Both cross sections involve denominators with a phonon wavevector dependence. Hence one should be able to observe a similar oscillatory behavior for 2LO(Γ) phonons at the two dimensional E_1 gap.

An analysis similar to the one used for the $E_0+\Delta_0$ gap [Olego and Cardona] can be performed on the shifts observed at the E_1 gap and can yield information about the effective masses of the electrons and holes that participate in the scattering. Differences

in the magnitudes of the shifts for crystalline and microcrystalline samples can reflect differences in their band structures. A comparison between the peak shifts of the crystal and microcrystalline surfaces indicate that one could possibly use the 2LO shifts for characterizing shallow (the optical penetration depth at 2.9 eV is 90 Å [Aspnes and Studna]), weakly damaged surface layers in GaAs. Such a technique could complement other resonant two-phonon Raman scattering methods for studying weakly damaged material [Wagner, Wagner and Hoffman] and it will be investigated in this chapter.

6.2 Experiments

The sample used in this study is the Si-implanted (100) GaAs sample annealed at 525 °C described in chapter four. Ultraviolet reflectivity and Raman (LO peak) measurements on the unimplanted face revealed the spectral characteristics of crystalline GaAs. Identical measurements on the implanted and annealed side revealed that a thin 100 Å surface layer is a mixture of microcrystalline and amorphous GaAs; the fraction of the volume probed which was microcrystalline was 92% and the average microcrystal diameter was 400 Å as determined through an oscillator analysis of the reflectivity spectrum in chapter four.

Spectra of both sides were taken with the same focusing conditions. They were measured at room temperature in the standard backscattering geometry. The incident light was polarized

in the $(01\bar{1})$ direction and both polarizations of the scattered light were collected.

Each spectrum was an average of 30 scans (each point was integrated for 3 seconds, points were taken 0.25 cm^{-1} (2.87 to 2.93 ev) and 0.5 cm^{-1} apart) to remove any effects of a slow loss of laser power because of photodecomposition of the dye. Total scanning time for each spectrum was about 1 hr. and 45 minutes. Wavenumber calibration was done by scanning over the laser line (with neutral density filters in place) before and after each spectrum was taken.

6.3 Results and Discussion

Figure 6.1 compares typical spectra (taken at 2.94 eV) for both surfaces of the sample. Although the focusing conditions were kept the same by simply flipping the sample around in its holder, the photodecomposition of the dye gradually changed the incident power. The crystalline surface was measured with an average (over time) power of about 70 mW; the power used for the microcrystalline surface was about 90 mW. Figure 6.1 includes the correction for this (i.e. the spectra are normalized to the same laser power). The reduction in intensity for the microcrystalline surface is large; resonant 2LO(Γ) Raman scattering intensity is known to be very sensitive to surface damage [Wagner and Hoffman].

Figure 6.2 shows the frequency shifts of the 2LO(Γ) peaks from twice the LO(Γ) frequency ($2 \times \Omega_{LO}$ = 583.3 cm^{-1} at room

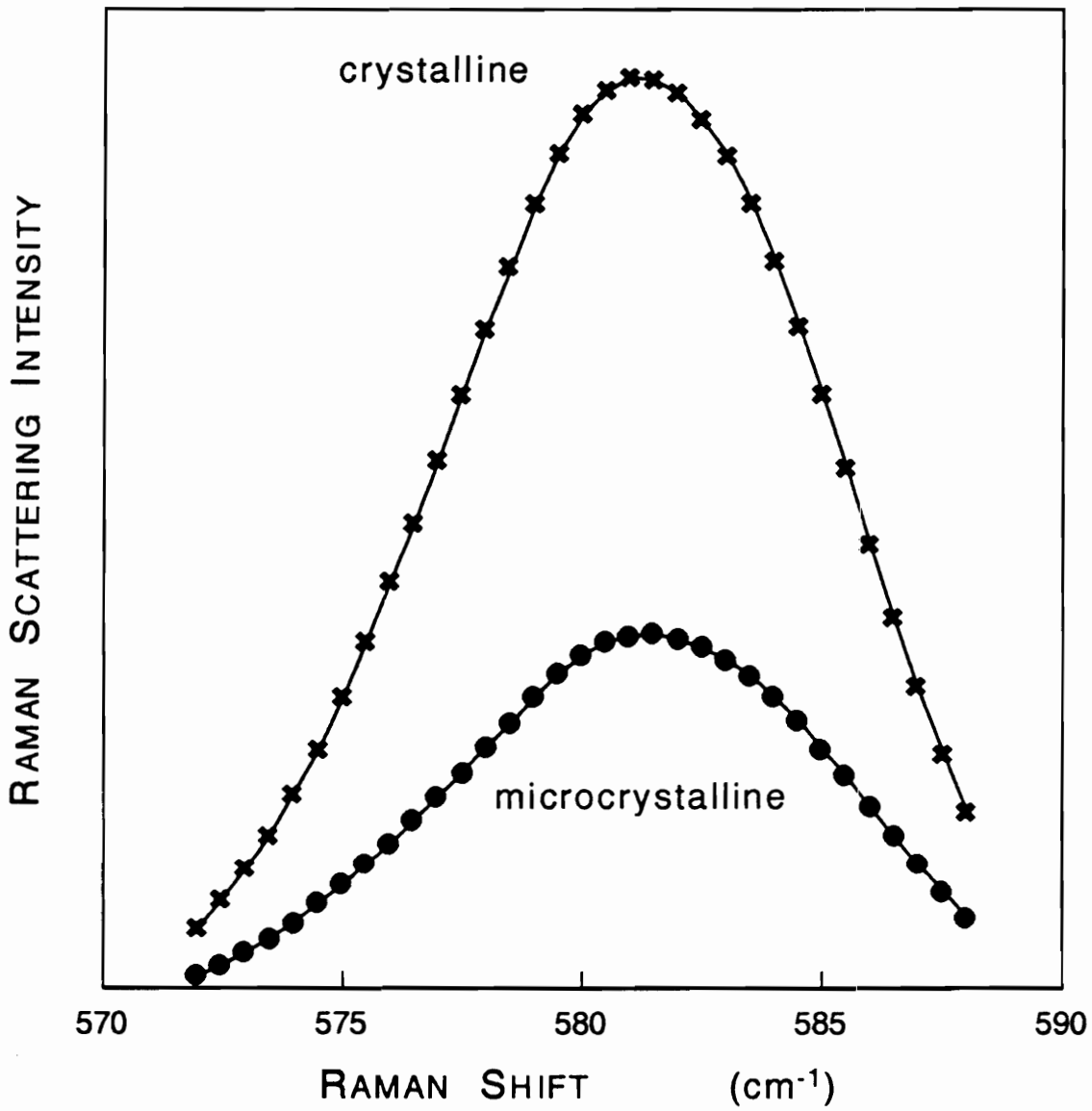

Fig. 6.1: Raman Spectra of microcrystalline (circles) and crystalline (crosses) GaAs. The spectra were taken with an incident photon energy of 2.94 eV.

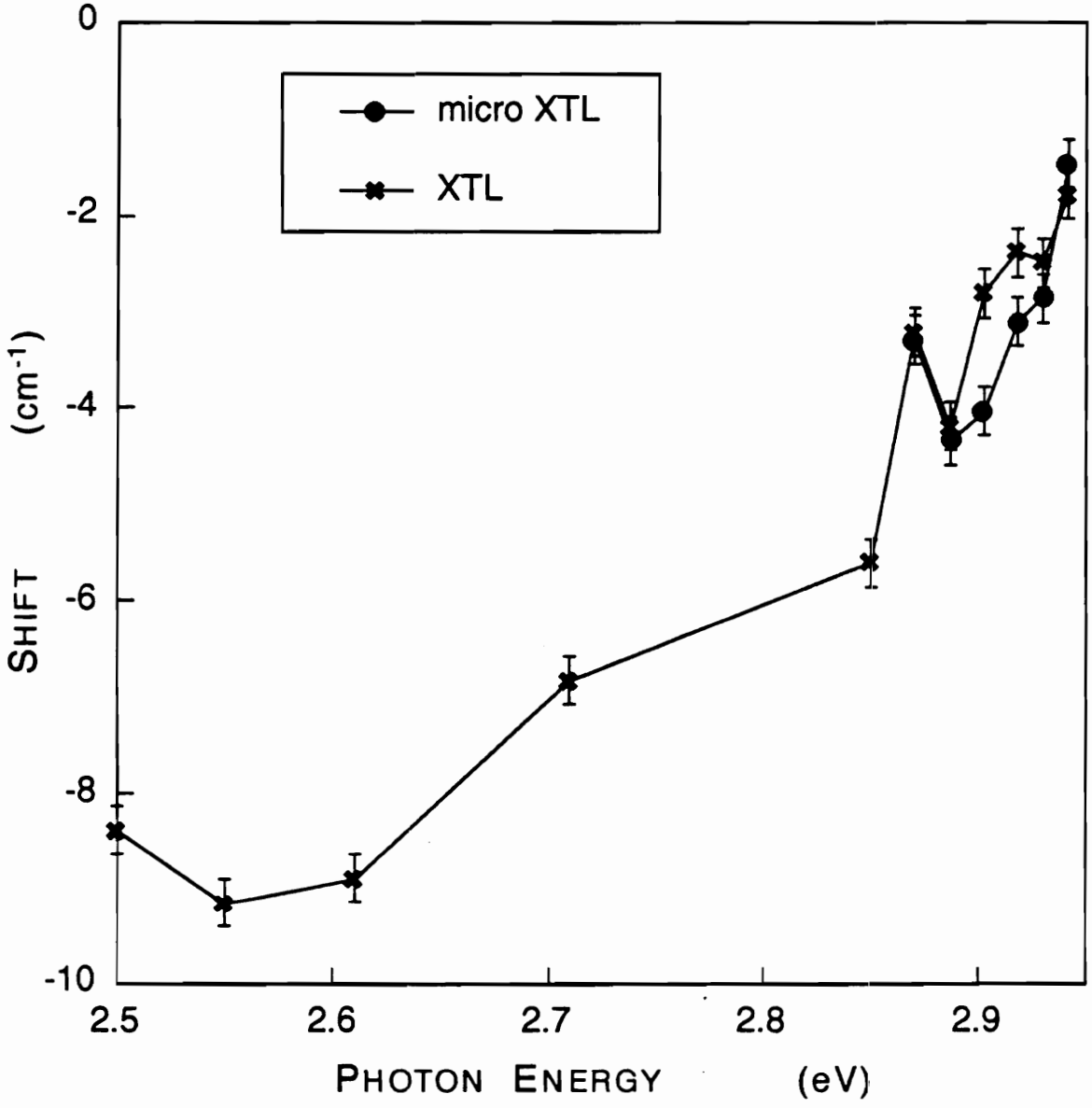

Fig. 6.2: Shifts of the 2LO(Γ) peak from twice the frequency of the LO(Γ) peak in GaAs as a function of the incident photon energy. The lines are shown as a guide to the eye. The microcrystalline shifts are shown with circles, and the crystalline ones are shown with crosses.

temperature [Chandrasekhar and Ramdas]) as a function of the incident photon energy for both the crystalline and microcrystalline surfaces. The shifts were determined by doing a Levenberg-Marquardt curve fit [Press et al.] of the data (ranging from 570 to 590 cm^{-1} near resonance and ranging from 520 to 595 cm^{-1} away from resonance) to the sum of a Lorentzian and a negative slope linear background (2.85 to 2.94 eV) or to the sum of three Lorentzians and a line (2.50 to 2.71 eV). This method was chosen to compensate for the low spectral resolution which was necessary for the enhancement of the signal to noise ratio. The different choices for the functions to which the data were fit are based on the fact that the 2LO peak is much more strongly resonant than the 2TO peak. A comparison between the second order Raman spectra for the energy ranges near resonance and away from resonance is shown in Figure 6.3.

The downward shift in Figure 6.2 increases with decreasing incident energy from 2.94 to 2.89 eV but decreases from 2.89 to 2.87 eV. On the average, the microcrystalline sample has greater shifts, and the linear region has a steeper slope. Beyond this point, there is no data for the microcrystalline sample since the signal to noise ratio for the 2.85 eV spectrum was extremely low and the spectra for energies between 2.50 and 2.71 eV would be mostly due to the underlying crystalline GaAs substrate because of the deeper optical penetration depths. For the crystalline sample, an increase in the size of the shift is observed from 2.87 eV to 2.61 eV, the energy at which the 2LO peak

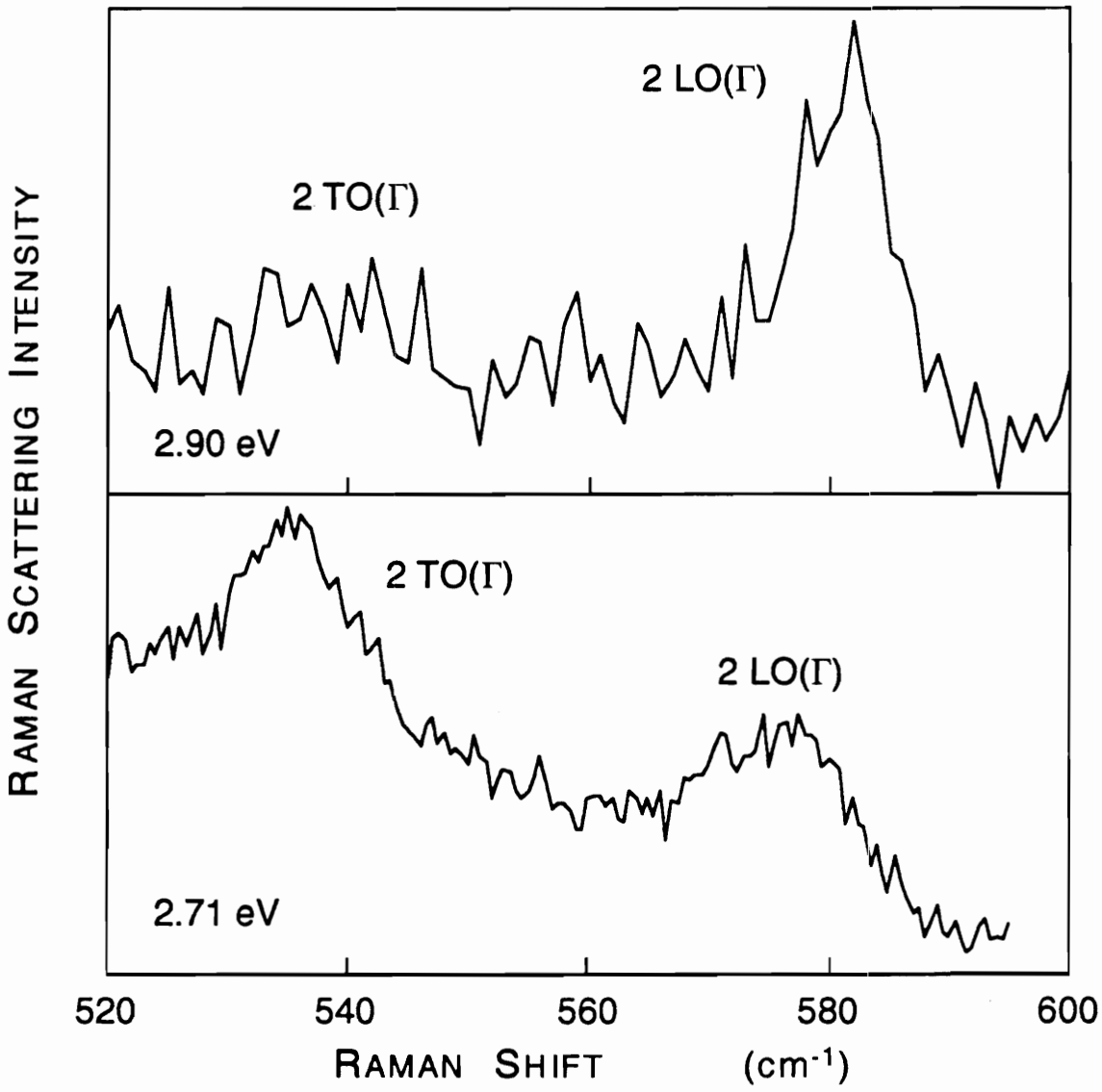

Fig. 6.3: Typical second order Raman spectra including the 2LO(Γ) and 2TO(Γ) peaks. The top spectrum is characteristic of spectra collected with an incident photon energy between 2.85 and 2.94 eV. The incident photon energy used was 2.90 eV. The bottom spectrum was collected with an incident photon energy of 2.71 eV and is representative of spectra in the photon energy range between 2.50 and 2.71 eV.

position is at a minimum. From 2.50 to 2.61 eV, the shift is constant indicating that resonance effects are negligible; at this point, the second order Raman scattering cross section mimics the one-phonon density of states.

These frequency shifts occur when the phonon wavevector which maximizes the scattering cross section changes as a result of varying the incident photon energy, $\hbar\omega_L$. This wavevector is related to the phonon frequency, Ω_{LO}, through the phonon dispersion relation [Olego and Cardona]:

$$\Omega_{LO}(q) = \Omega_{LO}(0) - \frac{\hbar q^2}{2m_{LO}} \qquad (6.1)$$

Here, m_{LO} is an "effective mass" determined by fitting equation 6.1 with the experimental phonon dispersion curves for GaAs [Waugh and Dolling]. The average of m_{LO} over the Λ and Δ directions is $530m_e$.

The magnitude of the wavevector q, which maximizes scattering in the region where the first double resonance is allowed ($\hbar\omega_L > E_1 + \hbar\Omega_{LO}$), has the following form [Martin and Falicov]:

$$q = \left(\frac{2M}{\hbar^2}\right)^{1/2} \left[(\hbar\omega_L - E_1)^{1/2} + (\hbar\omega_L - E_1 - \hbar\Omega_{LO})^{1/2} \right] \qquad (6.2)$$

Here M is the sum of the effective masses of the electron and hole. By substituting the value of q from equation 6.2 into equation 6.1 the peak positions for spectra taken above $E_1 + \hbar\Omega_{LO}$ can be determined.

When $\hbar\omega_L < E_1 + \hbar\Omega_{LO}$, both intermediate and outgoing channels are off resonance; the q dependent factors in the scattering efficiency must be examined closely:

$$\left| \frac{q}{E_1 + \hbar\Omega_{LO} + \frac{\hbar^2 \left(\vec{k} + \vec{q} \right)^2}{2m} - \hbar\omega_L} \right|^2 \qquad (6.3)$$

The Raman tensor is proportional to q (representing the phonon density of states) and also to the second derivative of the electric susceptibility with respect to the photon energy; this derivative has three resonating denominators (see equation 1.6 and Figure 1.5) for an iterated electron-one-phonon scattering process, and the q dependent factor in the denominator is the one which involves the intermediate resonance channel [Trommer and Cardona, Renucci et al.] These factors are what make up equation 6.3. Here, $\vec{k} + \vec{q}$ is the total momentum of the electron-hole pair, and k is equal to the magnitude of the incident photon wavevector.

In this experiment, k is negligible compared to q. In order to observe the frequency shifts, q has to be at least an order of magnitude larger than k in equation 6.1. In first order Raman scattering, q ~ k; since the phonon dispersion curve of GaAs is relatively flat at this q, $\Omega_{LO} = \Omega_{LO}(0)$ and no shift is observed. Since shifts are observed, one can neglect k in solving for the value of q which gives equation 6.3 a maximum:

$$q = \left(\frac{2m}{\hbar^2}\right)^{1/2} \left[E_1 + \hbar\Omega_{LO} - \hbar\omega_L \right]^{1/2} \qquad (6.4)$$

Here, m is some mass parameter. For photon energies above E_1, m = M, the total mass of the free electron-hole pair. Below E_1, there is the possibility of forming bound electron-hole pairs so m could be equal to μ , the reduced mass of the electron-hole pair. This could explain the decrease in the shift at 2.87 eV, since the shift is proportional to q^2 which is in turn proportional to the mass parameter.

By putting equation 6.4 into equation 6.1, the peak positions can be expressed in terms of the mass parameter for the spectra taken with incident photon energies below $E_1 + \hbar\Omega_{LO}$. M can be determined by fitting the experimental peak positions in the region above 2.89 eV to the resulting equation, which is linear. The values for the effective masses of the electron and the hole can be computed from M by using $(m_e^* - m_h^*)/M = 1/3$ [Trommer and Cardona]. However, since there is only one point (at 2.87 eV) from which μ can be determined, curve fitting can not be used to find it. Instead, a range of μ values is determined to reflect the error bars in the peak position. A computed value for μ (taken from m_e^* and m_h^*) can then be compared against this range.

In all of the calculations, a correction to the shift was made to account for the effects of the line shapes on the peak positions. Since the lineshapes for 2LO(Γ) Raman scattering resonant with the E_1 critical point are similar to those for

scattering in resonance with the fundamental gap, (change E_g to E_1 in the expressions given by Zeyher) one can apply the same type of correction used by Olego and Cardona. They made an additional energy dependent shift by a linear interpolation between the natural linewidth of the LO phonon at the critical point energy ($E_0 + \Delta_0$) and zero at 4 x $\hbar\Omega_{LO} + E_0 + \Delta_0$. In this study, a natural linewidth of 2.5 cm^{-1} is used.

The values obtained for the masses from such an analysis are listed in Table 6.1. The effective masses for microcrystalline GaAs are about twice as heavy as those for the crystal. The results for crystalline GaAs agree well with the values taken from Aspnes, 1976. Even the calculated reduced mass of the electron-hole pair falls within experimental error, indicating that bound electron-hole pairs are formed below the E_1 gap.

The value for the mass taken from Aspnes, 1976, is the value at the L-point, and the value for the mass in the Λ direction is about ten times less [Trommer and Cardona]; since the data in this study agree with Aspnes' value one can conclude that the scattering occurred near the L point.

Figure 6.4 shows a graph for the shifts calculated from equations 6.1, 6.2 and 6.4 using the fitted values for the masses, compared with the actual experimental shifts. Both graphs are in good agreement with theory for the region below the double resonance. For the microcrystalline sample, however, better agreement was obtained by considering a shift in E_1 from 2.89 eV to 2.90 eV. In the region where double resonances are

Table 6.1: Effective masses in crystalline and microcrystalline GaAs in units of the electron mass.

	microcrystal	crystal	crystal, other experiments
M	1.45	0.74	0.825[a]
μ (experiment)	0.23 ± 0.12	0.23 ± 0.15	---
μ (calculated)	0.32[a]	0.164[a]	0.183[a]
m_e^*	0.967[a]	0.493[a]	0.55[b]
m_h^*	0.483[a]	0.247[a]	0.275[a]

[a] Values based on $(m_e^* - m_h^*)/M = 1/3$ [Trommer and Cardona].
[b] Aspnes, 1976.

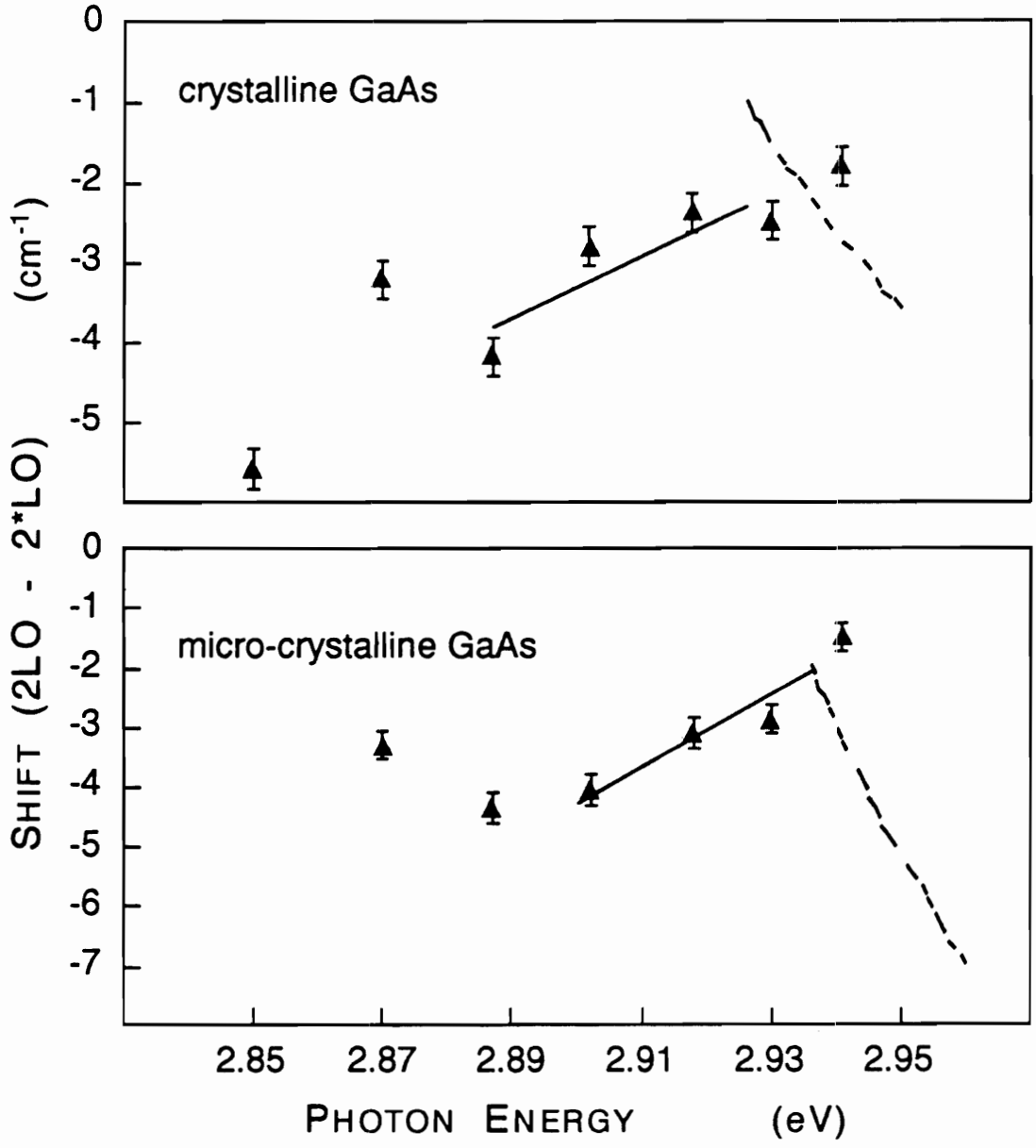

Fig. 6.4: Shifts of the 2LO(Γ) peak from twice the frequency of the LO(Γ) peak in GaAs as a function of the incident photon energy. The curves (solid line: region below double resonance; dotted line: region above) are generated from the appropriate equations in the text using the masses from Table 6.1. Upper panel: crystalline GaAs; lower panel: microcrystalline GaAs.

allowed, it appears that there are not enough points to make a fair comparison. However, it is likely that no double resonances were observed, since these curves are very different from the experimental results.

In conclusion, the shifting of the 2LO(Γ) peak as the incident photon energy is varied across the E_1 critical point in GaAs has been observed. This behavior is also present for the microcrystalline sample, but the slope of the linear region in this case is greater, indicating heavier masses for the electrons and holes in the band structure of microcrystalline GaAs. Such an effect could be used to characterize very weakly damaged samples of GaAs.

CHAPTER SEVEN
SUMMARY

Raman scattering and ultraviolet reflectivity studies are spectroscopic tools that have been used to characterize the structural and electronic changes in GaAs after ion implantation and subsequent annealing. Their applicability to studying the changes arising from such processing steps depends on the nature of the change as well as the optical penetration depth of the incident light used to investigate the change.

The analysis of the spectra of processed GaAs is dependent on the models chosen to represent the structural damage and the changes in the electronic structure. In this dissertation, the damaged structure has been modelled as an amorphous matrix with microcrystalline islands distributed over the matrix. It is characterized according to the average microcrystal diameter and the amorphous volume fraction. The electronic changes have been modelled in terms of an increase in the number of carriers and the presence of plasmons.

With such models, it was seen that ultraviolet reflectivity is mainly a probe of structural disorder, and that it is useful for studying shallow (<100Å) damage layers. On the other hand, the behavior of the Raman LO peak can be monitored to study structural as well as electronic changes provided the carrier concentration is greater than 10^{16} cm^{-3}. For non-resonant techniques, a broad range of probe depths is available. In this

work a range of 260 Å to 1500 Å was used. Raman spectra for the 2LO peak measured with an incident photon energy near the E_1 interband transition provides information about very weakly damaged shallow layers.

To study ultraviolet reflectivity spectra taken over a limited range of photon energies, an oscillator analysis was performed instead of using the Kramers-Kronig equations. The behavior of the parameters of the seven oscillators was monitored as a function of damage by studying the damage depth profile of Be-implanted GaAs, and it was found that the parameters which varied the most (and systematically) with damage are the linewidths of the interband reflectivity peaks and the dielectric constant at infinity. These parameters can be used for depth profiling.

A comparison of the profiles generated in previous Raman experiments [Holtz et al.,1988] with the profiles from the reflectivity spectra provided insight into the connection between the LO peak shifts and the changes in (all) the oscillator parameters. The parameters provide information about the value of the real part of the dielectric function in an energy region between and including the electronic and vibrational excitations. The Lyddane-Sachs-Teller relation then establishes the link between this value and the static dielectric constant through the LO peak shifts. This link also suggests that the static dielectric constant is independent of the microcrystal size.

The annealing studies made use of the Raman LO peak linewidth and intensity as well as an oscillator analysis of

reflectivity spectra. The Si-implanted samples were characterized at various annealing temperatures; this revealed that recrystallization occurs at a lower temperature than electrical activation. At 525°C, both Raman and reflectivity spectra look like the spectra for virgin c-GaAs. However, the Raman LO peak drops in intensity at 775°C, indicating the coupling of the LO phonons with plasmons. The carrier concentration was estimated from this intensity reduction, showing that the carrier concentration at 525°C could not have been more than half of the value at 775°C. Van der Pauw measurements confirmed these results.

A comparison between the Raman LO linewidth damage depth profiles of the as-implanted and 400°C annealed samples showed that recrystallization occurs not only at the interface between the damaged layer and the underlying c-GaAs layer but also at the boundaries of the microcrystals within the damaged layer. The 400°C profile showed an advance of the interface from 1600 to 1000 Å away from the surface, but it also showed that the microcrystal size in the 1000 Å thick surface layer had increased. Polarization experiments were performed to find out the Raman selection rules in the microcrystals, and these rules were identical to that of the starting material. This means that the microcrystals retain the orientation the crystal had before implantation, and therefore it was not necessary for the damaged-undamaged layer interface to advance to the surface to correct for any misorientation in the microcrystals.

In the comparison between Si-implanted (100) and (211)

GaAs, depth profiling was achieved through chemical etch. Unfortunately, the etchant induced surface roughness on the samples affected the measured Raman LO intensity as well as the ultraviolet reflectivity spectra. Hence, Raman studies concentrated on the linewidth of the LO peak since it is intensity-independent. However, a new method of analyzing the reflectivity spectra had to be developed; an oscillator analysis of spectra that were corrected for roughness effects produced physically unrealistic parameters. It was observed that the reduction in reflectivity caused by roughness was constant in the region between 4.5 and 5.0 eV. By taking the ratio of reflectivities between 4.55 and 4.75 eV, the reduction factor drops out. This ratio changes as damage is introduced, and it was used to provide a damage depth profile for both faces. While this two-wavelength-technique is crude, it produced results in fair agreement with those obtained from the Raman linewidth analysis.

While the differences between the profiles for the 1.7 x 10^{13} cm^{-2} implanted samples were small, they were qualitatively the same as the differences noticed for the higher fluence of 4 x 10^{13} cm^{-2}. It was observed, from Raman as well as reflectivity spectra, that the (211) surface had a more LSS-like damage depth profile than the (100) surface did. The damage was also greater and concentrated closer to the surface for the (211) implant. Some slight channeling effects were observed only for the (100) implant. These differences favor the (100) implant as a better candidate for device manufacturing.

Finally, the shifts (from twice the LO peak frequency) in the frequency of the Raman 2LO peak at resonance with the E_1 interband transition energy were studied. The shift varies with the incident photon energy since the wavevector which maximizes the Raman scattering cross section changes as the incident photon energy is scanned across the E_1 gap. Both crystalline and microcrystalline (diameter > 400 Å) GaAs displayed such shifts. An analysis of the slope of the graph of the shifts vs. the incident photon energy yields information about the total mass of the electron-hole pair involved. A comparison between the slopes of the microcrystalline and crystalline material suggests an increase in this total mass for GaAs microcrystals.

References

D. E. Aspnes, Phys. Rev. B. 14, 5331 (1976).

D. E. Aspnes, Thin Solid Films 89, 249 (1982).

D. E. Aspnes, private communication (1988).

D. E. Aspnes, S. M. Kelso, C. G. Olson and D. W. Lynch, Phys. Rev. Lett. 48, 1863 (1982).

D. E. Aspnes and A. A. Studna, Phys. Rev. B 27, 985 (1983).

I. Banerjee, P. W. Chye and P. E. Gregory, IEEE Elect. Dev. Lett. 9, 10 (1988).

J. L. Birman, Phys. Rev. 131, 1489 (1963).

J. L. Birman, Theory of Crystal Space Groups and Infra-Red and Raman Lattice Processes, in Encyclopedia of Physics, L. Genzel, ed. (Springer-Verlag,1974).

J. S. Blakemore, J. Appl. Phys. 53, R123 (1982).

A. Borghesi, A. Piaggi, A. Stella, G. Guizzetti, D. Bisero and G. Queirolo, J. Appl. Phys. 67, 7045 (1990).

N. Bottka, D. K. Gaskill, R. S. Sillmon, R. Henry and R. Glosser, J. Electronic Mater. 17, 161 (1988).

A. G. Bruggeman, Ann. Phys. (Leipzig) 24, 636 (1935).

G. Burns, Introduction to Group Theory with Applications (Academic Press, New York, 1977).

M. Cardona in Light Scattering in Solids, Vol. II, M. Cardona and G. Guntherodt, Eds. (Springer-Verlag, Berlin, 1982).

M. Cardona in Proceedings of the Society of Photo-Optical Instrumentation Engineers, Vol. 822, Raman and Luminescence Spectroscopy in Technology (SPIE, Bellingham, 1987), p.2.

H. R. Chandrasekhar and A. K. Ramdas, Phys. Rev. B 21, 1511 (1980).

M. L. Cohen and J. R. Chelikowsky, Electronic Structure and Optical Properties of Semiconductors, (Springer-Verlag, 1988).

P. Dobrilla, Mater. Letters 7, 78 (1988).

B. Dorner and D. Strauch, private communication, 1987.

W. M. Duncan, TI Technical Journal, p. 18, Sept.-Oct. 1988.

W. M. Duncan and G. Westphal in VLSI Electronics: Microstructure Science, N. G. Einspruch and W. R. Wisseman, eds. (Academic Press, New York, 1985).

H. Ehrenreich and M. H. Cohen, Phys. Rev. 115, 786 (1959)

J. Epp, J. G. Dillard, A. Siochi, R. Zallen, E. D. Cole, S. Sen, A. Vaseashta, and L. C. Burton, in Processing and Characterization of Materials Using Ion Beams, MRS Vol. 128, edited by L. E. Rehn, J. E. Greene, and F. A. Smidt (Materials Research Society, Pittsburgh, 1989), p.677.

M. Erman and J. B. Theeten, Surf. Interface Anal. 4, 98 (1982).

M. Erman, J. B. Theeten, P. Chambon, S. M. Kelso and D. E. Aspnes, J. Appl. Phys. 56, 2664 (1984).

G. F. Feng, Ph.D. Dissertation, Virginia Tech (1989).

G. F. Feng and R. Zallen, Phys. Rev. B 40, 1064 (1989).

J. F. Gibbons, Proc. IEEE 60, 1062 (1972).

J. F. Gibbons, W. S. Johnson and S. W. Mylroie, Projected Range Statistics: Semiconductors and Related Materials (Dowden-Hutchinson-Ross, Stroudsburg, 1975).

M. L. Gray, J. M. Parsey, Jr., R. E. Ahrens, S. J. Pearton, K. T. Short, L. Sargent and J. S. Blakemore, J. Appl. Phys. 66, 4176 (1989)

D. L. Greenaway and G. Harbeke, Optical Properties and Band Structure of Semiconductors (Pergamon Press, Oxford, 1968).

M. H. Grimsditch, D. Olego and M. Cardona, Phys. Rev. B 20, 1758 (1979).

W. Hayes and R. Loudon, Scattering of Light by Crystals (Wiley, New York, 1978).

M. Holtz, Ph.D. Dissertation, Virginia Tech, (1987).

M. Holtz, R. Zallen, O. Brafman and S. Matteson, Phys. Rev. B 37, 4609 (1988).

M. Holtz, R. Zallen, A. E. Geissberger and R. A. Sadler, J. Appl. Phys. 59, 1946 (1986).

K. Huang, Proc. Roy. Soc. (London) A208, 352 (1951).

IMSL, Math/PC-Library (User's Manual), 1984.

J. D. Jackson, Classical Electrodynamics, 2nd ed. (Wiley, New York, 1975).

K. Jezierski, J. Phys. C 19, 2103 (1986).

K. Jezierski and J. M. Pawlikowski, Acta Phys. Pol. A67, 447 (1985).

Y. Kato, T. Shimada, Y. Shiraki and K. F. Komatsubara, J. Appl. Phys. 45, 1044 (1974).

M. Lax, Symmetry Principles in Solid State and Molecular Physics, (Wiley, New York, 1974).

J. Lindhard, M. Scharff and H. Schiott, Mat. Fys. Medd. Dan. Vid. Sclsk. 33, 1 (1963).

R. Loudon, Phys. Rev. 137, A1784, (1965).

R. M. Martin and L. M. Falicov in Light Scattering in Solids I, M. Cardona, ed. (Springer-Verlag, Berlin, 1975).

J. W. Mayer and S. S. Lau, Electronic Materials Science: For Integrated Circuits in Si and GaAs (Macmillan, New York, 1990).

W. McLevige, Ph.D. Dissertation, University of Illinois, (1978).

D. L. Mills, Vijnana Parishad Anusandhan Patrika 14, 115 (1971).

T. Nakamura and T. Katoda, J. Appl. Phys. 53, 5870 (1982).

T. Nakamura and T. Katoda, Jpn. J. Appl. Phys. 23, L552 (1984).

T. Nakamura and T. Katoda, J. Appl. Phys. 57, 1084 (1985).

D. Olego and M. Cardona, Solid State Commun. 39, 1071 (1981).

S. J. Pearton, Solid State Phenomena 1 / 2, 247 (1988).

A. Pinczuk, A. A. Ballman, R. E. Nahory, M. A. Pollack and J. M. Worlock, J. Vac. Sci. Technol. 16, 1168 (1979).

F. H. Pollak and R. Tsu in Proceedings of the Society of Photo-Optical Instrumentation Engineers, Vol 452, Spectroscopic Characterization Techniques for Semiconductor Technology (SPIE, Bellingham, 1984), p.26.

W. H. Press, B. P. Flannery, S. A. Teukolsky and W. T. Vetterling, Numerical Recipes (Cambridge University Press, 1986).

M. A. Renucci, J. B. Renucci, R. Zeyher and M. Cardona, Phys. Rev. B 10, 4309 (1974).

H. Richter, Z. P. Wang and L. Ley, Solid State Commun. 39, 625 (1981).

H. Ryssel and I. Ruge, Ion Implantation (Wiley, Chichester, 1986).

G. A. Samara, Phys. Rev. B 27, 3494 (1983).

R. Schiffer, Appl. Opt. 26, 704 (1987).

S. Sen, Ph.D. Dissertation, Virginia Tech, (1990).

H. Shen, F. H. Pollak and R. N. Sacks, Proceedings of the Society of Photo-Optical Instrumentation Engineers, vol. 524, Spectroscopic Characterization Techniques for Semiconductor Technology II (SPIE, Bellingham, 1985), p. 145.

S. Shigetomi and T. Matsumori, Jpn. J. Appl. Phys. 22, 1294 (1983).

W. G. Spitzer and D. A. Kleinman, Phys. Rev. 121, 1324 (1961).

J. L. Tandon, J. H. Maddok, I. S. Leybovich, G. Bai and M. A. Nicolet, Appl. Phys. Lett. 54, 448 (1989).

J. B. Theeten and M. Erman, J. Vac. Sci. Technol. 20, 471 (1982).

K. K. Tiong, P. M. Armitharaj, F. H. Pollak and D. E. Aspnes, Appl. Phys. Lett. 44, 122 (1984).

R. Trommer and M. Cardona, Phys. Rev. B 17, 1865 (1978).

H. W. Verleur, J. Opt. Soc. Am. 58, 1356 (1968).

J. Wagner, Appl. Phys. Lett. 52, 1158 (1988).

J. Wagner and Ch. Hoffmann, Appl. Phys. Lett. 50, 682 (1987).

J. Wagner, H. Seelewind and W. Jantz, J. Appl. Phys. 67, 1779 (1990).

J. L. Waugh and G. Dolling, Phys. Rev. 132, 2410 (1963).

D. R. Wight in Gallium Arsenide Materials, Devices, and Circuits, M. J. Howes and D. V. Morgan, eds. (Wiley, New York, 1985).

W. A. Wooster, Tensors and Group Theory for the Physical Properties of Crystals (Clarendon Press, Oxford, 1973).

E. S. Yang, Fundamentals of Semiconductor Devices, (McGraw-Hill, New York, 1978) pp. 9-20.

H. Yoshida and T. Katoda, J. Appl. Phys. 67, 7281 (1990).

R. Zallen, The Physics of Amorphous Solids (Wiley, New York, 1983).

P. J. Zanzucchi and W. R. Frenchu, Appl. Opt. 20, 643 (1981).

R. Zeyher, Phys. Rev. B 9, 4439 (1974).

VITA

Ramon Alfredo Carvalho Siochi was born on May 22, 1963 in Manila, Philippines. He received his B.S. Physics degree, Summa Cum Laude, at the Ateneo de Manila University in the Philippines in March, 1985. He then came to Virginia Tech in September, 1985; there he received an M.S. in Physics in February, 1988, and a Ph.D. in Physics in December, 1990.